

METASTABILITY OF COPPER INDIUM GALLIUM DISELENIDE
POLYCRYSTALLINE THIN FILM SOLAR CELL DEVICES

by

JINWOO LEE

A DISSERTATION

Presented to the Department of Physics
and the Graduate School of the University of Oregon
in partial fulfillment of the requirements
for the degree of
Doctor of Philosophy

September 2008

University of Oregon Graduate School

Confirmation of Approval and Acceptance of Dissertation prepared by:

Jin Woo Lee

Title:

"Metastability of Copper Indium Gallium Diselenide Polycrystalline Thin Film Solar Cell Devices"

This dissertation has been accepted and approved in partial fulfillment of the requirements for the Doctor of Philosophy degree in the Department of Physics by:

Stephen Kevan, Chairperson, Physics
J David Cohen, Member, Physics
Roger Haydock, Member, Physics
David Strom, Member, Physics
Mark Lonergan, Outside Member, Chemistry

and Richard Linton, Vice President for Research and Graduate Studies/Dean of the Graduate School for the University of Oregon.

September 6, 2008

Original approval signatures are on file with the Graduate School and the University of Oregon Libraries.

© 2008 JinWoo Lee

An Abstract of the Dissertation of
JinWoo Lee for the degree of Doctor of Philosophy
in the Department of Physics to be taken September 2008

Title: METASTABILITY OF COPPER INDIUM GALLIUM DISELENIDE
POLYCRYSTALLINE THIN FILM SOLAR CELL DEVICES

Approved: _____
Dr. J. David Cohen

High efficiency thin film solar cells have the potential for being a world energy solution because of their cost-effectiveness. Looking to the future of solar energy, there is the opportunity and challenge for thin film solar cells.

The main theme of this research is to develop a detailed understanding of electronically active defect states and their role in limiting device performance in copper indium gallium diselenide (CIGS) solar cells. Metastability in the CIGS is a good tool to manipulate electronic defect density and thus identify its effect on the device performance. Especially, this approach keeps many device parameters constant, including the chemical composition, grain size, and interface layers. Understanding metastability is likely to lead to the improvement of CIGS solar cells.

We observed systematic changes in CIGS device properties as a result of the metastable changes, such as increases in sub-bandgap defect densities and decreases in

hole carrier mobilities. Metastable changes were characterized using high frequency admittance spectroscopy, drive-level capacitance profiling (DLCP), and current-voltage measurements. We found two distinctive capacitance steps in the high frequency admittance spectra that correspond to (1) the thermal activation of hole carriers into/out of acceptor defect and (2) a temperature-independent dielectric relaxation freeze-out process and an equivalent circuit analysis was employed to deduce the dielectric relaxation time. Finally, hole carrier mobility was deduced once hole carrier density was determined by DLCP method.

We found that metastable defect creation in CIGS films can be made either by light-soaking or with forward bias current injection. The deep acceptor density and the hole carrier density were observed to increase in a 1:1 ratio, which seems to be consistent with the theoretical model of $V_{Cu}-V_{Se}$ defect complex suggested by Lany and Zunger. Metastable defect creation kinetics follows a sub-linear power law in time and intensity.

Numerical simulation using SCAPS-1D strongly supports a compensated donor-acceptor conversion model for the experimentally observed metastable changes in CIGS. This detailed numerical modeling yielded qualitative and quantitative agreement even for a specially fabricated bifacial CIGS solar cell. Finally, the influence of reduced hole carrier mobility and its role in limiting device performance was investigated.

CURRICULUM VITAE

NAME OF AUTHOR: JinWoo Lee

PLACE OF BIRTH: Seoul, Korea

DATE OF BIRTH: April 16, 1973

GRADUATE AND UNDERGRADUATE SCHOOLS ATTENDED:

University of Oregon, Eugene

Yonsei University, Seoul, Korea

DEGREES AWARDED:

Doctor of Philosophy in Physics, 2008, University of Oregon

Master of Arts in Physics, 2000, Yonsei University

Bachelor of Arts in Physics, 1996, Yonsei University

AREAS OF SPECIAL INTEREST:

Semiconductor Device Physics

Thin Film Solar Cell Device Modeling

PROFESSIONAL EXPERIENCE:

Yield Improvement Engineer, Hynix Semiconductor Manufacturing America,
Eugene, 2006-2007

Research and Teaching Assistant, Department of Physics, University of Oregon,
2001-2006

GRANTS, AWARDS AND HONORS:

Junior Scholar Award, University of Oregon, 1995

PUBLICATIONS:

J. Lee, J. T. Heath, J. D. Cohen, and W. N. Shafarman, "Detailed study of metastable effects in the Cu(InGa)Se₂ alloys: test of defect creation models", Mat. Res. Soc. Symp. Proc. 865, F12.4.1, 2005.

A. F. Halverson, P. T. Erslev, J. Lee, J. D. Cohen, and W. N. Shafarman, "Characterization of the Electronic Properties of Wide Bandgap Cu(InGa)(SeS)₂ Alloys", Mat. Res. Soc. Symp. Proc. 865, A.13.7, 2005.

J. Lee, J. D. Cohen, and W. N. Shafarman, "The determination of carrier mobilities in CIGS photovoltaic devices using high-frequency admittance measurements", Thin Solid Films 480-481, 336-340, 2005.

J. Lee, J. T. Heath, W. N. Shafarman, and J. D. Cohen, "Role of bulk defect states in limiting CIGS device properties", in Conference Record of IEEE 4th World Conference on Photovoltaic Energy Conversion, Vol. 1, 360, 2006.

J. Lee, D. B. Needleman, W. N. Shafarman, and J. D. Cohen, "Understanding metastable defect creation in CIGS by detailed device modeling and measurements on bifacial solar cells", Mat. Res. Soc. Symp. Proc. 1012, Y.12.02, 2007.

ACKNOWLEDGMENTS

Isaac Newton once said: Dwarf (ironically, that's me) on the shoulder of the giants (e.g. Dr. Cohen). I am very grateful to have such giants who supported me until the completion of this dissertation. I wish to express sincere appreciation to Professor J. David Cohen for his guidance of this research at the University of Oregon. Without his good advice and freedom of creative research in the Cohen lab, it would have been impossible to reach this far. I would like to thank my family: my parents who trusted my endeavor in science; my sister JiYeon; and especially KyoungA, who helped me achieve the utmost of my ability; lovely daughters Sean, Bella, and Priya.

I am very lucky to have had Dr. Jennifer Heath as my lab colleague. She set a role of scientific achievement and success in the early years of my research. I would like to thank Dr. William N. Sharfarman for providing the high performance CIGS samples. Simply, this research work would not have been possible.

I am also grateful to have had Dr. Shouvik Datta for unlimited access of scientific discussion and job talks. I would like to thank my lab co-workers; Adam Halverson, who helped my time enjoyable in the basement study room; Pete Erslev, who have endured the basement workspace together, Peter Hugger for reading my dissertation despite poor grammar and kinky transitions; David Berney Needleman and Ken Alder, who worked with me and more importantly helped to shape an idea through innumerable friendly discussions.

I would like to thank those who encouraged me outside my workplace. Among

them, pastor Ko from Eugene Presbyterian church, HR manager Koh from Hynix semiconductor, and Mr. Shin, the former president of Eugene Korean Association. Also, I would like to acknowledge my colleagues at Hynix semiconductor who encouraged me to follow my passion in scholastic research environment.

Last but not least, I am proud of what I was able to contribute to the progress in the knowledge of science as much. However, it may have been possible only with the help from all of you above. I would like to thank you all who helped me in the past while I continued Ph.D. course in Physics here in Oregon.

June 2008

JinWoo Lee

To KyoungA, Sean, Bella, and Priya

TABLE OF CONTENTS

Chapter	Page
I. MOTIVATION	1
1.1 Why Renewable Energy Is Important	1
1.2 Why Thin Film Solar Cell Is Important	4
1.3 Organization of the Thesis	6
Notes	8
II. THIN FILM SOLAR CELL BACKGROUND AND SAMPLES STUDIED....	10
2.1 Electrical Properties of Semiconductor	10
2.2 Quantum Mechanical Interpretation of Carrier Transport	11
2.3 Material properties of polycrystalline CIGS thin film solar cell	12
2.4 Samples for This Study	14
Notes	18
III. EXPERIMENTAL METHODS	19
3.1 High Frequency Admittance Spectroscopy	19
3.1.1 Admittance Spectroscopy of CIGS and Dielectric Relaxation	20
3.1.2 Density of States in the Bandgap	29
3.1.3 Numerical Modeling by SCAPS-1D	31
3.2 Drive Level Capacitance Profiling	34
3.2.1 Determination of Majority Carrier Mobility	37
3.2.2 Distinguishing Free Carrier Density from Bulk Defect States	38
3.3 Current-Voltage Curve Analysis	39
3.3.1 Ideal Diode Equation Analysis	40
3.3.2 Red Kink Effect in the Near-Infrared Current-Voltage Curves	46
Notes	48
IV. METASTABILITY IN CIGS	50
4.1 Metastable Defect Creation in CIGS	50
4.1.1 Metastable Defect Creation and Annealing	51
4.1.2 Configurational Coordinate Change for Metastability in CIGS	55
4.1.3 Light-induced Metastability	56

Chapter	Page
4.1.4 Meyer-Neldel Rule Behavior of the Metastability in CIGS	59
4.1.5 Universal 1:1 Ratio in Metastable Defects Creation	61
4.1.6 Lany-Zunger's Theoretical Model	64
4.2 Metastable Defect Creation Kinetics	66
4.2.1 Sub-linear Time and Intensity Dependence of Defect Creation Kinetics in CIGS	66
4.2.2 Rate Equation Analysis	67
4.2.3 Two Electron Capture Model	69
Notes	72
 V. MODELING OF METASTABILITY IN CIGS USING THE COMPENSATED DONOR-ACCEPTOR CONVERSION MODEL	 74
5.1 Metastability in the Wide Bandgap CIGS	74
5.1.1 Correlation between Electronic Defects and Photovoltaic Device Performance	76
5.1.2 Metastable Changes in J - V Curves	77
5.1.3 SCAPS Modeling of Metastability	82
5.1.4 Relationship between J - V Device Parameters.....	84
5.2 Detailed Modeling of Metastability in CIGS Solar Cells	90
5.2.1 Compensated Donor-to-Acceptor Conversion Model	90
5.3 Bifacial CIGS Solar Cells	94
5.3.1 Metastability in the Bifacial CIGS Solar Cells	94
5.3.2 Temperature and Intensity Dependence of I - V Curves.....	97
5.3.3 I - V curve roll-over at low temperatures	101
5.4 Mobility Limitation on the CIGS Device Performance	103
Notes	105
 VI. SUMMARY AND CONCLUSIONS	 108
 REFERENCES	 112

LIST OF FIGURES

Figure		Page
2.1	Cross-sectional SEM image of CIGS thin film solar cells.....	15
3.1	Schematic of the experimental instrumentation.....	21
3.2	Admittance spectra for CIGS 33400 have been measured at 175 K showing two distinctive steps	23
3.3	Equivalent circuit model	25
3.4	High frequency capacitance and conductance data on CIGS sample 33456 at 125 K and two different values of applied bias.	28
3.5	Density of states schematic diagram for a-Si:H and CIGS	30
3.6	Band diagram for CIGS solar cell under front illumination of 100 mW/cm^2 at 300 K.....	32
3.7	Admittance spectra for CIGS 33400 as a function of temperature and bias voltage.....	33
3.8	Comparison of CV and DLCP measured at 1 MHz.....	35
3.9	Typical example of J - V curve characteristics under AM1.5 standard illumination condition, $100\text{mW}/\text{cm}^2$ at 25°C	40
3.10	Light and dark J - V curve characteristics of typical CIGS cell.....	42
3.11	Intensity and temperature dependence of V_{OC} for the bifacial CIGS #33873.22 and the baseline SCAPS model.....	44
3.12	Red kink effect (open symbols) and UV curing method (solid symbols) for the near-infrared light J - V curves	47
4.1	Isochronal annealing of the light-induced changes in the high frequency capacitance and DLCP	52
4.2	Energy barriers for light-induced metastability in CIGS	53
4.3	Energy-configurational coordinate diagram for metastable defect creation and annealing effects in CIGS.....	55

Figure	Page
4.4 Persistent photocapacitance (PPC) for CIGS 33400 under light-soaking at 780 nm.....	56
4.5 Comparison of admittance spectra after light-soaking treatment	57
4.6 Meyer-Neldel rule (MNR) behavior of metastability in CIGS	60
4.7 High frequency admittance spectra and 1 MHz DLCP profiles at 125 K for CIGS #33400 before (pre-LS) and after light-soaking at 250 K for increasing exposure times	61
4.8 Light-induced changes in DLCP and CV density	62
4.9 Universal 1:1 ratio in metastable defect creation regardless of the method used to create the metastable changes	63
4.10 Time and intensity dependence of metastable defect creation after light-soaking at 780 nm at 250 K.....	66
4.11 Saturation of the metastable defect creation assuming a limited defect density of precursor sites.....	68
5.1 Comparison between the expected CIGS device parameters obtained from SCAPS modeling and the actual experimental results from IEC devices in Table 2.1.....	75
5.2 Metastable changes in J - V curves for CIGS #33713	78
5.3 Non-linear square fitting (NLSF) of the experimentally obtained J - V curves to the ideal diode equation after light-soaking treatments.....	79
5.4 Typical analysis of un-ideal J - V curve parameters	80
5.5 Variation of the ideality factors A with the light-soaking treatments	81
5.6 SCAPS simulation with the deep acceptor as the dominant recombination center.....	83
5.7 Effect of light-soaking treatments on device parameters.....	84
5.8 Relationship between FF and hole carrier mobility.....	86
5.9 Metastable FF and J_{SC} changes for CIGS #33713 at 300 K.	88

Figure	Page
5.10 Relationship between I_{SC} and hole carrier mobility	89
5.11 SCAPS modeling of light-induced metastability in CIGS	91
5.12 V_{OC} dependence on the donor defect state	92
5.13 SCAPS modeling demonstrating the reverse bias $I-V$ curve behavior of bifacial CIGS #33873.22 device	95
5.14 Temperature dependence of V_{OC} for bifacial CIGS #33873.22 device at 980nm.....	98
5.15 Energy band diagram showing pinning of electron quasi-Fermi level at CIGS/CdS interface at 300 K.....	99
5.16 Temperature dependence of V_{OC} for CIGS, CISS and CIGSS devices.....	100
5.17 Temperature dependence of white $I-V$ for CISS #24160 (a) before light-soaking (b) after light-soaking for 12 hours at RT	102
5.18 Temperature dependence of $I-V$ curves for CIGSS #24442.....	102
5.19 Effect of hole mobility on CIGS device performance obtained from SCAPS modeling as μ_h varies from 0.05 to 50 cm^2/Vs	104

LIST OF TABLES

Table		Page
2.1	List of electrical characteristics for CIGS, CISSe and CIGSSe samples.....	17
3.1	SCAPS parameters used to fit admittance spectra in Fig. 3.7.	33
5.1	Baseline SCAPS parameters for modeling.	93
5.2	SCAPS parameters for the compensated donor-to-acceptor conversion model	94

CHAPTER I

MOTIVATION

No new [energy] under the sun [in this world]

- Ecclesiastes 1.9

1.1 Why renewable energy is important

Solar energy is the only nearly limitless renewable energy source in the strict sense. Every hour earth receives enough solar energy for one year of worldwide energy consumption - about four orders of magnitude more than the current total annual energy needs for the entire planet [1, 2]. If we can learn to convert this solar energy to a useable form, then there would be no energy shortage in our world any more. However, if solar energy is going to become a practical alternative to fossil fuels, we need to develop efficient ways to convert sunlight into a convenient form of energy.

Planet earth has provided us with a very useful form of energy source for the last centuries: oil, which is predominantly used as a combustible fuel. Although today's

primary sources of consumer energy – oil, coal, and gas – are relatively cheap and abundant, they are not only limited in availability but are also being criticized as a possible source of climate change (e.g. global warming), and are questionably viable for longer term use in the near future [3]. The increasing rate of population growth makes this situation worse. If two billion people in China and India start to want a better standard of living, it simply means that more energy is required. The so-called “Chindia factor” would be a disaster for the rest of the world unless their well-being is guaranteed by a more secure energy source [4]. Although it is impossible to accurately predict when the peak production in oil would occur (in other words, when demand for cheap oil would surpasses its supply) or when global warming would become a direct threat to the ecosystem, if we do not prepare for an alternate future with renewable energy sources, a real catastrophe seems inevitable given the current level of world energy consumption. At the current rate, world energy consumption can not be sustained unless a cooperative transition to alternative renewable energy sources takes place in the very near future.

When one considers the different forms of alternative energy sources, hydroelectricity is the most common form of renewable energy; however, the most cost effective sites have already been exploited. Wind energy cannot provide more than a small fraction of the world energy since its cost-effectiveness is proportional to the cubic power of the average wind speed, so potential windmill sites are limited to the off-shore areas with a high wind speed. Economically and technologically practical biomass energy is in the distant future considering the already consequential disruptions in the food market if used on a large scale. Hydrogen technology requires basic research

breakthroughs in hydrogen generation and fuel cell efficiency to compete with current technologies. Furthermore, hydrogen is not a direct source of energy but just a carrier at most [5]. Solar (or photovoltaic) cells convert sunlight directly into electricity. Only solar energy has a potential to replace the current level of fossil fuel. The U.S. is lucky to be endowed with a vast solar energy potential; converting only a small fraction of solar radiation into electricity in the Nevada desert area would provide enough energy for its entire national energy consumption [6].

Due to the growing need for renewable energy, the solar cell industry has expanded dramatically in recent years. Just mimicking Moore's law in the micro-electronics industry, overall solar cell production has been doubling every two years, increasing by an average of 35 % each year since 2002, making it the world's fastest-growing technology sector [7]. Among the available solar technologies, thin film solar cell technologies mostly fabricated from a-Si:H and CdTe achieved a 62 % production growth in 2007. With the increasing manufacturing volume of solar cells, the industry is learning how to handle large scale production more efficiently and cheaply with a cost reduction over a cumulated learning curve, following rather general economic laws. Economies of scale and continued long term research experience will help to lower the manufacturing costs further [5].

For the large-scale solar cell deployment of electricity at a rate of 6 cents per kWh by 2020, Ken Zweibel, one of the most renowned renewable energy analysts in the field has recently proposed so called a "solar grand plan". In his article, \$420 billion in subsidies from 2011 to 2050 would be required to fund the infrastructure to make solar

economy cost-competitive [8]. This analysis assumes the readily-available average conversion efficiency of 14 percent with cost of system installation at \$1.20 per watt [8]. Current thin film solar modules have 10 percent efficiency and an installed system cost of about \$4 per watt.

Developing renewable energy means more than just a large chunk of investment. It requires public acceptance of a new way of living, a new culture at the same time. In fact, we need to figure out the right renewable solution right now. Imposing CO₂ emissions caps is not working fast enough to motivate people to conserve better or switch to the renewable energy. Simplifying our way of living and focusing on conservation is probably not be a sufficient solution in a world in which energy demands are ever growing faster than supply.

1.2 Why the thin film solar cell is important

The demand for solar cells, although small compared with the overall energy supply (less than 0.1% of total electricity consumption), has been growing rapidly (e.g., 62% in 2007) for the last several years. One reason for the growth in the thin film solar cell industry has been due to the polycrystalline Si shortage for Si solar cells. Since the material used to manufacture Si solar cells needs to be about one hundred times thicker than the typical thin-film technologies to capture the same amount of sunlight, small material usage is one of the most promising cost-effective strategies for thin film solar cell technology. Also, there are well-developed thin film deposition technologies in the

liquid crystal display (LCD) industry on the inexpensive large-area substrates like window glass. Currently, thin film solar cells can be manufactured at half the cost of crystalline Si, but have only roughly half the efficiency, so there is no net gain.

It is ironic that the technologies based on crystalline Si faces a real material shortage and consequent price increases because of scarcity in the polycrystalline Si feedstock. Furthermore, Si solar cells are already approaching a theoretical upper limit for energy conversion efficiency around 25 %, thus leaving little room for cost reduction largely because of silicon's 1.1 eV indirect bandgap. To date, the most efficient PV cell is a concentrated GaAs tandem cell, which boosts the conversion efficiency above 40 % [9]. This approach, however, is very expensive and new technologies such as dye cells, organic photovoltaics, and third-generation concepts have just begun and have a long research and development path ahead. For example, a unique quantum effect was found in silicon nanocrystal quantum dot materials by NREL researchers [10]. Although this quantum dot with the multiple exciton generation (MEG) could have a potential to reach a theoretical maximum efficiency as high as 85% in the thermodynamic limit, more lab-scale research to learn how to make a proper pn junction on the quantum dots for large area applications is an unsolved problem.

High efficiency thin film solar cells such as amorphous silicon (a-Si:H), copper indium-gallium diselenide (CIGS), and CdTe are gaining ground in part due to their cost-effectiveness. Steady progress in energy conversion efficiency has been made both in the laboratory and industry scale for these thin film solar cells [11-13]. An alternative for high efficiency thin film solar cells is to develop moderate-efficiency devices at

extremely reduced costs. Keeping in mind that price reduction in Si technology has been made by continuous improvement in the manufacturing process, thinning wafer thickness and manufacturing capacity expansion, we can expect the thin film solar cell to follow the same track of crystalline Si solar cells. Indeed, CIGS thin film solar cells have already attained a 19.9 % in the laboratories. It may remain to learn how to maintain this performance level under a large scale manufacturing process.

As we look to the future of solar energy, it is clear that there are great opportunities and challenges for the material sciences. Once again, no new renewable energy exists *under* the sun in this world. It only comes *from* the sun.

1.3 Organization of the thesis

This thesis is organized as follows: Chapter 2 introduces the basic concepts of polycrystalline CIGS thin film solar cells. Ch. 3 describes the experimental methods used for electrical characterization of metastability in CIGS and presents mobility measurement method using high frequency admittance spectroscopy and drive level capacitance profiling (DLCP). Also, a novel J - V curve analysis method based on the intensity dependence of V_{OC} will be introduced and the origin of the diode ideality factor for solar cells will be explained by comparing the intensity dependence of the open circuit voltage and the quasi-Fermi level splitting in the middle of CIGS absorber using numerical simulation SCAPS-1D.

Ch. 4 proposes a detailed energy-configurational coordinate diagram for the metastability in CIGS films to relate changes in the device performance, and observes systematic metastable changes in electronic defect states during the metastable treatments, such as the 1:1 ratio relationship between deep defect densities and free carrier density and changes in hole carrier mobilities as well as electrical properties. Ch.4 also discussed the observation of the “Meyer-Neldel rule” (MNR) behavior of the deep acceptor defect activation energy during metastability, sub-linear power law in time and intensity dependence of defect creation kinetics in CIGS. A two electron capture model is proposed to explain the metastable defect creation in CIGS.

Ch5 presents numerical modeling of metastability in CIGS solar cells using the SCAPS-1D simulation program and discussed the roles of electronic defects and hole carrier mobility in limiting CIGS device performance by comparing experimental results and device modeling regarding metastability in CIGS. This detailed numerical modeling was also found to yield a good agreement for the specially designed bifacial solar cells both qualitatively and quantitatively.

Finally, Ch. 6 concludes with a summary of experimental results. This thesis contribution provides a detailed understanding of metastability in thin film CIGS solar cells, the carrier transport mechanism, the electronic defect states, and the related device performance.

Notes

- [1] N. S. Lewis, and D. G. Nocera, *Science*, **103**, 15729 (2006).
- [2] N. S. Lewis, *Science*, **798**, 1137014 (2007).
- [3] G. W. Crabtree and N. S. Lewis, *Physics Today*, **60**, 37 (2007).
- [4] International Energy Agency, *World Energy Outlook 2007*, URL <http://www.worldenergyoutlook.org/2007.asp>.
- [5] G. M. Whitesides and G. W. Crabtree, *Science*, **315**, 796 (2007).
- [6] G. Cody, T. Tiedje, in *Proc. 25th IEEE Photovoltaic Specialist Conf.* (1996), pp. 1521-1524.
- [7] Solarbuzz, *Marketbuzz 2007*, URL <http://www.solarbuzz.com/Marketbuzz2008-intro.htm>.
- [8] K. Zweibel, J. Mason, V. Fthenakis, A Solar Grand Plan, *Sci. Am.* **298**, 64 (2008), URL <http://www.sciam.com/article.cfm?id=a-solar-grand-plan> (2007).
- [9] M. A. Green, K. Emery, D. L. King, Y. Hisikawa, W. Warta, *Prog. Photovolt.: Res. Appl.* **14**, 45 (2006).
- [10] M. C. Beard, K. P. Knutsen, P. Yu, J. M. Luther, Q. Song, W. K. Metzger, R. J. Ellingson, and A. J. Nozik, *Nano Lett.*, **7**, 2506 (2007).
- [11] R. N. Bhattacharya, M. A. Contreras, B. Egaas, R. N. Noufi, *Appl. Phys. Lett.* **89**, 253503 (2006).
- [12] K. Ramanathan, M. A. Contreras, C. L. Perkins, S. Asher, F. S. Hasoon, J. Keane, D. Young, M. Romero, W. Metzger, R. Noufi, J. Ward, and A. Duda, *Prog. Photovolt.: Res. Appl.* **11**, 225 (2003).

[13] A. Luque and S. Hegedus, *Handbook of Photovoltaic Science and Engineering*, Hoboken (2003).

CHAPTER II

THIN FILM SOLAR CELL BACKGROUND AND SAMPLES STUDIED

2.1 Electrical properties of semiconductor

Solar cells convert the incoming sunlight into electrical energy by absorbing it in the semiconductor absorber layer. Photogenerated electron-hole pairs in the absorber layer are separated by the electric field gradient before they recombine. The material properties of the semiconductor determine how much photocurrent can be created, and these properties plus the field gradient of the pn junction formed by contacting two types of semiconductors determine how much voltage can be generated. In order to make a good solar cell we need to collect most of the photo-created charge carriers through the electrical contacts. Keeping in mind that minority carriers also need to be collected before they recombine with majority carriers in the space charge region, it is important that semiconductor have good electrical properties, such as long minority carrier diffusion length and high carrier mobility. Below is a brief background of the relevant semiconductor device physics, especially for p-type polycrystalline CIGS thin film solar

cells. More information on important principles and properties of semiconductors and solar cells can be found elsewhere [1-5].

2.2 Quantum mechanical interpretation of carrier transport

From a quantum mechanical perspective, transport mechanisms in semiconductors can be understood by band theory. The electronic band structure of a solid can be described as a continuous distribution of “allowed states” separated by “forbidden gap” of disallowed states. The band of allowed states is a set of solutions of the quantum mechanical eigenstates of electron wave function in the periodic crystal lattice. These states are given by the solution of a Schrödinger equation under a crystal lattice potential $V(\vec{r})$, e.g., $H\Psi_{nk}=E_{nk}\Psi_{nk}$ where H is a Hamiltonian operator consisting of kinetic energy of electron and $V(\vec{r})$. Since $V(\vec{r})$ is periodic, $V(\vec{r} + \mathbf{a}) = V(\vec{r})$, where \mathbf{a} is the unit lattice vector, so this determines the basic function of wave function Ψ_{nk} . This wave function solution in the periodic lattice is called a Bloch function, $\Psi_{nk} = e^{i\vec{k} \cdot \vec{r}} \times U_{nk}$. The first part of Bloch function is a plane wave solution and $U_{nk}(\vec{r})$ is a periodic wave function in the crystal lattice. The Schrödinger equation indicates there are a set of number k for an integer index n , and the energy eigenvalue E_{nk} . Since there are such a large number of electrons ($\sim 10^{23}$) with different eigenstates, the electronic energy structure is that of quasi-continuous allowed band of energy levels in either valence band or conduction band, but suddenly a forbidden energy gap appears in the middle for the semiconducting materials [6, 7].

However, the real situation in polycrystalline semiconductors is more complicated because large chemical fluctuations in stoichiometry and compositional disorder exist. In such a case the properties of these defects often dominates their electronic properties. Therefore, the identification and characterization of the electronic defect states in the forbidden energy gap must be developed to better understand the transport and optical properties in these disordered materials.

2.3 Material properties of polycrystalline CIGS thin film solar cell

Polycrystalline semiconductors maintain a reasonable degree of long range order within their micro-size crystalline grains. However, residual energy levels can exist and extend into this forbidden energy gap due to the polycrystalline nature. Whereas polycrystalline semiconductors have poorer transport and electronic properties compared to their single-oriented crystalline counterparts, polycrystalline CIGS films are found to have better properties than epitaxial single crystal films despite the existence of defects and imperfection at the grain-boundaries. Unlike the disorder-induced density of states (DOS) present in amorphous silicon, the types of defect structures at the grain-boundaries in CIGS and CdTe are believed to be benign to the solar cell operation [8, 9].

A number of sub-bandgap defect states have been identified in polycrystalline CIGS films [10]. These bulk defect states are intrinsically doped and are believed to be highly compensated. Most CIGS samples exhibit a well-characterized deep acceptor state lying 0.3 eV above the valence band. Early experimental results by Heath et. al.

showed the existence of a near mid-gap defect lying 0.8 eV above the valence band of the absorber, regardless of the gallium content [11]. Because mid-gap defects are more detrimental because they contribute more to the recombination, this defect at 0.8 eV above the valence band may become a dominant recombination center in CIGS films with a higher Ga content. The amphoteric nature of vacancy complexes also has been attributed to a possible recombination center through their conversion due to metastabilities in chalcopyrite solar cells [12].

Even the best CIGS materials exhibit a high level of compositional disorder, notably the non-stoichiometric Cu poor phase [5]. This mixed phase of compositional disorder is believed to result in a mixed phase nature at the nano-scale level, leading to a very complicated DOS structure for the CIGS materials. Such complex electronic structures are known to have significant consequences on photo-created carrier recombination processes within the bandgap of the materials so that the DOS structure plays a vital role in determining the electrical properties of the material and the device performance for the disordered materials. Furthermore, the photovoltaic application of CIGS somehow permits a variation of up to 10 % in the CIGS stoichiometry to be tolerated without significantly degrading its electronic properties. This leniency regarding compositional disorder is accompanied by a complicated DOS structure and metastable behaviors. Thus researchers have had enormous difficulty in obtaining a fundamental understanding of the basic electronic properties of CIGS materials.

Currently, in the development of CIGS based solar cell technologies, various CIGS industries are exploring alternative methods of material synthesis, such as electro-

deposition, RF sputtering, and ink-jet printing, because of their potential for reducing manufacturing costs and materials usage [13]. To aid in this development, there is a recognized need for more basic material research to better understand the role of defect states in chalcopyrite based thin film solar cells.

2.4 Samples for this study

Materials under study in this work include I-III-VI₂ chalcopyrite alloys commonly referred to as copper indium diselenide (CIS) or copper indium gallium diselenide (CIGS) when gallium is substituted for some of the indium in CIS. In ternary compounds of Cu-chalcopyrites there exist nine possible combinations of elements with a wide range of band gaps from 1.0 eV for CIS to 2.4 eV for copper gallium disulfide. Almost all samples in this thesis work are CIGS quaternary compounds.

All samples studied were deposited at the Institute of Energy Conversion (IEC) using elemental evaporation with no intentional grading of the composition of the films [14]. Devices are deposited on soda lime glass substrates coated with 1 μm thick molybdenum (Mo) as the back ohmic contact. About 2 μm thick CIGS absorber layers were then deposited using single step or bi-layer elemental 4-source evaporation techniques. Several samples were grown at substrate temperatures lower than the usual temperature of 550 °C for the possible application of polyimide substrates or as a tool to understand possible grain size effects on carrier mobilities or device efficiencies.

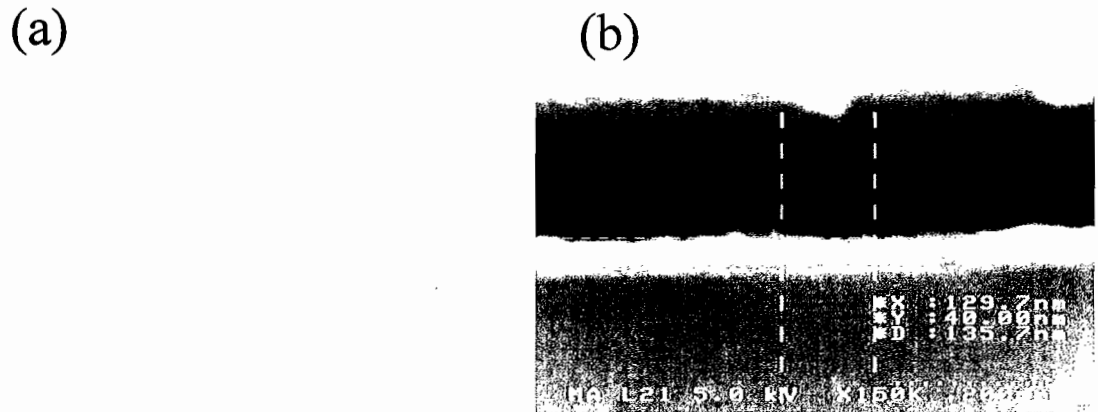


Fig. 2.1 Cross-sectional SEM image of CIGS thin film solar cells (a) Normal CIGS with 700 nm Mo. (b) Bifacial CIGS solar cell with 40 nm Mo.

Most samples for this study have the typical sandwich structure for a solar cell: Glass/Mo/CIGS/CdS/ZnO/Ni:Al grid. The CdS buffer layers with 30-40 nm thickness were deposited using a chemical bath deposition process. 50 nm undoped ZnO and 500 nm thick ZnO:Al were sputtered to form a transparent conducting oxide (TCO) layer. Finally, a Ni:Al grid was evaporated as the top contacts using an electron beam evaporation technique.

A couple depositions were used to fabricate semi-transparent bifacial CIGS solar cells. These were successfully deposited using thin Mo back contacts that allow light to penetrate from the back side as well as from the front. A 2 μm CIGS layer with a Ga fraction near 30 at.% was deposited on top of a 40 nm thin Mo with sheet resistance of 5 Ω/sq . The device performance of the bifacial CIGS solar cells was almost the same as that of the conventional thick Mo counterpart although thin Mo samples showed larger series resistance and lower fill factor. A particular bifacial CIGS sample #33873.22 had a fairly good efficiency of 12.8 %, although the standard 700 nm thick Mo device 33837.12

with the same bandgap of 1.2 eV had a higher efficiency around 17 %. While transmission at wavelengths between 780 nm and 980 nm was only about 4 %, illumination through the thin Mo back contact of the bifacial CIGS solar cell, the bifacial samples have allowed us to examine changes in the CIGS bulk absorber properties that exclude effects of charge trapping at the barrier interface and metastable changes in CdS layer.

Device performance as measured by IEC for CIGS, wide-bandgap CISSe and pentenary CIGSSe samples are given in Table 2.1. Electrical characteristics for solar cell operation were measured under AM1.5 solar spectrum. Carrier density, dielectric relaxation time, and hole carrier mobility were obtained by DLCP and high frequency admittance measurements.

Table 2.1. List of electrical characteristics for CIGS, CISSe and CIGSSe samples. Sample properties including substrate temperature during growth, absorber compositions, bandgap, and device performance were measured by IEC. Carrier density, dielectric relaxation time, and hole carrier mobility were obtained by DLCP and high frequency admittance measurements. Spatial non-uniformity in the free carrier density resulted in wide range uncertainty in hole carrier mobility determination.

Sample	T _{ss} (°C)	E _g (eV)	Ga (at.%)	η (%)	V _{OC} (V)	J _{SC} (mA/cm ²)	FF (%)	P (×10 ¹⁴ cm ⁻³)	ρε (ns)	μ _h (cm ² /Vs)
CIGS										
70008	550	1.0	0	9.53	0.41	34.17	65.6	8.8±0.6	2.5±0.2	2.9±0.3
24469	550	1.0	0	11.3	0.46	36.8	66.6			
24982	550	1.16	0.27	11	0.53	33.3	62.6			
24456	550	1.16	0.27	11.6	0.55	32.4	65	11±3	1.5±0.1	3.9±1.1
24427	550	1.18	0.29	14.5	0.61	31.7	74.7			
24934	550	1.18	0.3	14.9	0.63	30.6	76.8			
24400	550	1.2	0.32	16.1	0.65	33	74.8	8.2±0.5	1.1±0.1	7.2±0.8
24233	480	1.19	0.32	14.3	0.61	32.3	72.2	5.9±0.8	0.92±0.1	12±2.1
24264	400	1.2	0.32	11.8	0.6	29.5	65.7	4.8±1.1	0.77±0.0	18±4.0
33713	550	1.2	0.32	15	0.6	33	67.6			
24988	550	1.29	0.46	15.2	0.72	29.1	72.5			
24915	550	1.42	0.65	12.2	0.78	23.6	65.5			
24912	550	1.53	0.8	8.8	0.82	16.3	65.9			
Bifacial CIGS device										
33873.12		1.2	0.3	17	0.65	33	74.8			
33873.22		1.2	0.3	12.8	0.59	33.76	64.1			
33875.23		1.5	0.8	10	0.75	19.28	69.6			
33875.22		1.5	0.8	9.6	0.74	20.4	63.9			
Wide Bandgap Cu(In_xGa_{1-x})(Se_yS_{1-y})₂ Device										
Sample	Cu/III	Ga/III	S/VI	E _{gap} (eV)	Eff (%)	V _{oc} (V)	J _{sc}	FF (%)		
24160	0.91	0	0.33	1.2	9.4	0.48	29.24	67.6		
Pentenary Cu(In_xGa_{1-x})(Se_{~0.75}S_{~0.25})₂ Device Series										
24439	0.86	0.48	0.23	1.44	13	0.82	21.6	71.9		
24442	0.80	0.29	0.24	1.32	15	0.73	24.9	79.3		

Notes

- [1] S. M. Sze, *Semiconductor Devices, Physics and Technology* (John Wiley & Sons, Inc., 2002).
- [2] P. Blood and J. W. Orton, *The Electrical Characterization of Semiconductors: Majority Carriers and Electron States* (Academic Press, London, 1992).
- [3] J. W. Orton and P. Blood, *The Electrical Characterization of Semiconductors: Measurement of Minority Carrier Properties* (Academic Press, London, 1990).
- [4] A. L. Fahrenbruch and R. H. Bube, *Fundamentals of Solar Cells* (Academic Press, 1983).
- [5] S. Siebentritt and U. Rau, *Wide-Gap Chalcopyrites* (Springer, 2006).
- [6] N. W. Ashcroft and N. D. Mermin, *Solid State Physics* (Saunders, 1976).
- [7] Richard Zallen, *The Physics of Amorphous Solids* (John Wiley & Sons, Inc., 1983).
- [8] A. D. Compaan, *J. Metals* **59**, Iss. 12, p. 31 (2007).
- [9] M. Gloeckler, J. R. Sites, and W. K. Metzger, *J. Appl. Phys.* **98**, 113704 (2005).
- [10] B.J. Stanberry, PhD dissertation (University of Florida, Gainesville, 2001).
- [11] J. T. Heath, J. D. Cohen, W. N. Shafarman, D. X. Liao, and A. A. Rockett, *Appl. Phys. Lett.* **80**, 4540 (2002).
- [12] S. Lany and A. Zunger, *J. Appl. Phys.* 100, 113725 (2006).
- [13] H. W. Schock and R. Noufi, *Prog. Photovolt.: Res. Appl.*, **8**, 151 (2000).
- [14] W. N. Shafarman, R. Klenk, and B. E. McCandless, *J. Appl. Phys.* 79, 7324 (1996).

CHAPTER III

EXPERIMENTAL METHODS

3.1 High frequency admittance spectroscopy

The measurements employed in our studies include a set of experimental characterization techniques: (1) high frequency admittance spectroscopy, (2) drive level capacitance profiling, and (3) current-voltage measurements. A schematic experimental setup is illustrated in Fig. 3.1, and a brief introduction of each characterization method follows.

A novel experimental method to probe the electronic properties of carrier transport in working photovoltaic devices has been newly implemented in this work. This method utilized a high frequency admittance bridge covering the frequency up to 80 MHz. We used the high frequency lockin amplifier from Stanford Research covering the frequency range up to 200 MHz (SR844) and an arbitrary waveform synthesizer (Agilent 33250). Although Agilent 33250 limits the system bandwidth coverage only up to 80 MHz, it was a particularly convenient choice because it has a direct-digital-synthesizer (DDS) capability and so can provide an oscillating voltage of variable amplitude on top of a dc bias level without sacrificing 80 MHz bandwidth. The 200 MHz bandwidth

National semiconductor CLC 425 op-amp was configured as a current pre-amplifier. In order to reduce the capacitance signal loss in the high frequency regime, this current pre-amplifier had to be placed together within the sample probe. Another crucial part of measurement instrumentation was a micro-relay that could switch between a calibration capacitor and a sample. Furthermore, it could provide a direct bypass without going through the current pre-amplifier to measure dc current voltage (J - V) behavior. The entire high frequency probe assembly including the sample under study, current pre-amplifier circuit, and micro-relay, fit within a compact dimension of 1×2 cm. All these components were cooled altogether within our LN2 gas flow cryostat. This LN2 cooled gas flow cryostat dewar system enabled the reliable selection of temperature between 90 and 340 K with an accuracy of approximately ± 0.1 K. As a result, we were able to probe the high frequency response of the thermally activated admittance in the actual working photovoltaic devices. Data were taken using both GPIB and RS232 interfaces and then recorded by programs written in Visual C++ and Labview 7.0.

3.1.1 Admittance spectroscopy of CIGS and dielectric relaxation

Admittance spectroscopy is a well established technique that has been used to characterize the majority carrier traps present within the solar cell materials. It measures a frequency response of the capacitance and conductance at different temperatures and bias voltages. By analyzing steps and peaks in the capacitance and conductance respectively, we can determine features in the density of states distribution of defect

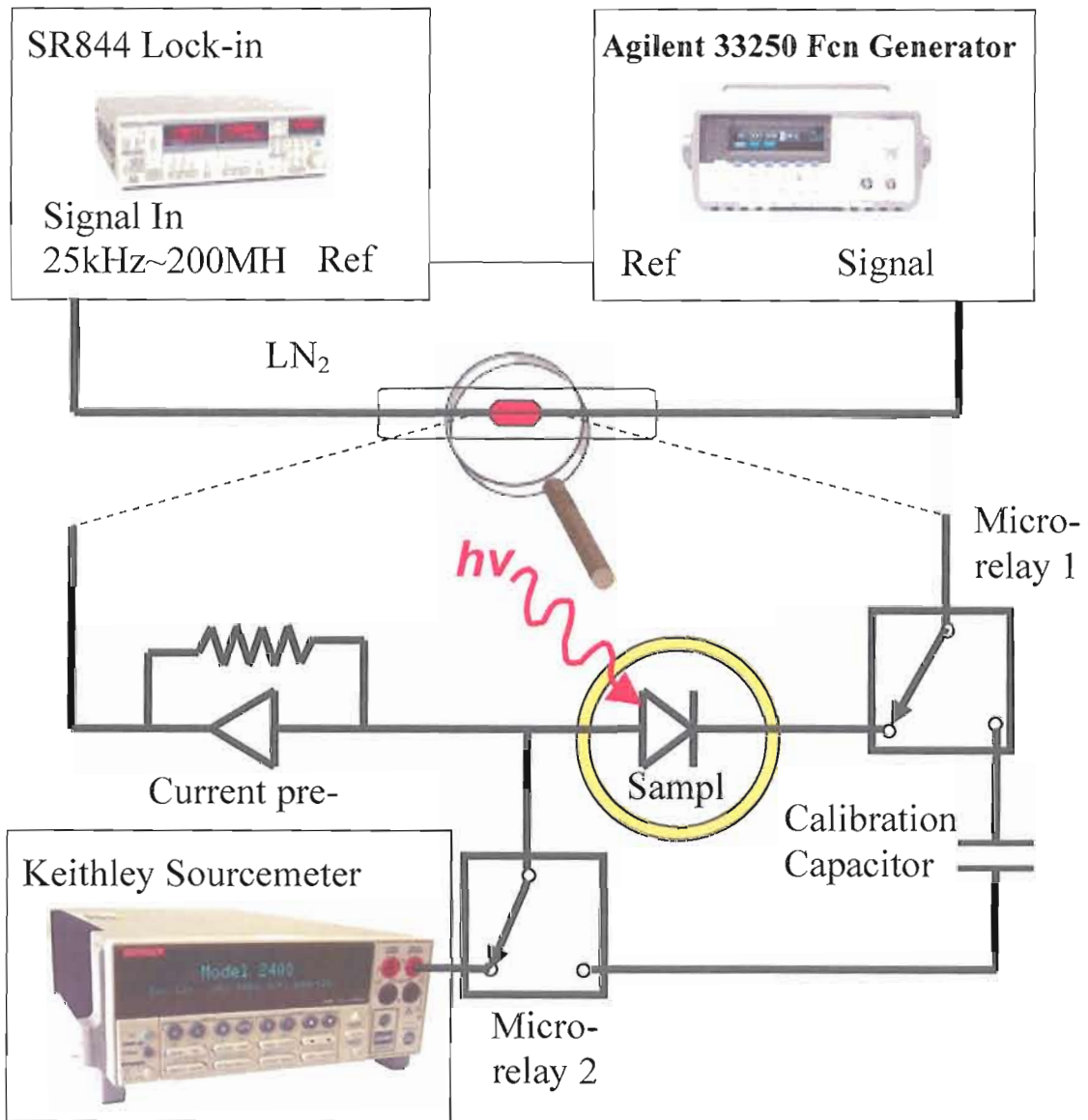


Fig. 3.1. Schematic of the experimental instrumentation.

states. The capacitance phase originates from the depletion layer in the junction, a region in the device where there is no free carrier which therefore acts as a dc blocking insulator. Conductance phase is the real part of admittance arising from the resistivity of the material, leakage of current, and mostly shunting in the depletion region.

Since admittance measurement is based on the junction capacitance of a pn junction or Schottky diode, admittance spectra can be modeled as an equivalent circuit consisting of the depletion capacitance C_d in series with a parallel combination of the rc circuit in the undepleted region. In Fig. 3.2 typical admittance spectra of CIGS 33400 at 175 K are shown. Clearly visible are two distinctive steps in capacitance that correspond to the contribution from the deep trap states and the free carrier response. The first capacitance step below 10 kHz arises from the deep defect response, coming from a band of deep defect states located roughly 0.3 eV above valence band maximum in the bulk CIGS absorber. Mid-region, between 10 kHz and 1 MHz, exhibits a nearly flat capacitance plateau. It corresponds to the depletion capacitance of the bulk CIGS junction, $C_d = \epsilon A/w$, where ϵ is the dielectric constant of the material, A is the area of the sample, and w is the width of the depletion layer. In addition to the defect related capacitance response freeze-out in admittance spectra, another sharp decrease in capacitance shows the dielectric relaxation above 2 MHz. This high frequency capacitance step can be clearly distinguished from other deep defect responses because it is a nearly temperature independent process and because the capacitance further decreases, and above 20 MHz, reaches down to the geometric capacitance, $C_g = \epsilon A/t$, where t is the thickness of the device. This high frequency step reflects the dielectric relaxation time of the CIGS layer, $\rho\epsilon$, where ϵ is the dielectric constant and ρ is the resistivity of the CIGS absorber.

We first employed the equivalent circuit analysis to deduce the dielectric relaxation time and hence the resistivity in the undepleted portion of the CIGS layer.

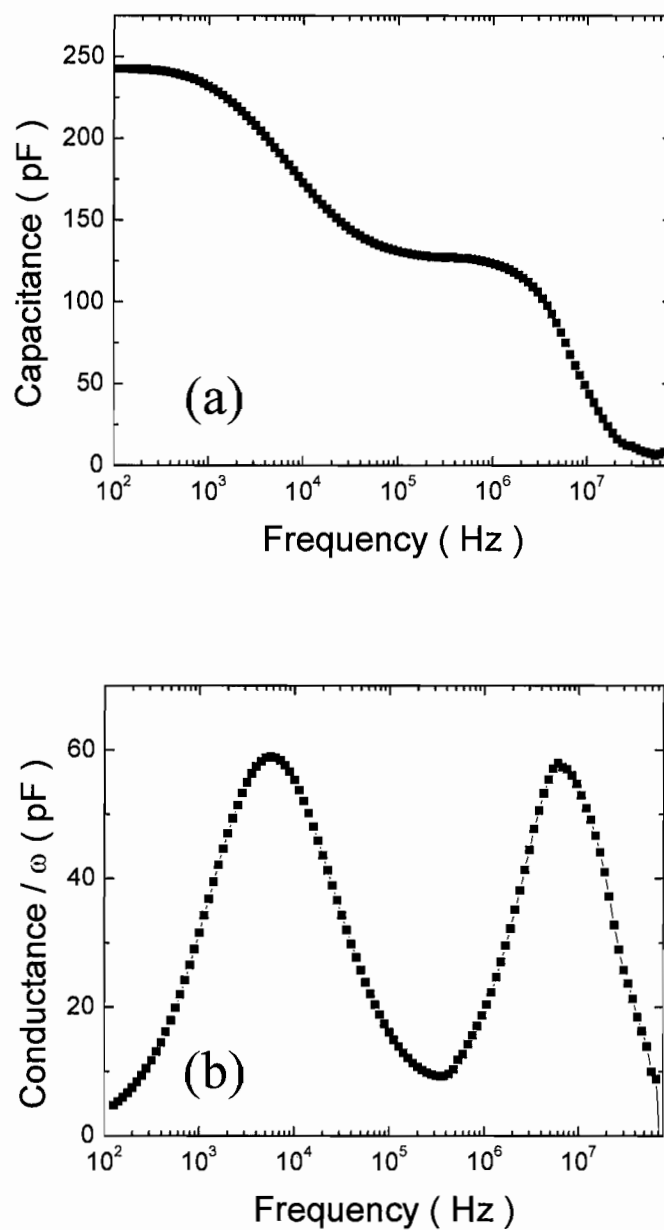


Fig. 3.2. Admittance spectra for CIGS #33400 have been measured at 175 K showing two distinctive steps. Low frequency step arises due to the contribution from the deep trap states and high frequency step corresponds to the dielectric freeze-out of the free carrier response.

An equivalent circuit model is shown in Fig. 3.3. We imagined the CIGS layer to consist of a set of very thin slabs of infinitesimal width, δx , connected in series with the depletion capacitance, C_d . Each slab consists of a capacitance, $c = \epsilon A / \delta x$, in parallel with a resistance, $r = \rho \delta x / A$, so that the rc time constant product of this parallel circuit simply equals $\rho \epsilon$, the dielectric relaxation time. The dielectric relaxation time is the characteristic time in which a charge motion in the material is able to respond to an external potential perturbation. Note that the shunt resistance at the depletion region can be ignored for simplicity in this modeling because it does not significantly affect the result. The actual dielectric freeze-out in the admittance spectra appeared only above frequencies of roughly 10 MHz since the majority carrier mobility is fairly large in polycrystalline CIGS absorber. In other words, the dielectric relaxation time was on the order of 1 ns, which is a timescale such that the undepleted part of the bulk absorber can not respond to the high frequency perturbation and so behaves as an insulator. The impedance of one of the infinitesimal slab is simply

$$Z_1 = \frac{r}{1 + i\omega\rho\epsilon} \quad (3.1)$$

where ω is an angular frequency. Since there will be a total $N(1-w/t)$ slices of infinitesimal width, each having impedance of Z_1 for the undepleted region of CIGS absorber, the total impedance of the semiconductor layer is

$$Z = \frac{1}{i\omega C_d} + \frac{N(1-w/t)r}{1 + i\omega\rho\epsilon} \quad (3.2)$$

$$= \frac{\omega(N(1-w/t)rC_d + \rho\epsilon) - i}{\omega C_d(1 + i\omega\rho\epsilon)} \quad (3.3)$$

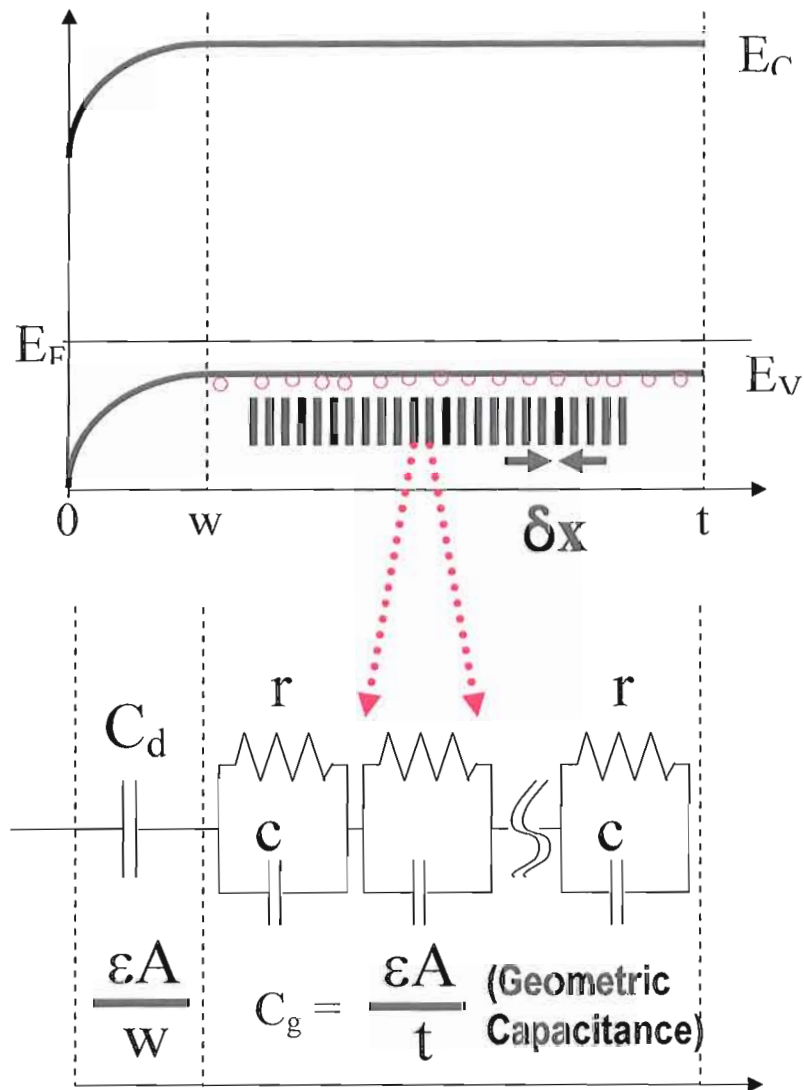


Fig. 3.3. Equivalent circuit model. Series of slabs of infinitesimal width δx , each having a capacitance, $c = \epsilon A / \delta x$, in parallel with a resistance, $r = \rho \delta x / A$, is connected in series with the depletion capacitance, $C_d = \epsilon A / w$. The rc time constant product of this parallel circuit equals a dielectric relaxation time constant $\rho \epsilon$ for the undepleted part of CIGS absorber.

Since capacitance is the imaginary part of the admittance, which is the inverse of the impedance, we readily obtain the frequency response of the capacitance and conductance in this equivalent model as follows:

$$C = \text{Im}(Y/\omega) = \text{Im}(Z^{-1}/\omega) \quad (3.4)$$

$$= \text{Im}\left(\frac{C_d(1+i\omega\rho\varepsilon)}{\omega(N(1-w/t)rC_d + \rho\varepsilon) - i}\right) \quad (3.5)$$

$$= \text{Im}\left(\frac{Cd(1+i\omega\rho\varepsilon)}{\omega(C_d/C_g)(\rho\varepsilon)^2 - i}\right) \quad (3.6)$$

$$= C_d \frac{\omega^2(C_d/C_g)(\rho\varepsilon)^2 + 1}{\omega^2(C_d/C_g)^2(\rho\varepsilon)^2 + 1} \quad (3.7)$$

$$= \begin{cases} C_d & \omega \rightarrow 0 \\ C_g & \omega \rightarrow \infty \end{cases} \quad (3.8)$$

$$\text{and } G = C_d \frac{(C_d/C_g - 1)\rho\varepsilon\omega^2}{(C_d/C_g)^2(\rho\varepsilon)^2\omega^2 + 1} \quad (3.9)$$

Simple substitution has been used to convert geometric relation into capacitance in this calculation

$$\frac{t}{w} = \frac{C_d}{C_g} \quad (3.10)$$

since,

$$C_d = \frac{\rho\varepsilon}{N\frac{w}{t}r}, \quad \text{and} \quad C_g = \frac{\rho\varepsilon}{Nr} \quad (3.11)$$

As shown in Eq. 3.8, we note that this equivalent circuit analysis of the parallel rc network model fulfills the boundary condition for both the capacitance and conductance phases as frequency approaches the asymptotic limits of zero or infinity. Capacitance in the low frequency region becomes the depletion capacitance and approaches the

geometric capacitance in the high frequency limit. The conductance phase shows a peak when there is a step in capacitance phase. At both frequency limits the conductance phase disappears to zero. An example of the equivalent circuit analysis to fit actual high frequency admittance data is shown in Fig. 3.4 using Eq. 3.7 and Eq. 3.9. Excellent fits to the admittance data were obtained for two different values of dc bias. The reverse bias admittance spectra were fitted even better due to a reduced contribution from the deep defect response at the lower frequency as the probing edge of the depletion region moved farther away from the junction interface. While the fitted value of $\rho\epsilon$ remained constant at 1.15 ns, the peak in conductance moved to a higher frequency as the depletion capacitance decreased. That is, the change in peak position with reverse bias arises because the depletion capacitance decreases as reverse bias is applied. The shift in peak frequency in the conductance phase can be proven analytically using the Kramer-Kronig relationship by taking a second derivative of Eq. 3.7 with respect to angular frequency so that the peak in the conductance phase will occur at the same frequency at the inflection point in the capacitance phase [1]. Specifically,

$$\omega_{peak} = \frac{1}{C_d / C_g \rho\epsilon} \quad (3.12)$$

Furthermore, we have considered the influence of an additional series resistance in the dielectric relaxation model. Although the equivalent circuit analysis with an additional series resistance makes the calculation a bit more complicated, it turns out to modify only the value of the high frequency response in this dielectric relaxation approximation. That is, for an assumed series resistance R_s

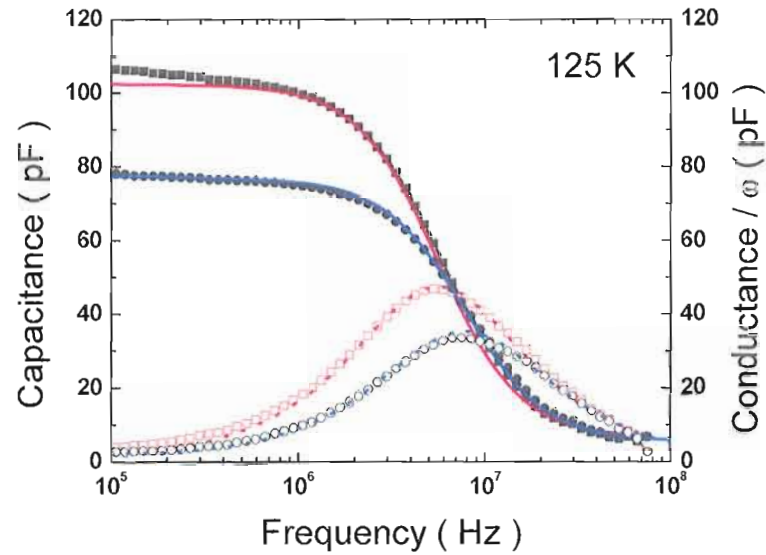


Fig. 3.4. High frequency capacitance (solid symbols) and conductance (open symbols) data on CIGS sample #33456 at 125 K and two different values of applied bias. In fitting the admittance data at two different biases, same values of $\rho\epsilon$ were obtained.

$$C \rightarrow C_g \frac{1}{\left(1 + \frac{R_s C_g}{\rho\epsilon}\right)^2} \quad \text{as } \omega \rightarrow \infty \quad (3.13)$$

Since the dielectric time constant is in the order of 1 ns, even a small series resistance will significantly modify the capacitance response in the high frequency limit in this second order approximation. As a consequence, any additional series resistance will cause the inferred geometric capacitance to be greatly attenuated around the dielectric relaxation frequency.

3.1.2 Density of states in the bandgap

It has long been known that there exist energy levels, the so-called the density of states (DOS) within the bandgap of semiconductors. We define DOS to be a function of energy, $g(E)$, such that the $g(E)dE$ represents the number of states per unit volume with energies between E and $E+dE$. CIGS related compounds are polycrystalline materials, i.e. materials that contain a variety of crystal orientations with many grain boundaries. Even the highest quality CIGS materials are believed to contain large intrinsic fluctuations in stoichiometry and compositional disorder. Such fluctuations in addition to the polycrystalline nature results in a complicated DOS structure for the CIGS materials.

Standard UV/visible/infrared optical measurements are a typical tool for characterizing the DOS within a thin film solar cell material [2]. Spectroscopic absorption or transmission measurements are often performed to examine the electronic structure of a material. For example, a spectroscopic ellipsometry technique is unique in its ability to measure the complex refractive index or dielectric constants using phase sensitive detection. However, conventional optical measurements fall short of characterizing sub-bandgap DOS and their effect on device performance.

Instead several sub-bandgap absorption measurements have been developed and applied to determine the DOS within the bandgap for amorphous silicon, such as photo-thermal deflection spectroscopy (PDS), constant photocurrent method (CPM),

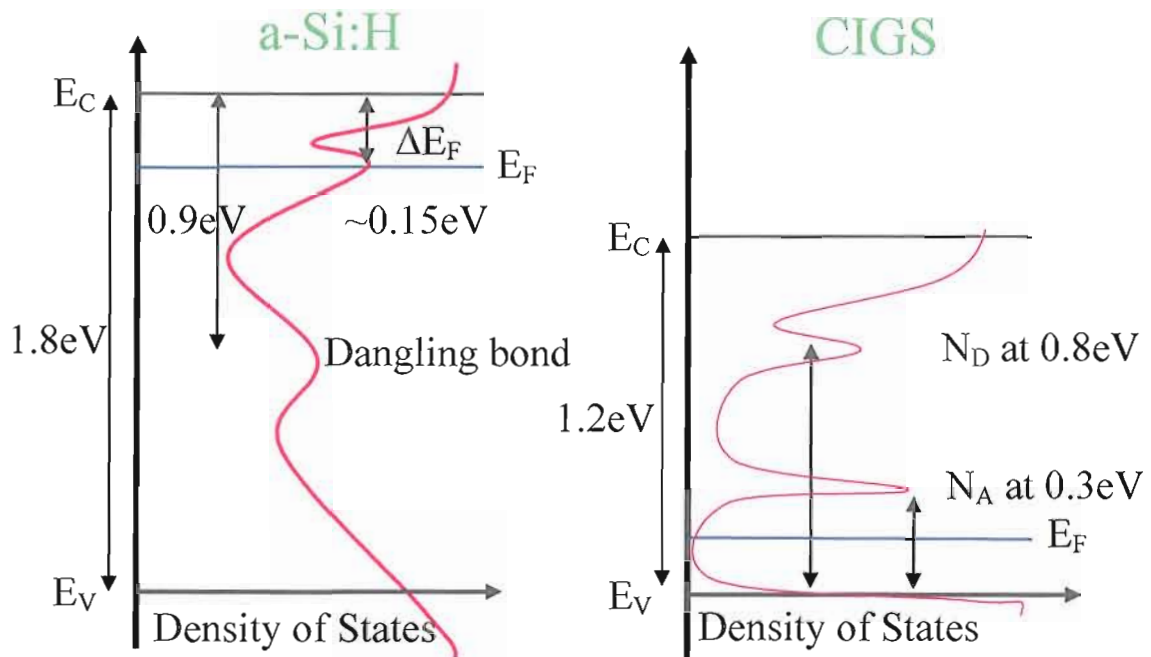


Fig. 3.5. Density of states schematic diagram for a-Si:H and CIGS. (1) a-Si:H: Fermi level (E_F) is pinned on defects in the conduction bandtail states and carrier density is thus thermally activated at $\Delta E_F = E_C - E_F$. (2) CIGS: Between the N_A defect state and the valence bandtail states, DOS is too small to pin the E_F . Thus, E_F changes with temperature to maintain a constant free hole carrier density.

and transient photocapacitance (TPC) [3]. These measurements can be applied to the thin film solar cells in their working device configuration, as opposed to the bare materials for the typical optical measurement so that features in DOS can be less ambiguously correlated with their device configuration. Although sub-bandgap absorption measurements have many advantages in studying DOS in that they yield both quantitative and spatially resolvable defect distribution, by far more sensitive measurement techniques are required for the detailed study of DOS of CIGS-related materials [4].

3.1.3 Numerical modeling by SCAPS-1D

Numerical simulations were made with the latest version 2.7 of SCAPS-1D software, a Solar Cell CAPacitance Simulator in 1 Dimension, developed by researchers at University of Gent [5]. The program SCAPS finds numerical solutions for the baseline solar cell structure consisting of several semiconductor layers with different energetic distributions of deep defects states. An example is given in Fig. 3.6.

In addition to calculating the model cell efficiency, we were able to fit the experimentally obtained thermal admittance spectra using SCAPS modeling without donor defect states. High frequency AS at different temperatures was successfully simulated in Fig. 3.7. The acceptor defect with single discrete energy level at 0.3 eV above the valence band was used as a recombination center and fairly good agreement between our simulated results and our experimental data was obtained. Furthermore, the conductance phase can be fitted well simultaneously by applying the Kramers-Kronig relationship to the SCAPS capacitance fit.

A fairly extensive baseline SCAPS model was developed to account for the admittance spectra and current-voltage ($J-V$) curves at the same time whose band diagram is shown in Fig. 3.6. This baseline model incorporates the hole carrier mobility information which was found through the nonlinear square fitting of the high frequency admittance spectra using the equivalent circuit analysis of Eq. 3.6 and Eq. 3.8, as previously shown in Fig. 3.4. A single discrete energy distribution for a deep defect was

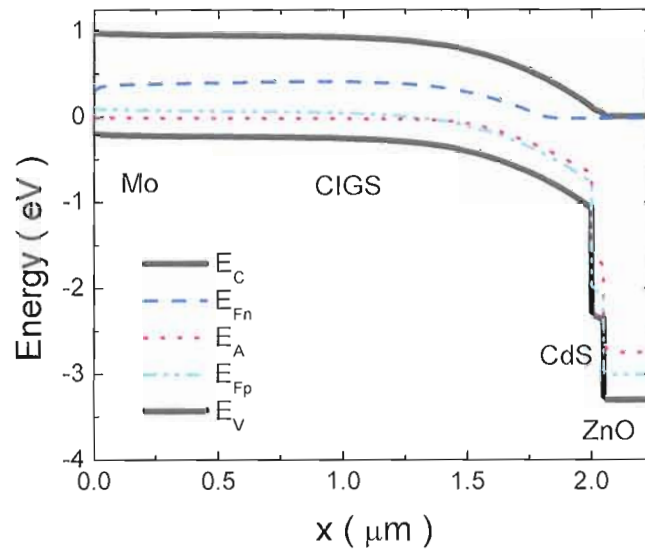


Fig. 3.6. Band diagram for CIGS solar cell under front illumination of 100 mW/cm^2 at 300 K.

used in the SCAPS modeling. The measured temperature dependence of admittance spectra (symbols) was then successfully fitted (lines) as shown in Fig. 3.7 under 0 and -1 V bias condition. The parameters used to fit the admittance spectra are listed in Table 3.1. Note that we had to vary slightly the capture cross-section and energy position of the defect state to match the admittance spectra to reproduce the observed temperature dependence. Therefore there is a more complex thermal emission behavior from the defect, such as a thermal barrier to carrier capture. However, we assumed a constant temperature independent carrier density and mobility in the simulation.

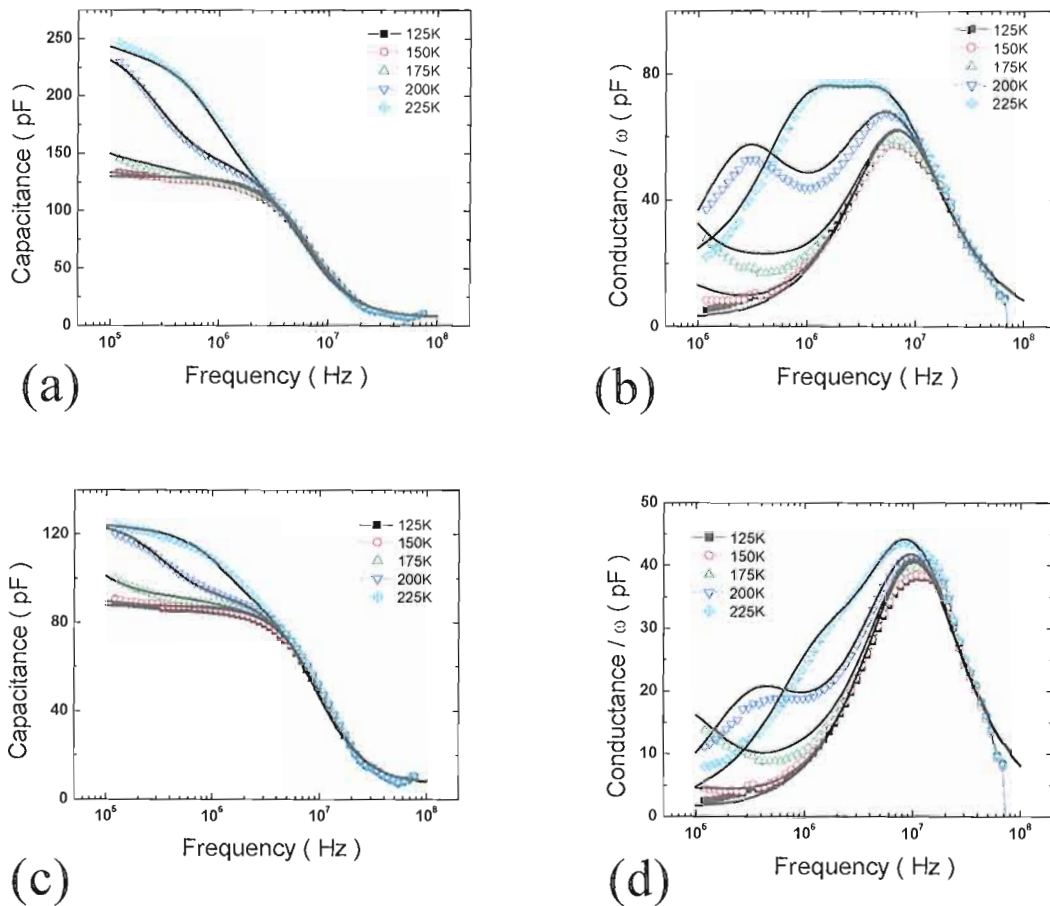


Fig. 3.7. Admittance spectra (symbols) for CIGS #33400 as a function of temperature and bias voltage. SCAPS modeling (lines) with single discrete energy distribution of defect states fits well for both 0 and -1 V bias condition.

Table 3. 1. SCAPS parameters used to fit admittance spectra in Fig. 3.7

Hole mobility μ_h (cm^2/Vs)	Hole carrier density (cm^{-3})	Defect density (cm^{-3})	Defect energy (eV)	Emission prefactor (sec^{-1})
7	6×10^{14}	2.4×10^{15}	0.185	5.5×10^{10}

Temperature dependence of AS suggests that the conductivity of the CIGS material is nearly temperature independent at least for the lower temperature region below 225 K. Note that the hole mobility and carrier density are temperature independent in SCAPS simulation. Varying the hole carrier density with temperature significantly overshoots depletion capacitance in the high frequency region or affects the dielectric relation frequency significantly.

3.2 Drive level capacitance profiling

Capacitance-voltage (CV) measurements across a semiconductor diode junction are one of the most commonly used techniques to obtain the carrier density and built-in potential (V_{bi}). The simplest analysis of an abrupt pn junction assumes a constant carrier density throughout the depletion region in the same manner as in the metal-semiconductor contact [6]. If carrier density is not uniform over the thickness of the semiconductor layer, the differential capacitance method can be used to determine the doping profile, and then the carrier density can be plotted as a function of the depletion width w from the CIGS/CdS barrier junction, which is given by

$$w = \sqrt{\frac{2\varepsilon(V_{bi} - V_a)}{qN_A}} \quad (3.14)$$

where q is the electron charge, ε is the dielectric constant of the material, V_{bi} is the built-in potential, V_a is the applied bias, N_A is the charge density in the p-type semiconductor. The corresponding depletion capacitance is then given by

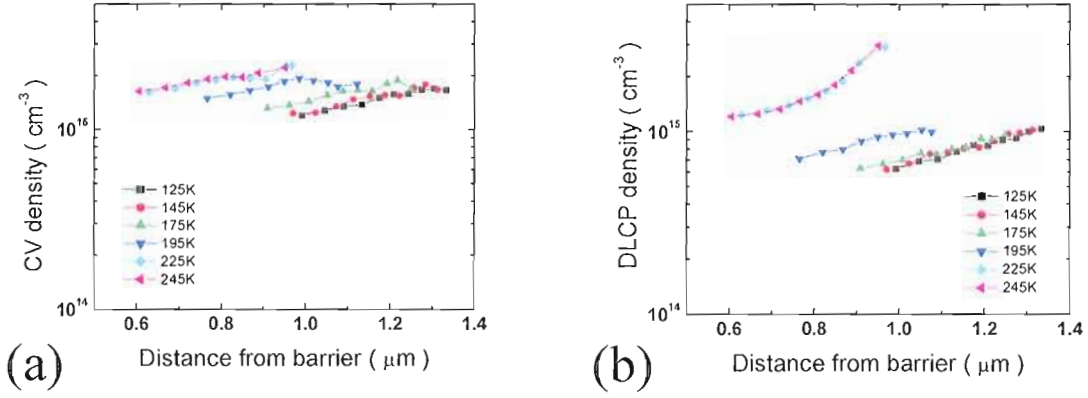


Fig. 3.8. Comparison of CV and DLCP for CIGS #333400 measured at 1 MHz. Voltage bias from -1 V down to 0 V with 0.1 V step.

$$C = \frac{\epsilon A}{w} \quad (3.15)$$

where A is the surface area of the sample. Combining Eq. 3.14 and Eq. 3.15, the acceptor density N_A in the bulk CIGS is given as

$$N_A = -\frac{C^3}{q\epsilon A^2} \left(\frac{dC}{dV} \right)^{-1} = \frac{2}{q\epsilon A^2} \left(-\frac{1}{d(1/C^2)/dV} \right) \quad (3.16)$$

However, there is a problem with the CV method if deep defect states exist within the bandgap. This situation introduces an additional capacitance response within the depletion region so that free carrier density can be greatly overestimated even when measured at high frequency and low temperature. Also, CV density will be greatly affected when there are densities of interface states. The effect of such interface states has been simulated previously for the case of a broad Gaussian band of deep acceptor states near the barrier interface [9, 10].

Drive level capacitance profiling (DLCP) measurements can be used to obtain the true free carrier density as a function of position throughout CIGS film. That is because at sufficiently high frequencies and temperatures the DLCP density receives little contribution from the deep trap states. Therefore, in order to determine the shallow acceptor density in the absorber layer of CIGS solar cells, we performed DLCP measurements at frequencies just below the dielectric freeze-out condition. For an accurate determination of the carrier density by this method it is important that the Fermi energy not be pinned within a region of high DOS in the bandgap. Typically, 1 MHz DLCP measurements at 150 K was well below the freeze-out condition. Although both the CV and DLCP typically showed a distinct spatial variation in the shape of profiling, the estimated free carrier density from the DLCP was always lower by a factor of two lower compared to the CV density. We attribute this difference in the different sensitivity of CV and DLCP to the deep trap density at particular measurement condition [8, 11].

Although the conventional CV method had previously been used to obtain the free carrier density, depletion width and deep trap density in CIGS, information about their spatial variation within the pn junction was not easily understood. Indeed, one major group in the CIGS community continues to argue that deep traps must be associated with interface states or at least with an ordered vacancy complex near interface region [12]. These arguments are based on experimental results that indicated that deep trap response can be altered by the surface treatments [13]. However, since the DLCP technique can clearly distinguish the bulk states response

from the interface effects, there is no doubt that interface states cannot account for the DLCP profiles extending far into the bulk region of the CIGS layer.

3.2.1 Determination of the majority carrier mobility

We have been able to deduce hole mobilities in the undepleted region of the CIGS polycrystalline films in the working solar cell configuration [5]. Although hole mobilities of the CIGS have been determined in the traditional manner using the Hall effect in conjunction with resistivity measurements, such measurements require insulating substrates with coplanar contacts geometry. Instead, we were able to deduce that the hole mobility of CIGS material was typically about $10 \text{ cm}^2/\text{Vs}$ at 150 K and was not strongly temperature dependent. The DC conductivity in a semiconductor is given by

$$\sigma = qp\mu \quad (3.17)$$

so that

$$\mu = \frac{\varepsilon}{qp(\rho\varepsilon)} \quad (3.18)$$

where σ is conductivity, p is the free hole carrier density, ρ is resistivity, and μ is the mobility of the material.

Hole mobilities in CIGS films do not seem to be well correlated to the solar cell performance. Furthermore, hole mobilities for samples grown at lower substrate temperature turned out to be higher [14]. Since lower substrate temperature is

believed to cause more structural disorder in the polycrystalline material, higher hole mobilities for samples grown at lower substrate temperature tends to be contradicted by their lower conversion efficiencies. Therefore, performance of CIGS solar cells is not likely to be mobility-limited, because majority carrier mobilities are high enough to guarantee the electrical transport. However, even high efficiency CIGS solar cells actually suffer a loss in the short circuit current J_{SC} and open circuit voltage V_{OC} due to the recombination in the space charge region if combined with relatively low mobility in practice, especially when the metastable changes take place to modify the rate of recombination process and hole carrier mobility by the conversion of charge state of $V_{Se}-V_{Cu}$ defect complex [11].

3.2.2 Distinguishing free carrier density from bulk defect states

As shown in Fig. 3.8, 1 MHz DLCP below 200 K is independent of temperature and its spatial variation becomes smaller. In this regime, the DLCP profile indicates the spatial variation of the shallow dopant because most of the deep states can not follow the fast applied perturbation within the time scale of

$$\tau = \frac{1}{\omega} = \frac{1}{\nu_0} \exp(E_e / kT) \quad (3.20)$$

where ω is angular frequency of the perturbation, ν_0 is the attempted-to-escape frequency, E_e is the limiting energy for the carrier transport.

3.3 Current-voltage curve characteristics

The current-voltage (J - V) curve measurement is the most common characterization technique for determining solar cell performance. Current is measured as a function of applied voltage in both dark and light condition. The light J - V curve is shifted down into the fourth quadrant because the photocurrent gives rise to the power generation. Since CIGS is p-type semiconductor, hole carriers move toward the back contact under illumination. As more forward bias is applied, the current starts to flow in the opposite direction and becomes positive. The forward bias at which no current flows is called the open circuit voltage V_{OC} , and when applied voltage is zero, the current is called the short circuit current J_{SC} . The power delivered is simply the voltage times the current, with the maximum power density occurring at $P_m = J_m \times V_m$. The fill factor FF is also an important parameter as is the energy conversion efficiency η . Since it is difficult to measure η directly, FF is often used to define the overall performance of a solar cell in the laboratory characterization. Whereas FF is rather immune to the light intensity, η increases for the concentrated system because V_{OC} increases logarithmically with the light intensity while J_{SC} is linear to the light intensity. These are defined by

$$FF \equiv \frac{P_m}{V_{OC} J_{SC}} \quad \text{and} \quad \eta = P_m / P_{in} \quad (3.21)$$

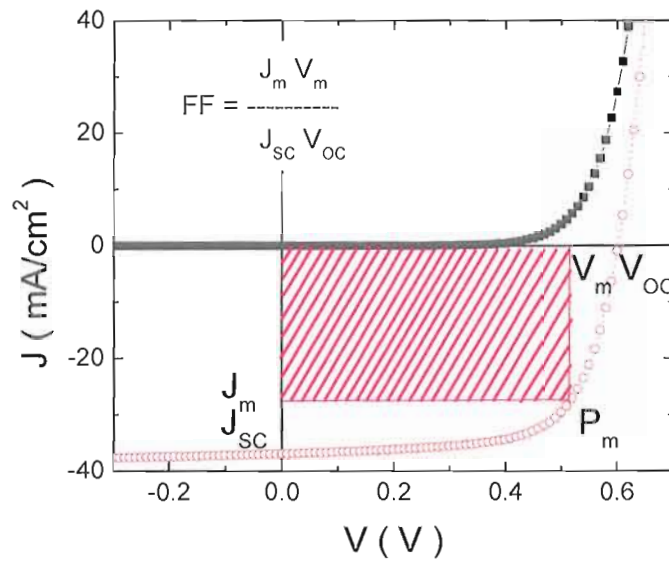


Fig. 3.9. Typical example of J - V curve characteristics under AM1.5 standard illumination condition, $100\text{mW}/\text{cm}^2$ at 25°C . The fill factor is 67.6 % and the cell efficiency is 15 % for CIGS #33400.

where P_m is the input illumination power at typically 1 sun or $100\text{ mW}/\text{cm}^2$. A typical J - V curve is shown in Fig. 3.9 at RT under AM1.5 standard 1 sun illumination condition.

3.3.1 Ideal diode equation analysis

The ideal case for the current-voltage under light is given by

$$J = J_0(\exp(qV / AkT) - 1) - J_{sc} \quad (3.22)$$

where J_0 is the diode current density and A is the ideality factor of the solar cell. In general there are several non-ideal feature that affect J - V curve characteristics for

solar cell operation. These parasitic loss factors include series resistance R , shunt conductance G , and diode ideality factor A . The standard (non-) ideal J - V curve analysis used in this work follows the practical procedure described elsewhere [15]. An example of J - V curve is shown in Fig. 3.10. Typical analysis procedures were performed following four steps and plots:

(a) The raw J - V curves in the dark and under AM1.5 (strong daylight equivalent) illumination

(b) A plot of dJ/dV near J_{SC} to determine the shunt conductance

(c) A plot of $dV/dJ = R + \frac{AkT}{q}(J + J_{SC})^{-1}$ against $(J + J_{SC})^{-1}$

(d) A semi-logarithmic J - V plot against $V - RJ$ to identify A by an alternative way

While typical values for the ideality factor lie in the range between 1.3 and 2 as shown in Fig. 3.10(c), A can be even larger than 2 in most of cases. Higher values of A are often attributed to the presence of the deep defects as recombination centers in the bulk CIGS [16]. Note that there are some discrepancies when determining the ideality factor and other device parameters from the dark and light condition.

We developed a simple experimental alternative method to evaluate the ideality factor A using the light dependence in V_{OC} . Assuming that J_{SC} is linearly proportional to the light intensity, the ideality factor can be deduced simply from the

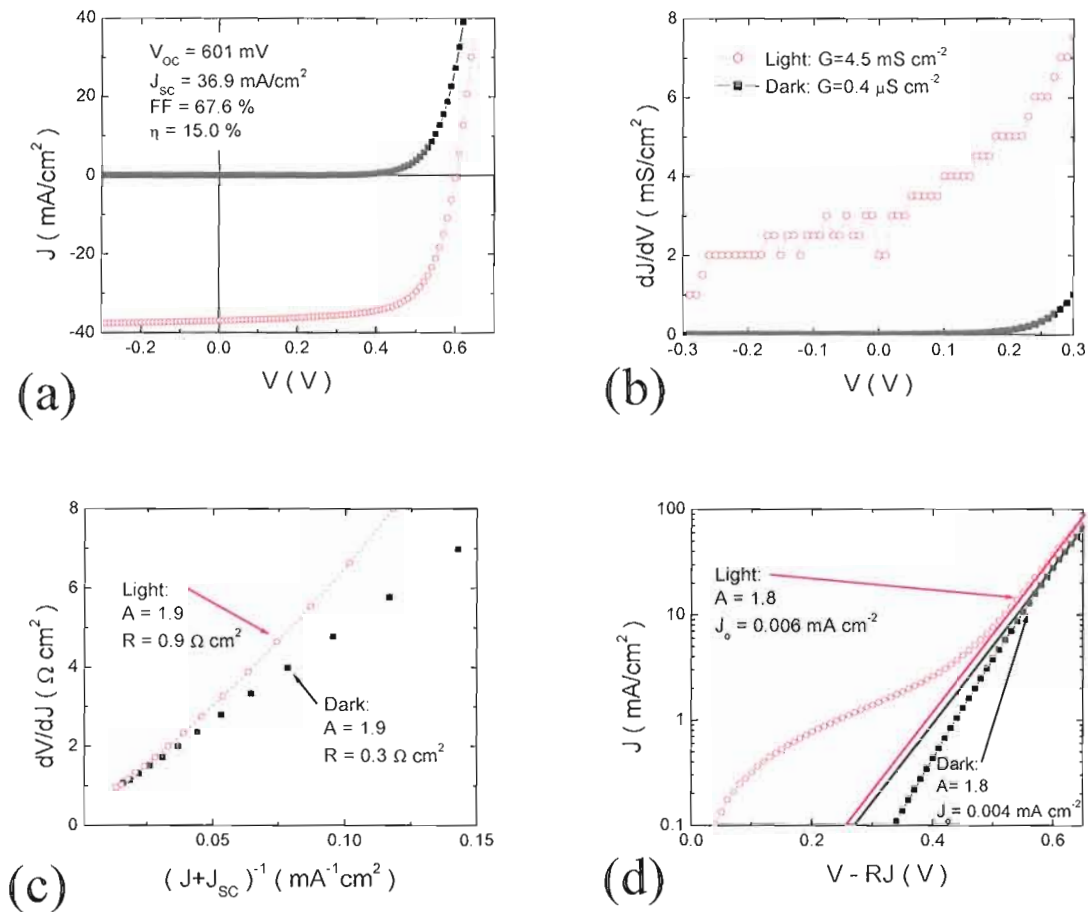


Fig. 3.10. Light and dark J - V curve characteristics of typical CIGS cell: (a) standard J - V plot (b) shunt characterization (c) derivative resistance plot against $(J+J_{SC})^{-1}$ to determine ideality factor A and series resistance R (d) typical semi-logarithmic plot of $J+J_{SC}$ against $V-RJ$ using R obtained from the fit in (c).

light intensity dependence of V_{OC} . At open circuit condition, ideal J - V curve

becomes

$$J = J_0(\exp(qV_{OC}/kT) - 1) - J_{sc} = 0 \quad (3.23)$$

so that

$$A = \frac{q}{kT} \frac{dV_{OC}}{d \ln(Int)} \quad (3.24)$$

where Int is the light intensity which is linearly proportional to J_{SC} . As shown in Fig. 3.10(b), semi-logarithmic dependence against light intensity confirms the previously determined value of the ideality factor in Fig. 3.10(c). Fig. 3.11(a) shows the validity of the linear relationship assumption between J_{SC} and light intensity in the modeling.

Fig. 3.11(c) shows the temperature dependence of V_{OC} assuming that the diode current J_0 is given by

$$J_0 = J_{00} \exp\left(-\frac{\Phi_b}{AkT}\right) \quad (3.25)$$

The temperature dependence of the V_{OC} does not show any tendency of saturation at a low temperature regime in SCAPS modeling. Since the offset at zero Kelvin temperature gives the barrier height at the CIGS/CdS interface, a linear fit to the modeling data in Fig. 3.11(c) clearly indicates that the dominant recombination center is in the CIGS absorber layer. This could have two possible consequences. Because SCAPS modeling does not include any additional interface defect, the interface defect state needs to be considered to explain the actual V_{OC} saturation at temperature lower than 200 K, possibly associated with pinning of the electron quasi-Fermi level at the cliff-like conduction band offset at the interface. Second, the linear fit of experimental $V_{OC} \rightarrow E_g/q$ as $T \rightarrow 0$ means that there is not a Fermi level pinning mechanism at the interface states regarding the lack of V_{OC} for the wide bandgap chalcopyrite case. Therefore, a large number of bulk defect states can be predicted to pin the quasi-Fermi level splitting at low temperature.

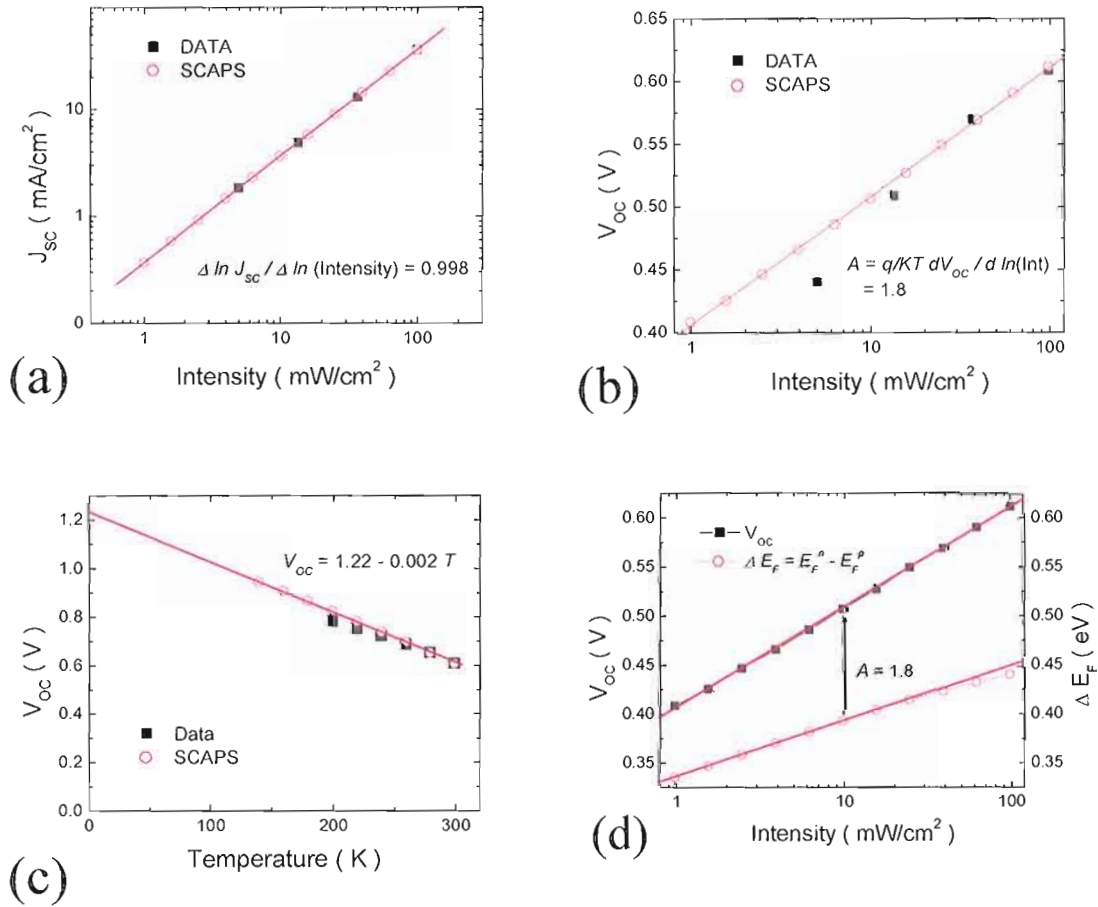


Fig. 3.11. Intensity and temperature dependence of V_{OC} for the bifacial CIGS #33873.22 and the baseline SCAPS model (a) Showing J_{SC} is linearly proportional to light intensity (b) V_{OC} depends logarithmically with light intensity. A linear fit used to determine the diode ideality factor A (c) The temperature dependence of V_{OC} shows that $V_{OC} \rightarrow Eg/q$ (1.22 V for CIGS bandgap) as $T \rightarrow 0$ (d) A comparison of the intensity dependence of V_{OC} and quasi-Fermi level splitting in the middle of CIGS absorber showing the apparent slope difference by a factor of A .

Fig. 3.11d shows that the slope of V_{OC} against light intensity is determined by a spatially homogeneous recombination center in the bulk CIGS film. It is helpful to note that the difference between the slopes of the quasi-Fermi levels splitting in the middle of CIGS device is larger by exactly the ideality factor compared to the one of

the intensity dependence of V_{OC} . This is true for the following reason: for the quasi-steady-state, the electron density is determined by the condition that the generation rate, G , be equal to the recombination rate, R ,

$$G = R \propto N_R np \quad (3.26)$$

where N_R is the density of the recombination center participating a bimolecular recombination process, and that G is proportional to the light intensity. Since the quasi-Fermi level of holes is less susceptible to changes in light intensity, most of the intensity dependence of the quasi-Fermi level splitting comes from the change in the quasi-Fermi level of electrons. The intensity dependence of quasi-Fermi level splitting is readily available from the change in the electron density

$$n = N_C \exp\left(\frac{E_C - E_{Fn}}{kT}\right) \quad (3.27)$$

$$E_C - E_{Fn} = kt \ln \frac{n}{N_C} \propto kt \ln \frac{G}{pN_R} \quad (3.28)$$

where N_C is the effective density in the conduction band and E_{Fn} is the quasi-Fermi level of electrons. From the above relation,

$$\frac{d(E_C - E_{Fn})}{d \ln(Int)} = kT \quad (3.29)$$

In contrast to the intensity dependence of V_{OC} , the quasi-Fermi level splitting does not contain any ideality correction factor in thermal energy. That semi-logarithmic intensity dependence of quasi-Fermi level splitting in Eq. 3.29 is obeyed means that bimolecular recombination process takes place at the spatially homogeneous bulk defect states in the CIGS.

3.3.2. Red kink effect in the near-infrared current-voltage curves

We typically measured the I - V curve characteristics using sources of 780 nm and 980 nm monochromatic near-infrared light at intensity of 50 mW/cm² or 100 mW/cm². These sources were used in part because normal sources of white light cause additional metastable effects in the CdS buffer layer. The same near-infrared light sources and light intensities were used in light-soaking. However, using such near-infrared light sources also resulted in the so-called “red kink” effect because photon energies lie below the CdS bandgap and so do not produce enough photoconductivity for the carrier transport in the CdS layer [17]. As shown in Fig. 3.12 the absence of sufficient photoconductivity significantly distorted the I - V curves. It turned out that V_{OC} did not change even with the red kink effect, only FF does [18]. Red kink effect can not be understood simply as a series resistance effect. It could rather be interpreted as a back-to-back diode model if there is another diode in reverse direction. However, we found that by adding a very weak UV light at a wavelength of 254 nm the red kink problem can be suppressed without affecting either the short circuit current or the open circuit voltage [11, 18]. It is worth noting that the red kink effect might entail a serious loss mechanism for the application of tandem solar cells.

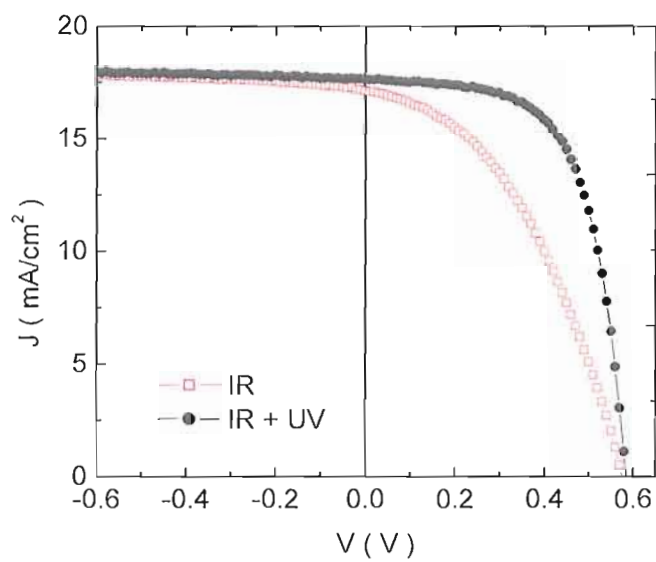


Fig. 3.12. Red kink effect (open symbols) and UV curing method (solid symbols) for the near-infrared light I - V curves.

Notes

- [1] P. Y. Yu, M. Cardona, *Fundamentals of Semiconductors* (Springer, 1996), 3rd ed.
- [2] J. D. Cohen, A. V. Gelatos, *Amorphous Silicon and Related Materials* (World Scientific, 1988), p. 475.
- [3] H. Ibach, H. Lüth, *Solid-State Physics* (Springer, 2003), 2nd ed.
- [4] N. Peyghambarian, S. W. Koch, and A. Mysyrowicz, *Introduction to semiconductor optics* (Prentice-Hall, 1993).
- [5] M. Burgelman, P. Nollet and S. Degrave, *Thin Solid Films* **361-362**, 527 (2000).
- [6] S. M. Sze, *Physics of Semiconductor Devices* (John Wiley & Sons, 1981), 2nd ed.
- [7] J. T. Heath, W. N. Shafarman, and J. D. Cohen, *J. Appl. Phys.* **95**, 1000 (2004).
- [8] J. Lee, J. T. Heath, W. N. Shafarman, and J. D. Cohen, in *Materials Research Society Proc.* **865**, F12.4.1 (2005).
- [9] A. Niemegeers, M. Burgelman, R. Herberholz, U. Rau, D. Hariskos, and H. W. Schock, *Prog. Photovolt.: Res. Appl.* **6**, 407 (1998).
- [10] R. Herberholz, M. Igalson, and H. W. Schock, *J. Appl. Phys.* **83**, 318 (1998).
- [11] J. Lee, D. B. Needleman, W. N. Shafarman, and J. D. Cohen, *Materials Research Society Spring Proc.* **1012**, Y.12.02 (2007).
- [12] A. Klein and W. Jaegermann, *Appl. Phys. Lett.* **74**, 2283 (1999)
- [13] U. Rau, D. Braunger, R. Herberholz, H. W. Schock, J. -F. Guillemoles, L. Kronik and D. Cahen, *J. Appl. Phys.* **86**, 497 (1999).
- [14] J. Lee, J. D. Cohen and W. N. Shafarman, *Thin Solid Films* **480-481**, 336 (2005).

- [15] S. S. Hegedus, W. N. Shafarman, *Prog. Photovolt.: Res. Appl.* **12**, 155 (2004).
- [16] U. Rau, *Appl. Phys. Lett.* **74**, 111 (1999).
- [17] A. O. Pudov, J. R. Sites, M.A. Contreras, T. Nakada and H. W. Schock, *Thin Solid Films*, **480-481**, 273 (2005).
- [18] J. Lee, J. T. Heath, W. N. Shafarman, and J. D. Cohen, in *Conference Record of IEEE 4th World Conference on Photovoltaic Energy Conversion*, **1**, 360 (2006).

CHAPTER IV

METASTABILITY IN CIGS

4.1 Metastable defect creation in CIGS

For more than a decade the promise of high energy conversion efficiencies inspired photovoltaic research on electronic metastability in CIGS. Photovoltaic devices based on thin film polycrystalline CIGS absorber layers have achieved device efficiencies of more than 19% in the laboratory [1]. However, large scale manufacturing processes obtained much lower efficiencies of around 10%. According to the detailed balance limit of Shockley and Queisser there is yet room for further improvements in efficiency up to 28% [2]. The relationship between electronic properties and their role in limiting device performance still remains an open question. Since a major part of device efficiency is limited by carrier recombination, it is important to understand how the carrier recombination mechanism changes with metastable behavior in CIGS.

Despite a growing amount of research into the material properties of CIGS, metastabilities in CIGS are not well understood. Specifically, questions remain as to whether such behavior reflects poorer bulk properties of the CIGS layer, or whether it is due to interface properties at the junction. Following the summary of our research

objectives, (1) We seek to characterize and understand the nature of electronic metastability in CIGS devices both qualitatively and quantitatively. In particular we wish to understand from where metastability originates, either interface or bulk properties. (2) We seek to find the correlation between metastable changes in the carrier densities and their effects on device performance. Also, we try to identify the detailed physical mechanism underlying metastability in CIGS. We combine experimental studies of device characterization with numerical modeling using SCAPS-1D.

4.1.1 Metastable defect creation and annealing

In order to compare the metastable defect creation and annealing process, the energy barriers of the metastable defect creation and annealing need to be characterized as a function of the temperature at which the sample was light-soaked and annealed. One of the important aspects of the metastability research is that we need to keep the sample below 250 K to minimize thermal annealing of the metastable defects [3]. In order to investigate changes in the bulk CIGS under prolonged light exposure, we used laser diodes as a monochromatic light source at near-infrared wavelengths of 780 nm and 980 nm to obtain fairly uniform light-induced defect profile throughout the CIGS absorber. We tried to keep the light intensity relatively low while J - V curves were measured because too much light exposure under the forward bias condition could result in additional bias-induced metastable changes. Since metastabilities can be induced by forward and reverse bias, we were careful to choose the voltage ranges for DLCP and J - V

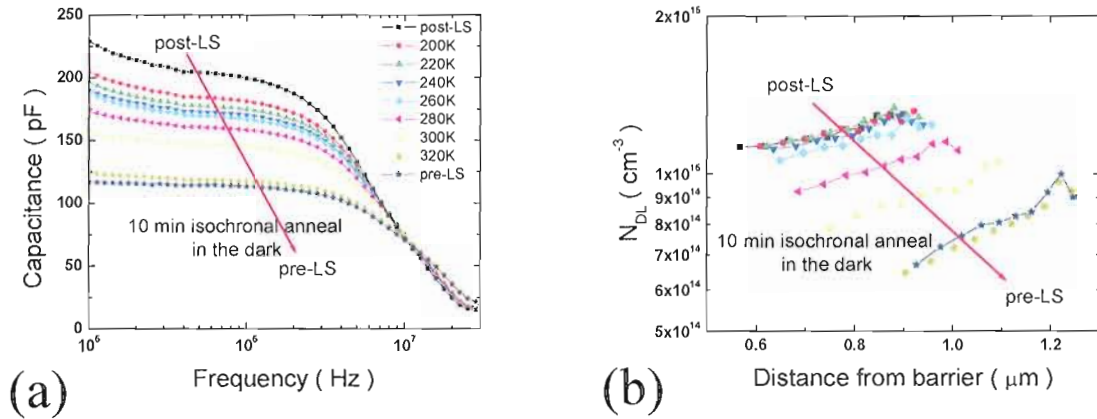


Fig. 4.1. Isochronal annealing of the light-induced changes in the high frequency capacitance and DLCP: (a) Set of 125 K capacitance spectra of CIGS #33400 for a sequence of isochronal annealing in the dark at temperature from 200 K to 320 K with 20 K step for 10 minutes. Sample was light-soaked for 3 hours at room temperature (post-LS) using monochromatic light source at 780 nm at 100 mW/cm^2 . After subsequent isochronal annealing, depletion capacitance starts to decrease down to the previous annealed state (pre-LS). (b) Corresponding set of 125 K DLCP after such isochronal anneals.

measurements. Metastable changes were also induced in the dark using a forward current injection up to values of the short circuit current under 1 sun or AM1.5 intensity. Thus we were able to compare the effect of light-induced carrier generation with the effect of electrical current injection.

Using a single 10 minute isochronal anneals at various temperatures and an isothermal anneals at 280 K after several hours of light-soaking, we obtained the energy barrier E_{bl} of the metastable defect relaxation. CIGS sample #33400 was light-soaked at 250 K for 3 hours, and then immediately cooled to 125 K in the dark. After the light-soaking, high frequency capacitance spectra at 125 K were measured for a sequence of isochronal annealing for 10 minutes in the dark at temperature ranging from 200 K to 320 K with 20 K steps.

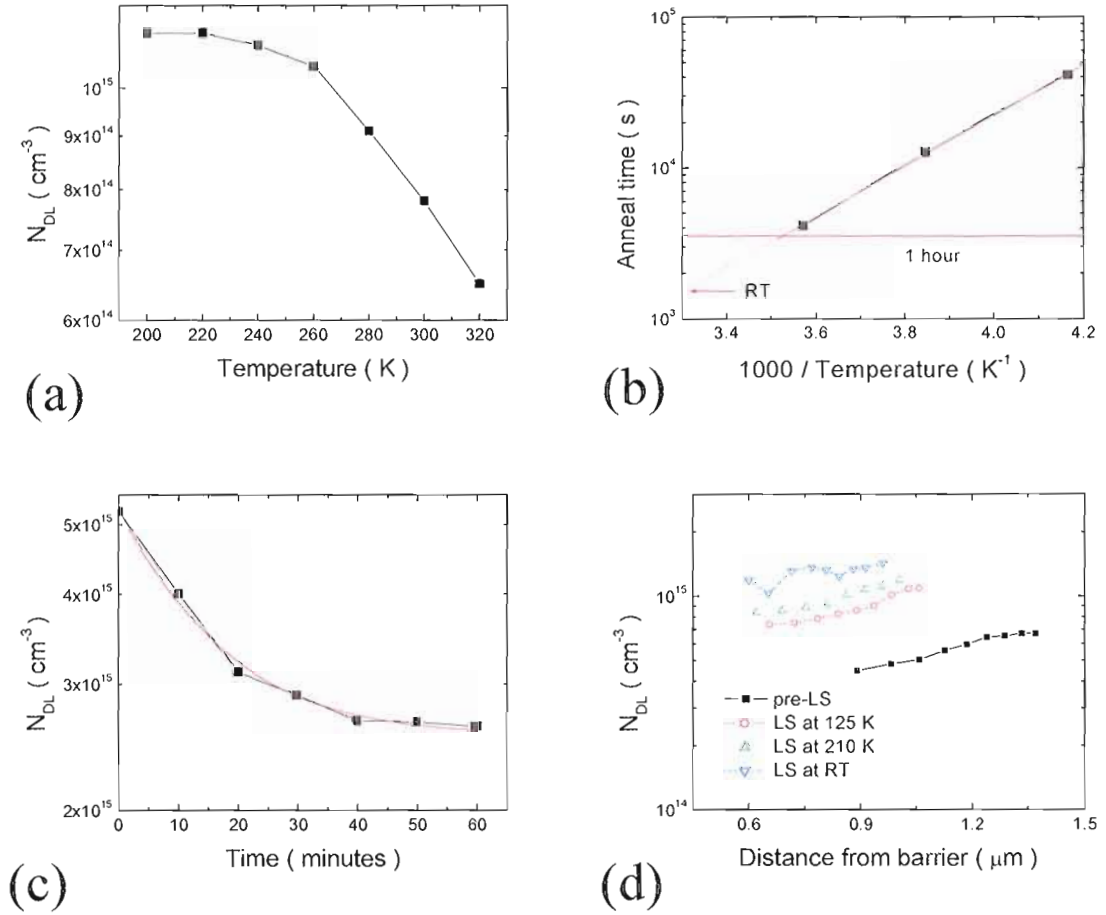


Fig. 4.2. Energy barriers for light-induced metastability in CIGS: (a) Isochronal annealing of the metastable defect as shown in Fig. 4.1(b) (b) Anneal time for metastable defects at different temperatures (c) Isothermal annealing at 300 K fitted to the exponential decay function with a time constant of 15 minutes (d) Changes in N_{DL} after 3 min light-soaking at different temperatures.

To explain the observed thermally activated annealing process with increasing annealing temperatures in Fig. 4.2(a), a thermally activated anneal rate has been assumed in Fig. 4.2(b),

$$N(T_n) = N(T_{n-1}) \exp\left(-\frac{\Delta t}{\tau_n}\right) \quad (4.1)$$

$$\tau_n = \frac{-\Delta t}{\ln \frac{N(T_n)}{N(T_{n-1})}} \quad (4.2)$$

so, the thermal barrier can be calculated from the Arrhenius equation,

$$\tau_n = \tau_0 \exp\left(\frac{E_{b1}}{kT}\right) \quad (4.3)$$

where $N(T_n)$ is the N_{DL} at certain temperature T_n , Δt is the isochronal time interval, and τ_n is the characteristic anneal time at T_n . Activation energy (E_{b1}) of 0.3 eV with a time constant of 4 ms was obtained from the dependence displayed in Fig. 4.2(b). As shown in Fig. 4.2(c) the isothermal annealing at 300 K clearly shows that annealing of the metastable states is the thermally activated process. Data were fitted to the exponential decay function of Arrhenius equation with a time constant τ_0 of 15 minutes in Fig. 4.2(c). The complementary methods of an isochronal anneal and isothermal anneal shown in Fig. 4.2(a) and Fig. 4.2(c) agree fairly well with a similar anneal time for an arbitrary annealing temperature.

Fig. 4.2(d) shows the changes in the carrier density after light-soaking for three minutes at different temperatures. We measured DLCP at low temperature of 125 K at high frequency of 1 MHz to obtain the free carrier density. We observed a faster rate of defect creation when the sample was light-soaked at a higher temperature although the energy barrier for such temperature dependence was found to be very small. In summary, energy-configurational coordinate diagram for light-induced defect creation and annealing effects with E_{b1} is shown in Fig. 4.3.

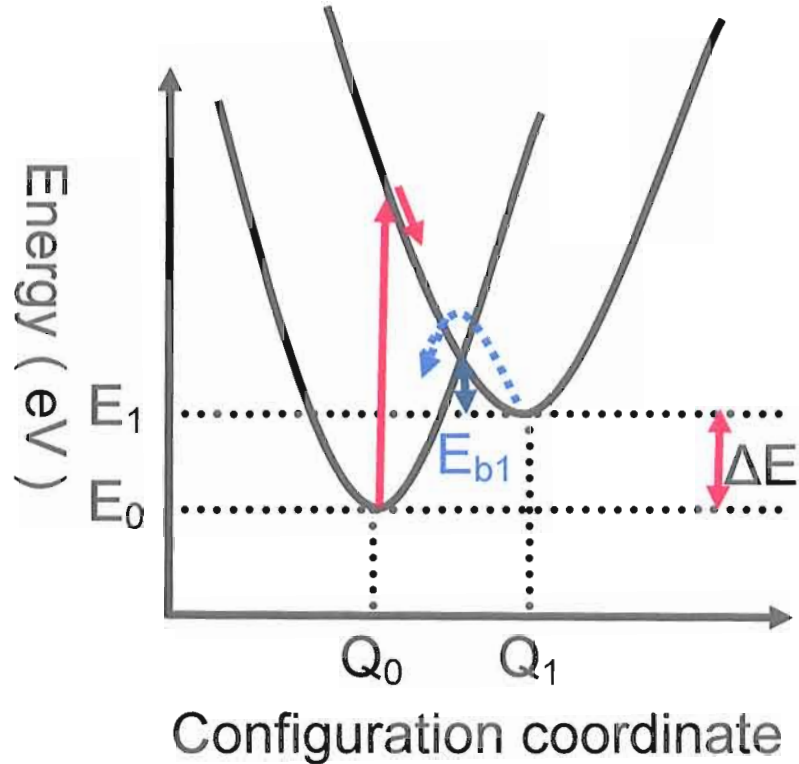


Fig. 4.3. Energy-configuration coordinate diagram for metastable defect creation (from Q_0 to Q_1) and annealing effects (from Q_1 to Q_0) in CIGS.

4.1.2 Configurational coordinate change for metastability in CIGS

The schematic diagram in Fig. 4.3 shows the configuration change for metastable defect creation (from Q_0 to Q_1) and annealing (from Q_1 to Q_0) in CIGS films [4]. Light- or voltage-induced metastability drives a configuration into the elevated energy state by ΔE and thermal annealing with an energy barrier E_{b1} brings the metastable configuration Q_1 back to the thermodynamically stable coordinate Q_0 . E_{b1} is estimated to be 0.3 eV according to the isochronal light-soaking and annealing measurements. Note that thermal annealing of metastability in CIGS at room temperature (RT) takes less than an hour (see

Fig. 4.2(c)). However, light-induced metastable defects can be created faster than their annealing rate even at RT although the concurrent annealing rate could become comparable to the creation rate at much higher temperatures.

4.1.3 Light-induced metastability

In Fig. 4.4, we monitor the changes in admittance at 300 kHz at 250 K during light exposure. Although both the capacitance and conductance phases start to increase immediately after light exposure, the conductance phase starts to decrease at high light intensity because the thermal emission rate for defects changes during the metastable defect creation. Changes in admittance persist over a long time period at temperatures below 250 K even after light turned off.

Fig 4.5 shows how admittance changes after extended hours of infrared light exposure at 250 K. At temperatures below 175 K, depletion capacitance plateau

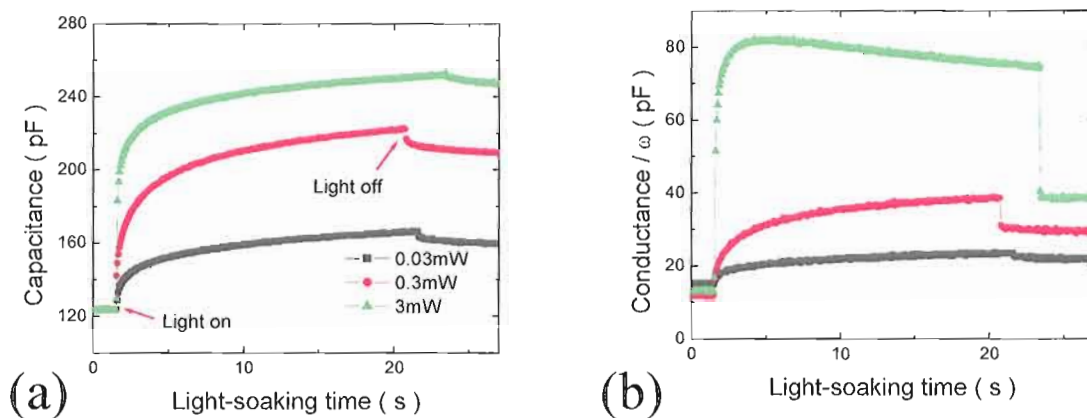


Fig. 4.4. Persistent photocapacitance (PPC) for CIGS #33400 under light-soaking at 780 nm. Capacitance (a) and conductance (b) were measured at 250 K at 300 kHz.

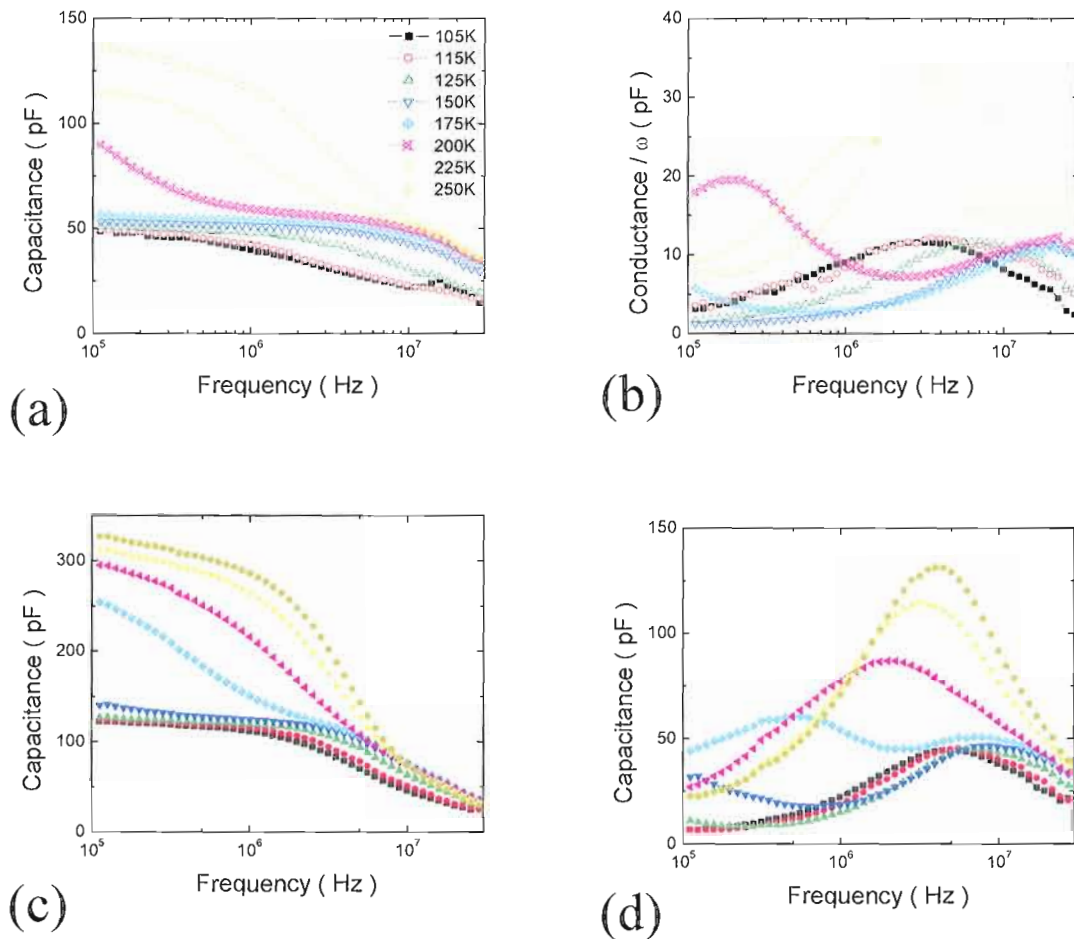


Fig. 4.5. Comparison of admittance spectra after light-soaking treatment: (a) High frequency capacitance spectra for CIGS #33400 at different temperature before 107 hours light-soaking (pre-LS) (b) Pre-LS conductance/ ω spectra that represents the real part of the admittance data shown in Fig. 4.5(a) (c) both depletion capacitance and deep states related to the capacitance step have increased after 107 hours light-soaking at 250 K (d) conductance phase has also changed as much as in Fig. 4.5(c). Shifts of conductance peaks to the higher frequencies indicate that the activation energy has been decreased after the light-soaking.

increased more than a factor of two after light-soaking, as did the trap-related capacitance step. It is interesting to notice that the conductance phase also changed not only in magnitude but also in the conductance peak position. Shifts in the conductance peak

position indicate that the activation energy has been changed after light-soaking. Note that significant annealing of the light-induced metastable change occurs only at annealing temperatures above 260 K. Also note that the dielectric relaxation time constant did not change at all after light-induced metastability since the peak frequency shifts to the lower value as depletion capacitance increases according to Eq. 3.12. Therefore conductivity in CIGS film tends to be constant during metastable defect creation, on the other hand light-induced metastability causes hole carrier mobility to decrease, as hole carrier density increases as a result.

$$\sigma = \frac{\varepsilon}{\tau_r} = pe\mu_h \quad (4.4)$$

In the high frequency and low temperature regime, a second activation step in the low temperature region, as shown in Fig. 4.5, indicates the existence of another barrier for hole transport. This step is still unassigned to any other defect activation as far as it belongs to bulk properties of CIGS [5]. To investigate this additional charge response, we attempted to correlate this temperature activated step in capacitance to the hole mobility freeze-out at low temperature due to less than 100 % defect ionization. We were able to fit admittance spectra with a reduction in hole mobility in the SCAPS simulation. However, the temperature dependence of the inferred hole mobility was unacceptably larger than the typical $T^{3/2}$ dependence. I believe it may be associated with Fermi level pinning in localized regions such as hole barriers at grain boundaries [6, 7]. Since there are more deep-trap states to pin the Fermi level after light-soaking, this could possibly account for the monotonic decrease the thermal defect activation of conduction.

However, pinning of the Fermi level at the deep-trap level tends to be contradicted by the weak temperature dependence of both the hole carrier density, determined from DLCP, and the conductivity, determined from the high frequency admittance dielectric freeze-out condition after metastable defect creation. The origin of the shallow activation step at low temperature could not be explained yet.

4.1.4 Meyer-Neldel rule behavior of the metastability in CIGS

A partial explanation for the observed behavior can be understood in terms of the Meyer-Neldel rule (MNR) [8], which explains why different activation energies associated with a particular metastable trap will have the same emission rate at the so-called “iso-kinetic” temperature as shown in Fig. 4.6(a). Based on the Arrhenius plot analysis, we obtained the activation energies of the deep defect and the capacitance step in the low temperature. We found that the activation energy of the deep defect becomes smaller with increased light-soaking treatments and approaches the shallow activation energy value after prolonged light-soaking, following the MNR line, as shown in Fig. 4.6(b).

A number of explanations physically justifying the MNR in a-Si:H have been proposed; however there is not a widely accepted microscopic model of MNR for CIGS [10, 11]. Yelon, Movaghar and Branz suggested that the origin of MNR might be explained as arising from phonon-assisted electron hopping in a-Si:H [12]. We found

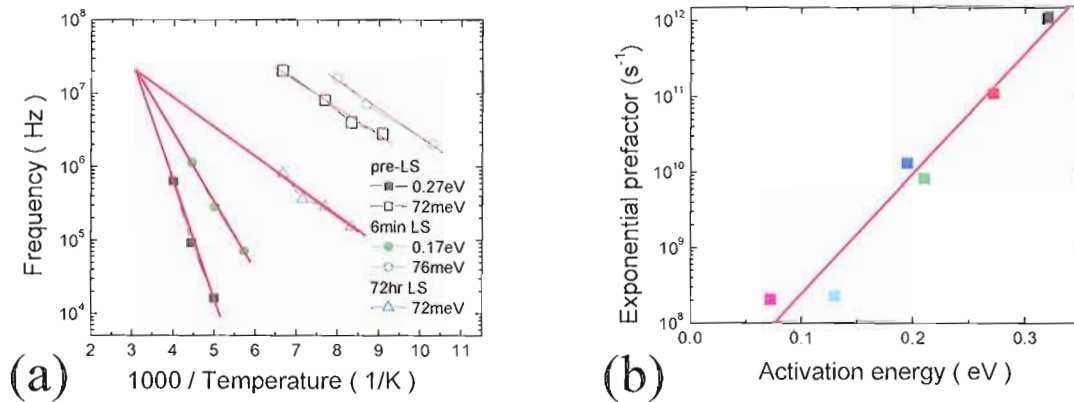


Fig. 4.6. Meyer-Neldel rule (MNR) behavior of metastability in CIGS. (a) Arrhenius plot of deep and shallow defect activation for annealed state (pre-LS, solid and hollow rectangles), after 6 minutes light-soaking (6 min LS, solid and hollow circles), and after 72 hours light-soaking treatments (hollow triangles) (b) MNR plots of different metastable states after light-soaking treatments.

two different activation energies in the thermal admittance spectra in Fig. 4.6 and that only the activation energy of the deep trap states decreased with the light-soaking approaching that of shallow level. This suggests that both thermal activation energies actually might originate from the same defect states and only one actual energy poison for deep trap states could be related to that defect. However, whether this metastability-related MNR behavior is based on two different competing processes or is just a variation in the single defect activation is still unknown. This experimental finding seems to agree with the previously observed continuous shift of the activation energy of the air annealing at 200 °C, although our deep trap states response in bulk CIGS is at odds with the interpretation based upon a continuous distribution of sub-bandgap states near at the interface [13, 14].

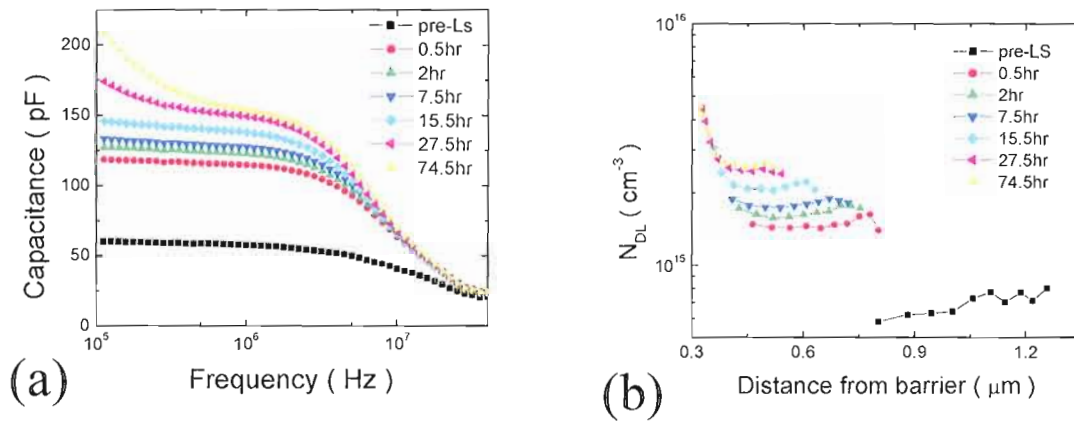


Fig. 4.7. High frequency admittance spectra and 1 MHz DLCP profiles at 125 K for CIGS #33400 before (pre-LS) and after light-soaking at 250 K for increasing exposure times.

4.1.5 Universal 1:1 ratio in metastable defects creation

We next determined a set of high frequency admittance spectra together with a corresponding DLCP profiles obtained at 125 K following light exposures at 250 K for increasing exposure times. After such light exposures, the depletion capacitance and DLCP profiles exhibited a monotonously increasing metastability feature as shown in Fig. 4.7. Significant metastable effects already occurred in the first few minutes and observed light-induced metastable changes continued up to nearly 100 hours of exposure. After about 20 hour exposure, a significant deep trap density starts to cause a curvature of the capacitance spectra in the low frequency region even at low measurement temperature of 125K. Furthermore, the DLCP profiles also start to bend upward near the interface region, indicating inhomogeneous metastable changes near the junction barrier.

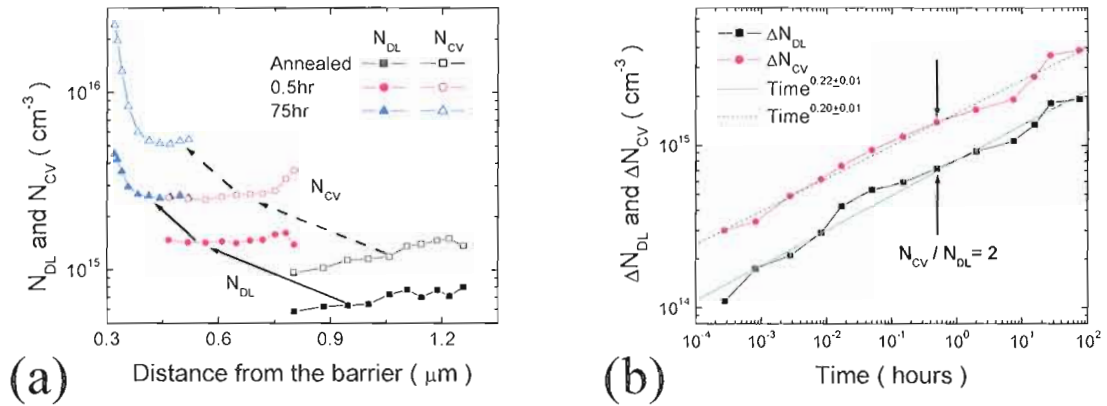


Fig. 4.8. Light-induced changes in DLCP and CV density: (a) Comparison between DLCP (solid symbols) and CV profiles (open symbols) (b) Set of DLCP and CV densities after consecutive light-soaking at 250 K by a 780 nm near-infrared light. Values of CV are roughly a factor of 2 larger than corresponding DLCP throughout exposure time.

Using DLCP and CV characterization methods, we observed changes in the free carrier density p and in the deep defect density N_T after their light-soaking treatments. Since DLCP is insensitive to the response from the deep defect states or interface states at high frequency and low temperature, it directly provides the free carrier response p , while the CV profile yields the sum: $p + N_T$. A set of DLCP and CV profiles for a series of metastable states are compared in Fig. 4.8(a). The apparent factor of 2 resulting when the ratio N_{CV}/N_{DL} is taken implies that changes in p and N_T are roughly equal in magnitude. Note that the rate of increase in N_{CV} near the interface region is much faster than that of N_{DL} after a 75 hour light-soaking, perhaps suggesting additional metastable changes near the barrier interface.

One of the important aspects of light-induced defect creation is that there is no hint of saturation in metastable defect creation (see Fig 4.8(b)) up to times where the considerable increase in the free carrier density shrank the depletion width.

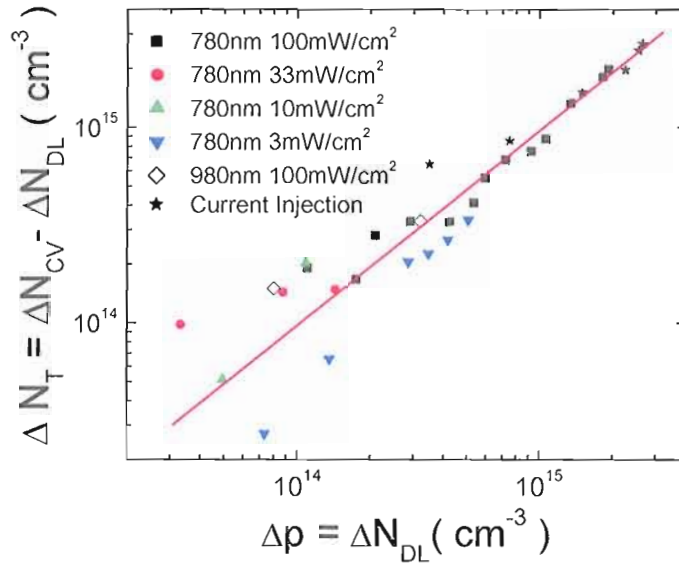


Fig. 4.9. Universal 1:1 ratio in metastable defect creation regardless of the method used to create the metastable changes. Light-soaking over a wide range of light intensities at different wavelengths, and even forward bias current injection induced the same rate of increases in the p and N_T .

Another striking result of metastability in CIGS is the 1:1 ratio in the changes in p and N_T . The universal 1:1 relationship between the increases in p and N_T is clearly shown in Fig. 4.9 where $p = N_{DL}$ and $N_T = N_{CV} - N_{DL}$ when compared at high frequency (1 MHz) and low temperature (125K). The 1:1 ratio relationship between changes in p and N_T was also found to be independent of the method used to create metastability, either by light exposure at different intensities and wavelengths, or by forward current injection at short circuit current equivalent of 32.4 mA/cm^2 . This relationship suggests that carrier recombination is responsible for the defect creation rather than any direct optical transition. Universal 1:1 ratio even from the forward current *electron* injection ensures that the capture of electron carrier into the deep electronic defect states initiates the

metastable creation of deep acceptor defect and free hole carrier density in 1:1 ratio, which seems to be consistent with the Lany-Zunger's theoretical model of $V_{Se}-V_{Cu}$ defect complex.

4.1.6 Lany-Zunger's theoretical model

It is now well understood that this metastability is a carrier recombination induced process, meaning that a common agent creates metastable defects both for forward current injection and for light exposure [15]. This hypothesis may not be surprising since these treatments show the same characteristic degradation patterns such as persistent photoconductivity (PPC) through the conversion of the recombination center as shown in Fig. 4.4.

Several models have been proposed to explain this metastable effect in CIGS: changes in charge states in vacancy complex of $(V_{Se}-V_{Cu})$ and configurational coordinate conversion of In (or Ga) interstitial ordered defect pairs $(In_{Cu}-2V_{Cu})$ into DX centers [16, 17]. We find that our experimental results are generally consistent with the vacancy complex model $(V_{Se}-V_{Cu})$. This model implies that the different metastable states observed in CIGS arise from the different charge states of the same defect. The vacancy complex $(V_{Se}-V_{Cu})$ or interstitial ordered defect pairs $(In_{Cu}-2V_{Cu})$ share interesting concepts: the capture (or release) of two electrons into each defect complex induces a configuration change in the vacancy complex which results in defect creation (or annealing) [17]. Both models predict PPC through resulting charge state conversion

following the two electron capture event [18]. The important new feature relative to the isolated point defect is that metastability in these defect complexes accompanies configurational change by capturing two electrons. However, it is not clear how efficient it is to maintain the same lattice formation with a double carriers capture in one defect complex.

We prefer the $(V_{Se}-V_{Cu})$ vacancy complex model because it accounts in a straightforward way for the experimentally observed 1:1 ratio between the free carrier density p and the metastable hole trap density N_T . That is, after the positively charged defect complex $(V_{Se}-V_{Cu})^+$ captures two electrons to becomes the metastable $(V_{Se}-V_{Cu})^-$ center, two holes are added to the valence band. This metastable state of the negatively charged defect complex $(V_{Se}-V_{Cu})^-$ can then attract and bind a hole, and resulting in the observed 1:1 ratio between the increase in a neutral acceptor and one free hole. Metastable hole trap states related with $(V_{Se}-V_{Cu})^-$ in the acceptor-configuration used to be attributed to the important recombination center, thus restricting solar cell device performance [18]. However, our recent studies argue that this acceptor defect is not the only important recombination center [19]. Instead, we believe the donor state $(V_{Se}-V_{Cu})^+$ is also important as a recombination center. Indeed, since the metastable acceptor states is relatively shallow throughout the wide band gap CIGS alloy system, the donor state is likely the more efficient recombination center if its energy position gets deeper into the mid-gap for the wide band gap CIGS alloy.

4.2 Metastable defect creation kinetics

4.2.1 Sub-linear time and intensity dependence of defect creation kinetics in CIGS

As shown in Fig. 4.10, metastable defect creation after light soaking at 780nm appears to follow sub-linear power law dependence with respect to the light-soaking time, $t^{0.22\pm0.03}$, and also the light intensity $I^{0.53\pm0.06}$. Changes in metastable defect densities were estimated by subtracting the initial value of DLCP density of $7 \times 10^{14} \text{ cm}^{-3}$ from those at later times. We found that intensity power law exponent was roughly twice bigger than that of the time dependence. Accounting for different rate dependence of defect creation kinetics on time and intensity is the main topic for the next section. Saturation at high light intensity was observed in Fig. 4.10(b) although whether it could be used as a hint of limited precursor sites for the metastable defect creation is doubtful.

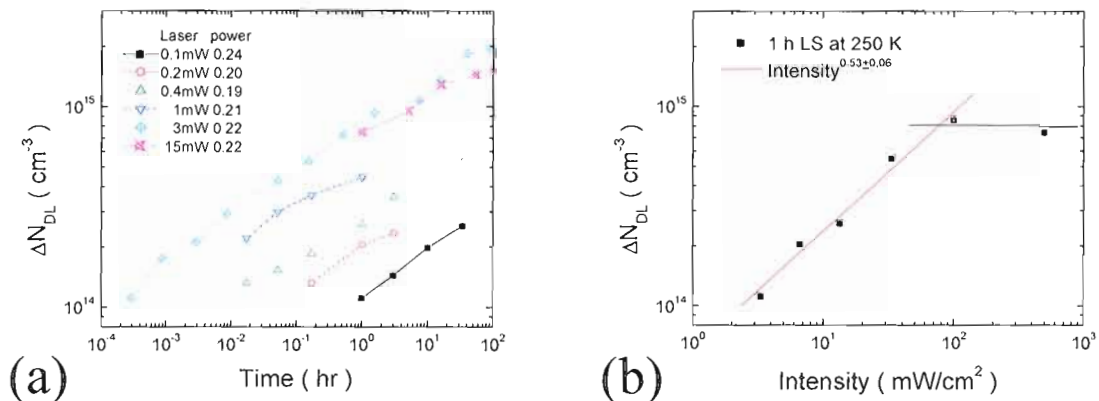


Fig. 4.10. Time and intensity dependence of metastable defect creation after light-soaking at 780 nm at 250 K. (a) $\log N_{DL}$ vs $\log(\text{Time})$ follows a power law with an exponent of 0.22 ± 0.03 (b) intensity dependence of metastable defect creation after 1 hour light-soaking. $\text{Intensity}^{0.53\pm0.06}$ dependence is about twice faster than the time dependence.

4.2.2 Rate equation analysis

The sub-linear time and intensity dependence shown in Fig. 4.10 provides a further test of the metastability mechanism. To evaluate the defect creation kinetics of the light-induced metastability in CIGS, we first considered the simplest rate equation that might describe the metastable defect creation as a result of a one-electron capture as an initiating event. Because the 1:1 ratio between p and N_T indicates that the capture of minority electron carriers into the pre-cursor sites creates the deep traps and excess hole carriers, it can be written as

$$\frac{dN_T}{dt} = C_1 n (N_p - N_T) \quad (4.3)$$

where C_1 is the rate equation coefficient, n is electron density in the conduction band, and N_p is the number of precursor sites that can be converted into N_T defects as a result of electron capture. Note that the metastable defect creation kinetics is self-limited since the creation of the new metastable defect is inhibited by the already created metastable defects. Therefore the metastable defect creation rate is inversely proportional to its own metastable density.

The quasi-steady state electro density is determined when the generation rate G (which is proportional to light intensity), is equal to the recombination rate R , if we assume a bimolecular recombination process through recombination sites of N_R :

$$G = R \propto N_R np \quad \text{or} \quad n \propto \frac{G}{pN_R} \quad (4.4)$$

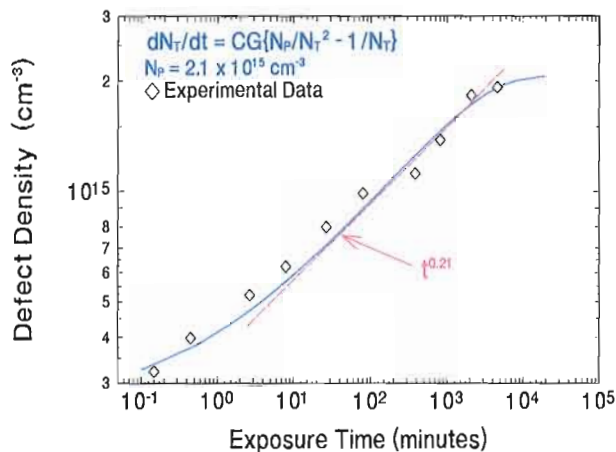


Fig. 4.11. Saturation of the metastable defect creation assuming a limited defect density of precursor sites. Simulation results (line) are used to fit the experimental data (symbols) and mid-range fitting (dotted line) shows the time dependence of $t^{0.21}$ close to the experimental result of $t^{0.22 \pm 0.03}$.

As discussed above, p increases in direct proportion to N_T ($p = N_T$) while the overall carrier density in the undepleted part of p-type CIGS absorber does not change much from its dark value under light exposure. Moreover, if we assume that the dominant recombination center N_R is the same metastable defect N_T ($N_R = N_T$) then we have $n \propto G/N_T^2$ and inserting this into Eq. 4.3, we obtain

$$\frac{dN_T}{dt} = C'G \left[\frac{N_p}{N_T^2} - \frac{1}{N_T} \right] \quad (4.5)$$

If the density of precursor sites is always larger than metastable N_T , then integrating Eq. 4.5 leads to the $t^{1/3}$ power law, which is typical for the bimolecular recombination. Although it is a much faster rate than experimentally observed $t^{0.22 \pm 0.03}$, we can get a reasonable fit to experimental data if we assume that an initial value of N_p is close to the final N_T value of $2.1 \times 10^{15} \text{ cm}^{-3}$ as shown in Fig. 4.11.

4.2.3 Two electron capture model

However, the intensity dependence is at odds with the rate equation dependence of the previous section because Eq. 4.5 fails to account for the twice larger power law exponent in $I^{0.53 \pm 0.06}$. Instead, it predicts the same rate of time and intensity dependence without respect to the details of any other quantity inside the bracket in Eq. 4.5. Therefore, we consider a different approach in the initial rate equation, namely a two-electron capture model:

$$\frac{dN_T}{dt} = C_2 n^2 (N_P - N_T) \quad (4.6)$$

That is, we assume that it is the capture of two electrons into the precursor site that initiates the metastable defect creation process [3]. Moreover, we believe this two electron capture model would be more consistent with the Lany-Zunger model as discussed in the previous section.

If we assume the bimolecular recombination process, an electron density n is

$$n \propto \frac{G}{N_T N_R} \quad (4.7)$$

since $p = N_T$ according to the observed 1:1 ratio increase during metastable defect creation. Inserting this into Eq. 4.6 give

$$\frac{dN_T}{dt} = C''' G^2 \left[\frac{N_P / N_R^2}{N_T^2} - \frac{1 / N_R^2}{N_T} \right] \quad (4.8)$$

Now we can account for the approximately 1:2 relationship between the time and intensity dependence in power law exponents of the defect creation kinetics. Solving Eq. 4.8 leads to

$$N_T \propto (G^2 t)^\alpha \quad (4.9)$$

where α lies in the range $0.2 \leq \alpha \leq 0.33$ depending on how much the metastable trap states contribute to the recombination centers. If N_R is the same metastable defect N_T ($N_R = N_T$), then α should lie close to 0.2, while α would be 0.33 if $N_R \neq N_T$ is used. That is, if N_T is the dominant recombination center then α should strongly sub-linear, while α would be typical 1/3 if other processes dominate recombination. The exponent α plays a weighting factor which depends on what is the dominant recombination center. A reasonable fit can be obtained for α lying near 0.25 for the obtained experimental kinetics data.

Furthermore, we found another compelling constraint on this rate equation analysis for SCAPS modeling. The most successful mechanism we have found for explaining the observed metastable effects is a conversion of a donor defect into a bulk acceptor. We considered the compensation model in which both donor and acceptor defect play the role of recombination centers in the bulk CIGS. Before describing the details of the experimental results based on the compensated donor-acceptor conversion model analysis in the following chapter, we will present the rate equation analysis of the metastability kinetics based on this model.

The constancy of the sum of donor and acceptor defects stays constant throughout the metastable conversion process suggests that total recombination centers $N_R = N_p + N_T$ should remain constant also while light-induced metastability occurs. Since Eq. 4.8 has a

same functional form as in Eq. 4.5, integrating Eq. 4.8 with this constraint readily provides the slightly less than 1/3 sub-linear power law dependence as displaced in Fig. 4.11. Furthermore, 1:2 relationship between the time and intensity dependence in exponents of the defect creation equation in Eq. 4.8 is guaranteed for the compensated donor-acceptor conversion model in Eq. 4.11.

$$\frac{dN_T}{dt} = C_2 \left(\frac{G}{N_T N_R} \right)^2 (N_R - 2N_T) \quad (4.10)$$

$$\frac{dN_T}{dt} \propto C_2 G^2 \left[\frac{1/N_R}{N_T^2} - \frac{2/N_R^2}{N_T} \right] \quad (4.11)$$

As a result, time and intensity dependence for the compensated donor-acceptor conversion model ($N_R = N_p + N_T$) also agrees with a proposed rate equation model in which the capture of two electrons into the pre-cursor sites (N_p) initiates the metastable creation of a deep trap (N_T) and excess hole carrier. Furthermore, charge balance between the negatively charged vacancy complex and two free holes can provide the 1:1 ratio relationship between the metastable changes in the free hole carriers and deep trap density as predicted by the proposed compensated donor-acceptor conversion model.

Notes

- [1] K. Ramanathan, M. A. Contreras, C. L. Perkins, S. Asher, F. S. Hasoon, J. Keane, D. Young, M. Romero, W. Metzger, R. Noufi, J. Ward, and A. Duda, *Prog. Photovolt.: Res. Appl.* **11**, 225 (2003).
- [2] Shockley and Queisser, *J. Appl. Phys.* **32**, 510 (1961).
- [3] J. Lee, J. T. Heath, W. N. Shafarman, and J. D. Cohen, in *Materials Research Society Proc.* **865**, F12.4.1 (2005).
- [4] D. Redfield and R. H. Bube, *Photoinduced Defects in Semiconductors*, (Cambridge University Press, 1996).
- [5] J. Kneisel, K. Siemer, I. Luck, and D. Braunig, *J. Appl. Phys.* **88**, 5474 (2000).
- [6] M. Gloeckler, J. R. Sites, and W. K. Metzger, *J. Appl. Phys.* **98**, 113704 (2005).
- [7] M. Gloeckler and W. K. Metzger, *J. Appl. Phys.* **98**, 063701 (2005).
- [8] W. Meyer and H. Neldel, *Z. Tech. Phys.* **12**, 588 (1937).
- [9] R.S Crandall, in *Materials Research Society Proc.* **763**, B2.5.1 (2003).
- [10] M. Stutzmann, W. B. Jackson, and C. C. Tsai, *Phys. Rev. B* **32**, 23 (1985).
- [11] M. Stutzmann, W. B. Jackson, and C. C. Tsai, *Phys. Rev. B* **34**, 63 (1986).
- [12] A. Yelon, B. Movaghar, and H. M. Branz, *Phys. Rev. B* **46**, 12244 (1992).
- [13] R. Herberholz, M. Igalson, and H. W. Schock, *J. Appl. Phys.* **83**, 318 (1998).
- [14] U. Rau, D. Braunger, R. Herberholz, H. W. Schock, J.-F. Guillemoles, L. Kronik, and D. Cahen, *J. Appl. Phys.* **86**, 497 (1999).
- [15] M. Igalson and H. W. Schock, *J. Appl. Phys.* **80**, 5765 (1996).
- [16] S. Lany and A. Zunger, *Phys. Rev., B* **72**, 035215. (2005).

- [17] S. Lany and A. Zunger, *J. Appl. Phys.* **100**, 113725 (2006).
- [18] S. Lany and A. Zunger, *Phys. Rev. Lett.* **100**, 016401 (2008).
- [19] J. Lee, J. T. Heath, W. N. Shafarman, and J. D. Cohen, in *Conference Record of IEEE 4th World Conference on Photovoltaic Energy Conversion*, **1**, 360 (2006).
- [20] M. Gloeckler, PhD thesis (Colorado State University, Fort Collins, 2005).

CHAPTER V

MODELING OF METASTABILITY IN CIGS

USING THE COMPENSATED DONOR-ACCEPTOR CONVERSION MODEL

5.1 Metastability in the wide bandgap CIGS

Wide bandgap chalcopyrite solar cells, including CIGS devices with higher Ga/(In+Ga) content, have failed to achieve the expected levels of energy conversion efficiency, primarily due to the open-circuit voltage V_{OC} deficits at higher bandgap energy. [1] There are significant deviations of V_{OC} from the values expected purely from the bandgap E_g increase in wide bandgap solar cells as shown in Fig. 5.1(a). Although V_{OC} up to 1.3 eV agree fairly well with the expected V_{OC} increase for the wide bandgap CIGS, it starts to saturate even with more Ga addition. Typically energy conversion efficiency actually drops rapidly with more than 30 % Ga addition ($E_g \sim 1.2$ eV) as shown in Fig. 5.1(b). Previously, we have studied the effect of the Ga addition on sub-bandgap defect states and found that the admittance response did not vary much and that their deep acceptor densities were within a reasonable variation range regardless of Ga content.

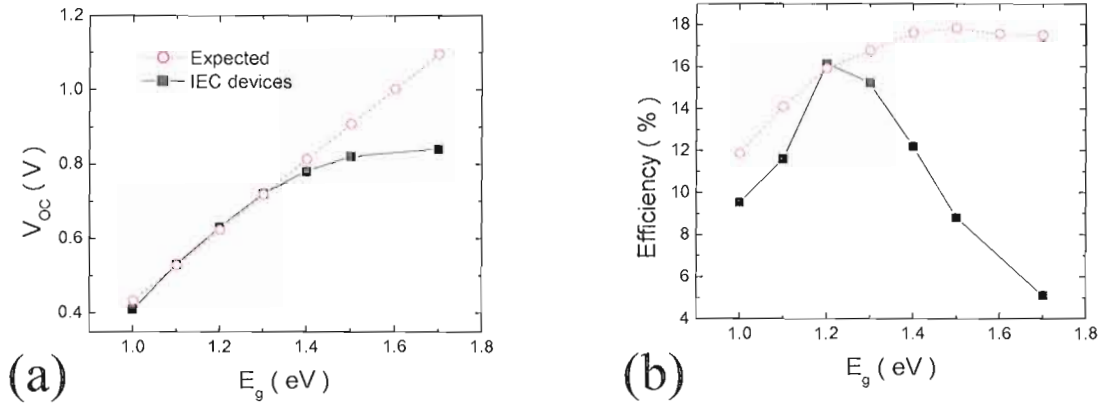


Fig. 5.1 Comparison between the expected CIGS device parameters obtained from SCAPS modeling and the actual experimental results from IEC devices in Table 2.1. (a) V_{OC} deviation from the expected values for wide bandgap CIGS (b) Efficiency drops rapidly for $E_g > 1.3$ eV.

None of the above experimental results is consistent with the ideal modeling case because there is no significant deep defect state other than acceptor state E_A at 0.3 eV above the valence band preventing V_{OC} from increasing as the bandgap increases. Certainly there are many other possible candidates including (1) the optically determined defect located 0.8 eV above the valence band edge, if it acts as a strong recombination center (2) recombination at the interfaces, possibly grain-boundary related defects within the space charge region (SCR), and (3) recombination of carriers via trapping in the bandtails. Our TPC studies found that defect states energy level at 0.8 eV above valence band did not change systematically as the gap was widened with gallium alloying in CIGS devices [2]. As this 0.8 eV defect state approaches further into the mid-gap in the high Ga content CIGS, it would become a more efficient recombination center for the wide bandgap CIGS devices.

However, it is not certain what makes a particular electronic trap behave as a stronger recombination center. To the extent that these defect states are electronically active, they can affect the solar cells performance by acting as recombination centers, modifying the Fermi energy or disrupting their spatial distribution. Recombination is often classified in the literature as sources either interface-related or bulk-related. For example, earlier works discussed the effect of a conduction band offset (CBO) at CdS/CIGS hetero-junction interface [3-7]. Since it is difficult to modify the interface properties without affecting other device parameters, numerical modeling involving the CBO, ordered defect complex (ODC), charged deep acceptor states (N_A), and compensated donor acceptor pair (DAP) have been performed. [7-11]. We focus on light-induced metastability to test the bulk nature of recombination mechanism in CIGS solar cells.

5.1.1 Correlation between electronic defects and photovoltaic device performance

A number of defect states that could be responsible for limiting device performance have been observed within the bandgap of polycrystalline CIGS thin films [12-14]. However, it was difficult to link specific defect states or other electronic properties of the film with the solar cell device performance [15]. In this study we have attempted to correlate the electric characteristics of the CIGS devices with electronic defect properties of the bulk absorber layer using our current understanding of metastability in CIGS solar cells. We performed admittance spectroscopy, DLCP, and

TPC, directly on the completed device structure, to provide the hole carrier mobility and carrier densities of the electronic defect states in the CIGS layer. The hole trap density was manipulated in a metastable fashion (light-soaking and thermal annealing) to isolate and thus identify its specific effects on device performance. At the same time, using near-infrared plus UV illumination, we performed J - V measurements to determine device parameters.

We have shown that under infrared illumination or forward bias conditions the density of the sub-bandgap defect located approximately 0.3 eV from the valence band edge and the density of majority carriers could both be increased by a substantial factor and in a 1:1 ratio [16]. Thus, the increase in the hole trap density could be linked to the reductions in the device performance, attributable to the apparently increased level of recombination after light-induced metastability in CIGS.

5.1.2 Metastable changes in J - V curves

Detailed experiments were carried out to compare the changes in the electronic defect states with the changes in the device performance. We measured J - V curve characteristics under near-infrared illumination at 780 nm at 50 mW/cm² after a series of light-soaking treatments. As shown in Fig. 5.2 observations of systematic changes in J - V curves reveals that V_{OC} did not change appreciably while the free carrier and deep acceptor defect densities increased by a more than factor of 5. Also we were able to

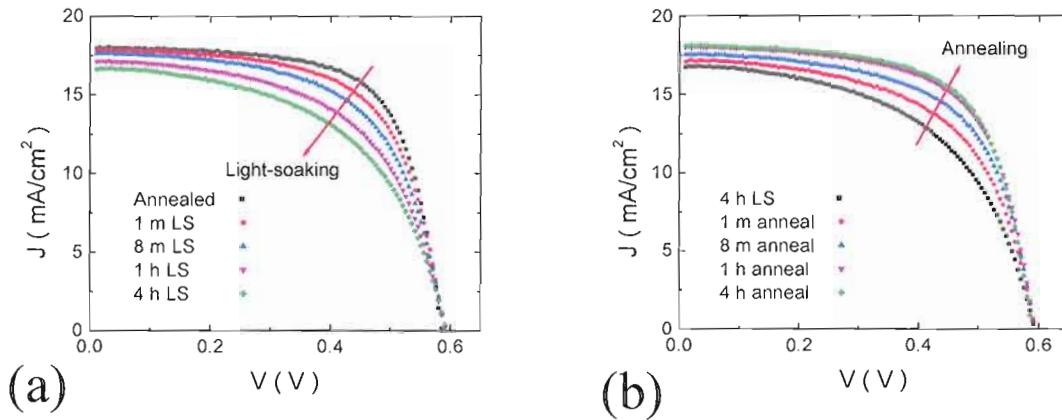


Figure 5.2. Metastable changes in J - V curves for CIGS #33713: (a) Light-soaking: experimental J - V curves at 300 K using 780 nm monochromatic near-infrared light source at an intensity of 50 mW/cm² (b) Annealing: metastable changes were reversed after device was left several hours in the dark at 300 K.

reverse these metastable changes after a sample was left in the dark at 300 K for several hours. These changes definitely occurred in the bulk region of the CIGS absorber. Although our measurements gave no indication of interface states, additional changes in the near interface or even at CdS buffer layer by light-soaking treatment cannot be completely ruled out.

In analyzing the J - V curves, we used the ideal diode equation to check variations in the series and shunt resistance as the electronic device properties were degraded. The J - V curves obtained were fitted according to the Eq. 5.1 with J_0 , A , and J_{SC} as variables. Fig. 5.3 shows the non-linear square fitting (NLSF) of the obtained J - V curves after a series of light-soaking treatments. We found that the simple ideal diode equation was sufficient to fit the various metastable states to the ideal equation with the addition of the two variables J_{SC} and A .

$$J = J_0 \left[\exp\left(\frac{qV}{AkT}\right) - 1 \right] - J_{sc} \quad (5.1)$$

We obtained excellent NLSF fits on a series of metastable J - V curves were obtained even with no additional dependence of the series resistance r and shunt resistance R , therefore neither r nor R appear to play any role in limiting the device performance. Their effects on the ideal diode equation were negligible at least for the high efficiency CIGS solar cells. More attempts were made to check whether variations in R and r were occurring with the light-induced metastability, using typical analysis techniques were used to characterize the R and r as shown Fig. 5.4. R is dV/dJ near J_{sc} and did not vary much with the light-soaking.

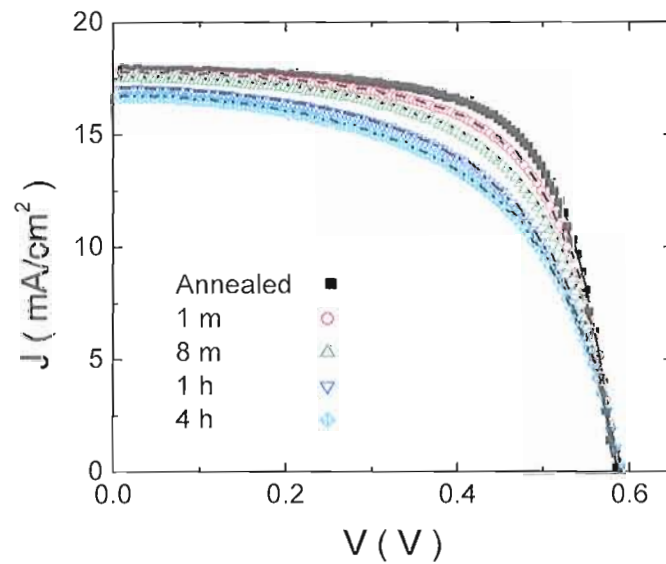


Fig. 5.3. Non-linear square fitting (NLSF) of the experimentally obtained J - V curves to the ideal diode equation after light-soaking treatments. Data (symbols) and NLSF fit (lines).

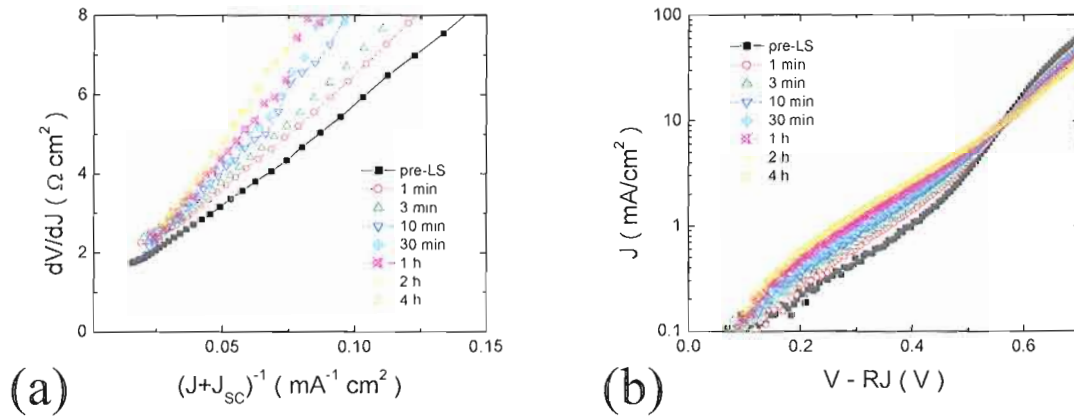


Fig. 5.4. Typical analysis of un-ideal J - V curve parameters: (a) Changes in shunt resistance and diode ideality factors (b) semi-logarithmic J - V curves after light-soaking treatments.

Slopes in Fig. 5.4(a) are equal to AkT/q and the intercept of the linear fit gives r as was already shown in Fig. 3.10(c). Both R and r were difficult to determine using the dV/dJ vs $(J+J_{sc})^{-1}$ (derivative resistance plot) method although A showed increasing slopes with the light-soaking treatments. Adjusted J - V curves also showed a clear tendency of increasing A with longer light soaking treatments in Fig. 5.4(b). Note that the humps in the J - V curves between 0.2 and 0.4 V are commonly related to the amount of integrated recombination loss and seem to be correlated with an increased degree of recombination after light-soaking treatments. Indeed, the increase in their ideality factors A seems to account well for the significant changes in the bulk recombination after light-soaking. Thus, the metastable state of non-ideal diode behavior could be gradually expressed by an ideality factor A .

Although these results are consistent with the bulk nature of recombination in CIGS layer, it is still puzzling how to interpret $A > 2$ with longer light-soaking treatments

because $A=2$ already means that most of the recombination is occurring within the space-charge region (SCR) of the bulk CIGS layer [16, 17]. Further changes in A above a value of 2 might indicate that there might be more than SCR recombination to account for metastable changes in $J-V$ curves [18]. A higher level of tunneling-enhanced recombination at the interface could be responsible for such complex recombination because the comparison of CV and DLCP suggested a somewhat higher degree of interface defect state localized near the barrier interface after long hours of light-soaking as shown in Fig. 4.7(a). Since we have characterized diode ideality factors in many ways, we summarized them in Fig. 5.5.

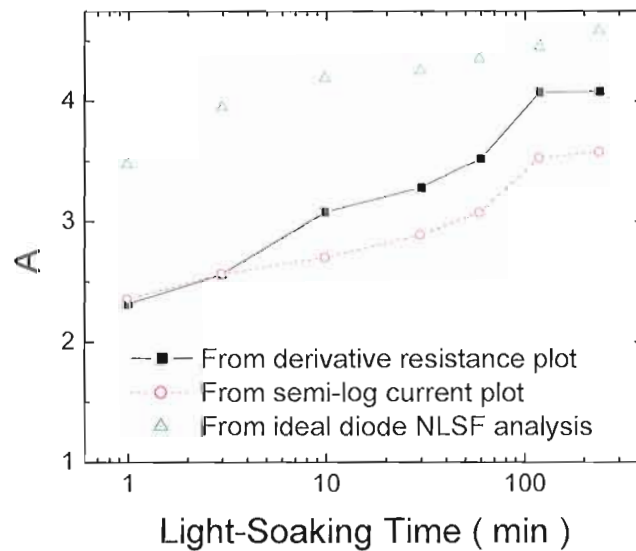


Fig. 5.5. Variation of the ideality factors A with the light-soaking treatments. Diode ideality factor A were characterized by various $J-V$ characterization methods as described in above section.

5.1.3 SCAPS modeling of metastability

Detailed numerical modeling was carried out to simulate the changes in the J - V curves along with the changes in the electronic defect states. Baseline SCAPS parameters for CIGS are listed in Table 5.1. Most input parameters refer to the earlier work of Gloeckler et. al. with a couple changes in accord with our experimental data [27]. Note that our baseline model does not include CdS/CIGS band offsets at the interface and both the 0.3 eV acceptor and 0.6 eV (or above) donor have single discrete defect distributions with a fairly large capture cross-section, σ_h or σ_e . Most adjustments in the baseline parameter sets are generally consistent with admittance spectroscopy and DLCP results while defect properties in the CIGS and other layer are used to fit the data.

As was shown in the J - V curves for a series of metastable states after light-soaking in Fig. 5.2(a), we observed decreases in J_{SC} and FF , but no significant change in V_{OC} . To determine the origin of the metastable degradation more precisely as well as its relationship to the bulk nature of the deep acceptor defect states as the dominant recombination center, we attempted to model these metastability effects using only the deep acceptor as a recombination center in Fig. 5.6(a).

We assumed the observed metastable deep acceptor defect (located at 0.3 eV above the valence band) as the only dominant recombination center, as shown in Fig. 5.6. Based on the experimental data, the free carrier density (shallow acceptor density) and the deep acceptor density were incrementally increased in a 1:1 ratio. We could not

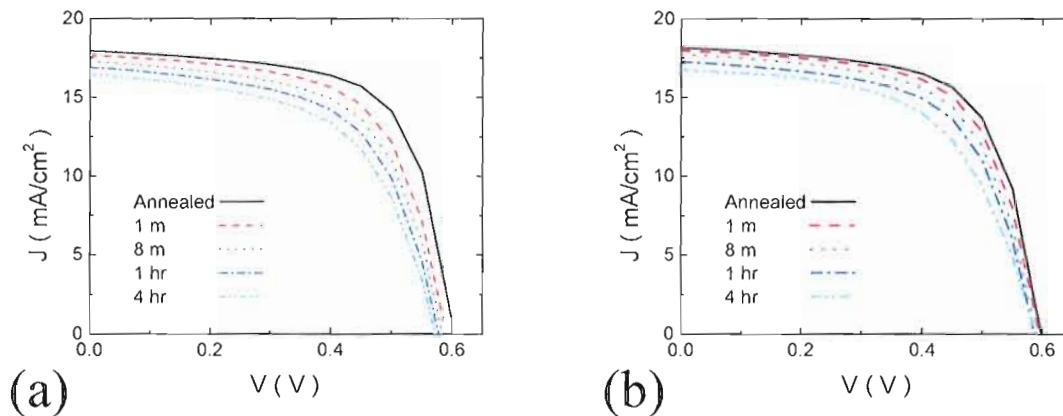


Fig. 5.6. SCAPS simulation with the deep acceptor as the dominant recombination center: (a) matching the changes in J_{SC} and FF in the experimental J - V curves well except that V_{OC} does not remain constant. (b) SCAPS simulation assuming varying electron capture cross-sections σ_e for different light-soaking states. σ_e was extremely large to keep V_{OC} constant.

match the experimental J - V curves with the deep acceptor states as the only recombination center. Although the decrease in J_{SC} and FF are well correlated with the narrowing of depletion width due to the increase of the free carrier density, V_{OC} did not remain constant unless we assume an extremely large capture cross-section σ_e ($\sim 10^{-12}$ cm²) and decreased its value monotonically as a function of light-soaking time. Since V_{OC} is mostly determined by the recombination rate, the recombination rate would be required to remain nearly constant to keep V_{OC} constant. Thus, in order to keep the recombination rate constant as the deep acceptor (hole trap) defect increases, σ_e would then have to be changed from 10^{-12} cm² to 2×10^{-13} cm². Such a change in σ_e is unphysical, as is its magnitude for the deep acceptor state near the valence band.

The failure of SCAPS modeling with the deep acceptor state as the dominant

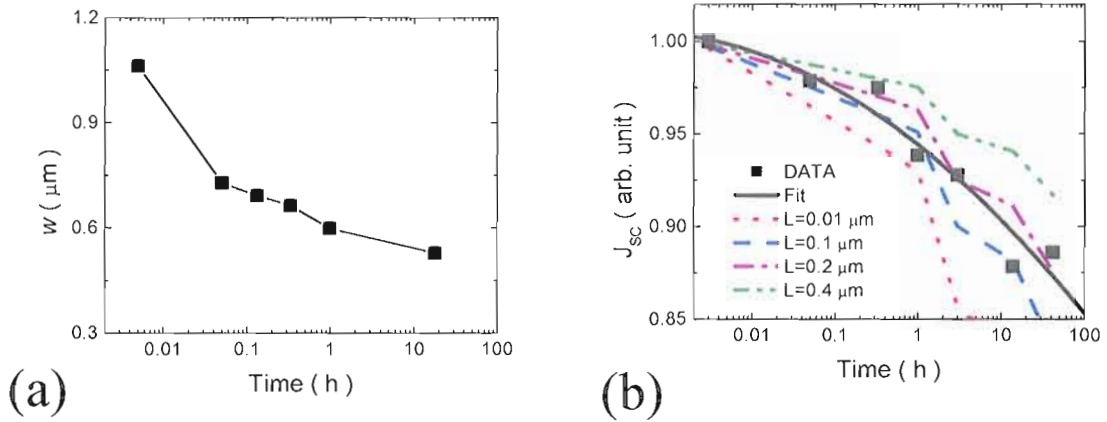


Fig. 5.7. Effect of light-soaking treatments on device parameters: (a) Changes in the depletion width and short circuit current with the extended hours of the light-soaking. (b) Measured values of J_{SC} at 300 K vs. the light-soaking time. Quadratic fit to the J_{SC} (solid line) can be well fitted with the calculated photo-generated current collection assuming minority diffusion length of $0.2 \mu\text{m}$.

recombination center indicated that we need another recombination center to compensate the increased recombination rate of the deep acceptor state, as the deep acceptor defect density increased with the light-soaking treatments. That is, we needed to keep the total recombination rate balanced through an inter-conversion of this new recombination center into the deep acceptor state. Before we go further into these details, we will continue investigating metastable changes in J - V device parameters in the next section.

5.1.4. Relationship between J - V device parameters

We investigated whether metastable behavior in J - V curves could be readily explained by a more fundamental parameter. We found that the decrease in J_{SC} was directly related to the decrease in the depletion width plus the minority carrier diffusion

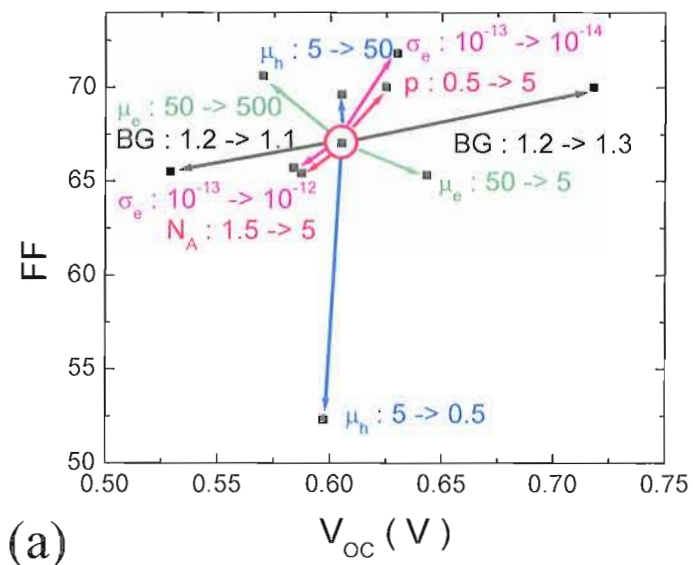
length as shown in Fig. 5.7(a). The experimentally observed decrease in J_{SC} was correctly simulated even with the deep acceptor recombination only, signifying simply that J_{SC} decreases as the depletion width decreases with the light-soaking. Since the carrier density increases almost by a factor of five, the depletion width decreases more than a factor of two as shown in the Fig. 5.7(a). The variation of depletion width was calculated from the high frequency depletion capacitance measurement at 150 K. Hence, we were able to correlate the changes in J_{SC} to a reduction in photo-carrier collection due to the shrinking of the depletion region.

The relative magnitude of carriers collected within approximately one diffusion length (L) from the edge of the depletion width w will be given [21] by

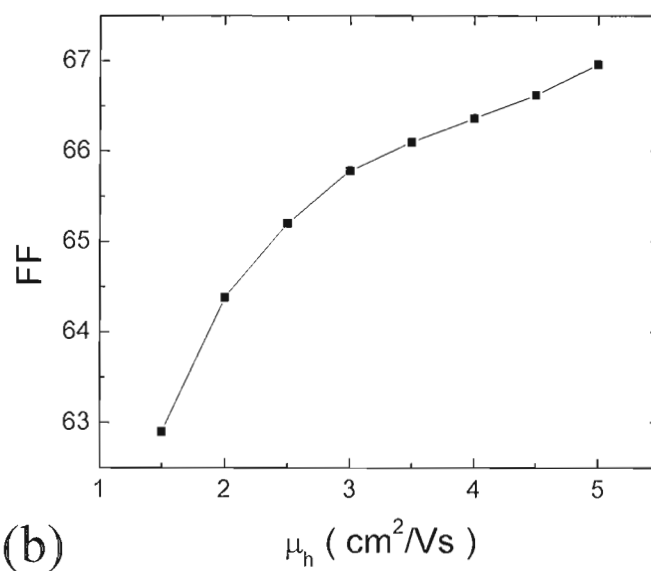
$$I_{L+w} \propto 1 - \frac{\exp(-\alpha w)}{\alpha L + 1} \quad (5.1)$$

where α is the optical absorption coefficient. We used an absorption coefficient of slightly smaller than $6 \times 10^4 \text{ cm}^{-1}$ to fit the decrease in the J_{SC} [25]. As shown in Fig. 5.7, the variation of w and J_{SC} were observed in logarithmic time scale. Changes in J_{SC} after the extended light-soaking treatments were fitted well with the calculated photo-generated current collection (dotted lines) assuming minority diffusion length of $0.2 \text{ }\mu\text{m}$ in Eq. 5.1. A recent study of carrier collection in the semi-transparent ZnO:Al back contact of CIGS thin film solar cell seems to support our estimation of the minority carrier diffusion length in the CIGS layer [22, 23].

Furthermore, we investigated whether the metastable changes in J_{SC} would be directly related to the decrease in depletion width and associated decrease in photo-



(a)



(b)

Fig. 5.8. Relationship between FF and hole carrier mobility (a) Sensitivity map for the baseline CIGS model (b) FF dependence on hole carrier mobility.

generated carrier collection during both the light-soaking and annealing processes. If the metastable changes for both the degradation and annealing processes are governed by the changes in the carrier density, the values of FF and J_{SC} would be controlled by a single parameter, such as the depletion width.

We attempted to simulate the metastable changes in FF with changes in p and N_T while keeping V_{OC} constant in the SCAPS modeling. However, we found that simple Shockley-Read-Hall (SRH) type recombination using a single defect could not account for the experimentally observed features in J - V curves, such as FF losses. While FF was one of the most important parameters of our metastability study in CIGS, it is also difficult to control without affecting other device parameters at the same time. Fig. 5.8(a) shows how vulnerable FF is to the changes made in the modeling parameters. It seems clear that the changes only in p and N_A can not adequately account for the FF loss. Given the constant V_{OC} during the metastability in CIGS, μ_h appears to be better correlated with FF , although several parameters could be adjusted to account for the similar change in FF . Note that FF drops rapidly as μ_h decreases below $3 \text{ cm}^2/\text{Vs}$ in Fig. 5.8(b).

We monitored the changes in the device parameters both during the light-soaking and the subsequent annealing processes. As shown in Fig. 5.9, FF deteriorated and recovered about three times faster than I_{SC} for both the light-soaking and the annealing kinetics in a semi-logarithmic fashion. We suspect the cubic nature in the I - V curve at the maximum power point where ($I_m \sim V_m^3$) is determining the different rate of metastable changes in I_{SC} and FF .

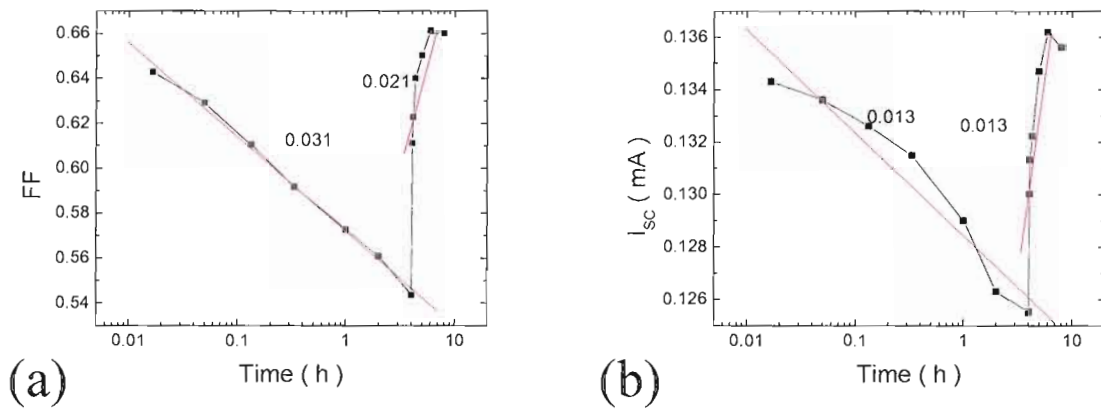


Fig. 5.9. Metastable FF and J_{SC} changes for CIGS #33713 at 300 K: semi-logarithmic plot of FF (a) and J_{SC} (b). Sample has been light-soaked for 4 hours at 100 mW/cm^2 and kept in the dark for recovery. Annealing process begins after 4 hours of light-soaking.

If FF and J_{SC} are related by such a rate in kinetics, then the changes in FF and J_{SC} might be governed by a single entity, such as the depletion width. Moreover, there should be only 1:1 correspondence between FF and J_{SC} if they are controlled by the same single parameter. However, the FF vs. J_{SC} in Fig. 5.10(a) shows different trajectories for the light-soaking and the annealing. Also the fact that there is not much reverse bias effect on the photo-current collection in the I - V curves after a series of light soaking indicates that there are more than a single mechanism is occurring with the light-induced metastable deep trap creation in addition to the changes in the carrier density. Therefore, while change in the carrier collection length accounts for many of the observed changes in device performance, another kind of mechanism is required to explain some of the other metastable changes in the device parameters.

Changes in J_{SC} seem to correlate well with the hole carrier mobility μ_h for both the light-soaking and annealing processes. Keeping in mind that conductivity of the CIGS

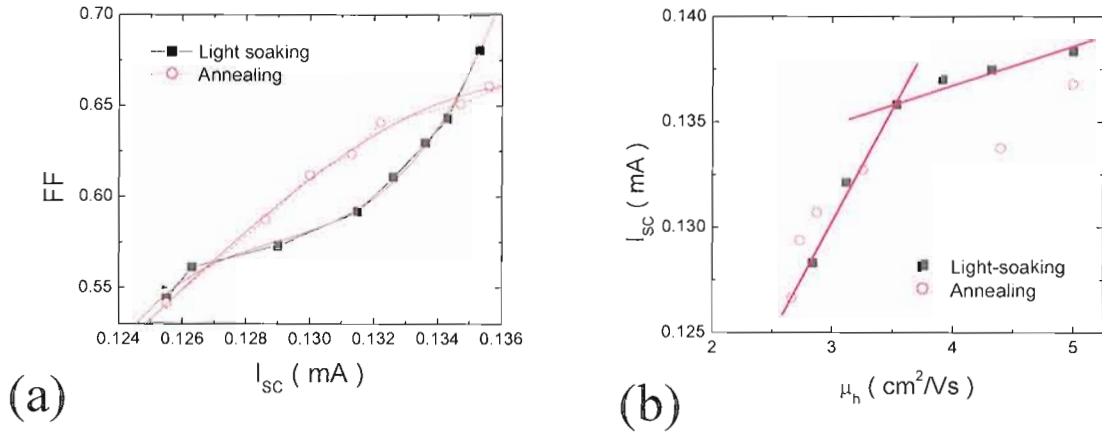


Fig. 5.10. Relationship between I_{SC} and hole carrier mobility: (a) Hysteresis-like trajectories between FF and I_{SC} during the light-soaking and the following annealing process. Both values decrease continuously with the light-soaking and increase with annealing in the dark at 300 K. The relationship between FF and I_{SC} has been fitted to the cubic power. (b) Changes in I_{SC} seem to be correlated well with the hole carrier mobility for both light-soaking and annealing processes.

layer did not change with the metastable defect creation, μ_h is inversely proportional to the free carrier density p during the light-soaking and annealing processes. Thus, the decrease in μ_h might be causing the reduction in the carrier collection that leads to the decrease in I_{SC} . Since most of the changes in I_{SC} tended to occur after there were significant decreases in μ_h below a critical value of 3.5 cm²/Vs, there were two different regimes in Fig. 5.10(b). Note that for lower mobility a clear relationship exists between I_{SC} and μ_h for both light-soaking and annealing processes. In fact, we have previously observed a correlation between I_{SC} and Urbach energy E_U , in a series of samples grown under varying conditions. Therefore, the degree of structural disorder represented by the μ_h could be linked to the reduction in the carrier collection during the light-induced metastability in CIGS.

5.2. Detailed modeling of metastability in CIGS solar cells

5.2.1 Compensated donor-to-acceptor conversion model

We investigated a number of microscopic scenarios based on the idea that a constant V_{OC} is related to a constant recombination rate. We attempted to model the lack of changes in V_{OC} using the compensated donor-acceptor conversion model coupled with a small decrease in the electron density in the CdS layer n_{CdS} . The defect observed at 0.8 eV above the valence band from the TPC studies was assumed to be the donor defect and was included as a second recombination center in this modeling. Since the conversion from the donor into the deep acceptor will generate an extra free (hole) carrier, this donor defect state would be consistent with the Lany-Zunger's complex divacancy model and the TPC-revealed mid-gap defect state. It has been proposed that the structural reorganization of the specific defect site is the root cause of the metastability in CIGS: the $V_{Se}-V_{Cu}$ defect complex [19, 20]. By including the donor defect states as a second recombination center, we were then able to successfully model both the decrease in J_{SC} and the lack of change in V_{OC} at the same time as shown in Fig. 5.11(b). Note that the shallow acceptor density needs to be compensated by the donor density in this model as follows.

$$p = N_A^{shallow} - N_D \quad (5.2)$$

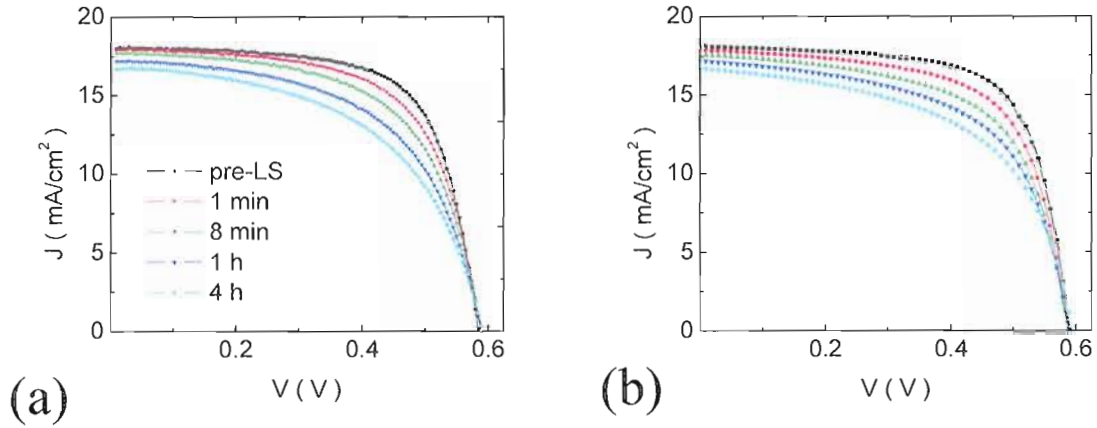


Fig. 5.11. SCAPS modeling of light-induced metastability in CIGS (a) Experimental J - V curves during the light-soaking at 780 nm at 300 K. (b) SCAPS simulation of the compensated donor-acceptor conversion model with decrease in n_{CDS} change.

Because adding donor will decrease the total number of free hole carriers, the shallow acceptor density needs to increase by the same amount of added donor so that the total free (hole) carrier density should be same to maintain the charge neutrality condition.

We investigated a number of equivalent models by maintaining a proper level of compensation between the donor type of defect and the shallow acceptor state according to Eq. 5.2. As shown in the Fig. 5.12, we found that the energy position of the donor defect and its defect density can affect the other device parameters so that the proper values of donor defect have been adopted for the actual modeling. A donor defect near mid-gap (E_D between 0.6 and 0.8 eV) with a reasonable compensation level compared to the shallow acceptor density was chosen to fit the experimental J - V curves.

Finally, SCAPS modeling with both deep acceptor N_A and deep donor N_D as recombination centers showed a good agreement with our experimental J - V data assuming a more reasonable electron capture cross-section σ_n of $5 \times 10^{-13} \text{ cm}^2$ for the deep

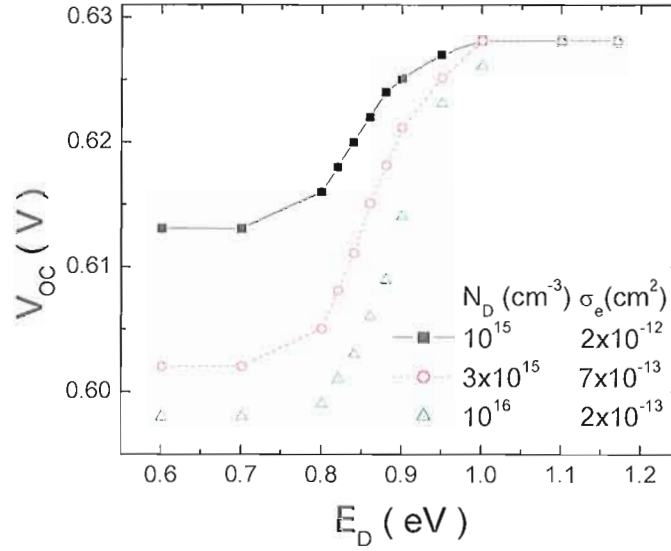


Fig. 5.12. V_{OC} dependence on the donor defect state. The product of N_D and σ_e were constant to keep the recombination rate same for different level of N_D compensation. N_D of $3 \times 10^{15} \text{ cm}^{-3}$, σ_e of 10^{-13} cm^2 , and E_D between 0.6 and 0.8 eV (circle) have been used for the actual SCAPS modeling.

acceptor defect. Furthermore, according to the Shockley-Read-Hall (SRH) formalism [24], this value of σ_n is consistent with the previous determined value of minority (electron) diffusion length L of $0.2 \mu\text{m}$ obtained in section 5.1.4; Specifically,

$$L = \sqrt{\frac{kT}{q} \cdot \mu_n \tau_n} \approx 0.2 \mu\text{m} \quad (5.3)$$

$$\tau_n = \frac{1}{\sigma_n * N_D * v_{th}} \approx 1 \times 10^{-9} \text{ s} \quad (5.4)$$

where μ_n is the electron mobility, τ_n is the minority carrier lifetime (the mean time before an electron recombines with a hole), σ_n is the capture cross-section for electron, N_D is donor defect density and v_{th} is the thermal velocity for electron.

Table 5. 1 Baseline SCAPS parameters for modeling

Layer properties	CIGS		CdS	ZnO
W (μm)	2		0.05	0.2
E_g (eV)	1.2		2.4	3.3
ϵ/ϵ_0	13.6		10	10
N_{CB} (cm^{-3})	2×10^{18}		2.2×10^{18}	2.2×10^{18}
N_{VB} (cm^{-3})	2.2×10^{18}		1.8×10^{19}	1.8×10^{19}
μ_n (cm^2/Vs)	50		100	100
μ_h (cm^2/Vs)	5		25	25
$N_A^{shallow}, N_D^{shallow}$ (cm^{-3})	3×10^{15}		9×10^{17}	9×10^{17}
α ($1/\text{cm eV}^{1/2}$)	1×10^5		1×10^5	1×10^5
Single-distributed defect states	Donor	Acceptor	mid-gap	mid-gap
σ_e (cm^2)	5×10^{-13}	5×10^{-13}	10^{-17}	10^{-12}
σ_h (cm^2)	10^{-15}	10^{-15}	10^{-12}	10^{-15}
E_D, E_A (eV)	$E_V+0.6$ (or above)	$E_V+0.3$	$E_V+1.2$	$E_V+1.65$
N_D, N_A (cm^{-3})	2.5×10^{15}	1.5×10^{15}	10^{18}	10^{17}

However, we were not able to account for all of the features in the experimentally observed changes in J - V curves. We attributed the observed loss in J_{SC} and FF to the decrease in μ_h . Since the total number of recombination centers was kept constant by the inter-conversion between the donor and acceptor defects, μ_h no longer had as large an impact on the FF in the SCAPS modeling as before. Instead, we found that the electron carrier density in the CdS layer might play the role of reducing FF without affecting other device parameters as shown in table 5.1. In fact, we observed the red kink effect due to a limited photoconductivity in the CdS layer. With this additional assumption about the modeling, we were able to find a good agreement between this model and the experimental J - V curves after a series of light-soaking as shown in Fig.

Table 5.2 SCAPS parameters for the compensated donor-to-acceptor conversion model. p and N_A^{deep} were determined experimentally. Throughout the metastable changes $p=N_A^{shallow}-N_D$ was in 1:1 ratio with N_A^{Deep} .

$(\times 10^{15} \text{ cm}^{-3})$	$N_A^{shallow}$	p	μ_h	N_D	N_A^{deep}	n_{CdS}
Pre-LS	3	0.5	5	2.5	1.5	9.5×10^{17}
1 min	3	0.7	3.6	2.3	1.7	9.1×10^{17}
8 min	3	0.9	2.7	2.1	1.9	8.9×10^{17}
1 h	3	1.1	2.2	1.9	2.1	8.8×10^{17}
4 h	3	1.3	2	1.7	2.3	8.7×10^{17}

5.6(a). Baseline modeling parameters and additional changes for the compensated donor-to-acceptor conversion model are listed in Table 5.1 and 5.2.

5.3. Bifacial CIGS solar cells

5.3.1 Metastability in the bifacial CIGS solar cells

As discussed above, we have explored a number of microscopic scenarios for how the metastable changes in the CIGS absorbers might actually be taking place. Based on the idea of a constant recombination rate indicated by a constant V_{OC} during the metastability, the Lany/Zunger divacancy conversion model, and the TPC indicated defect at $E_V + 0.8 \text{ eV}$, we proposed the compensated donor-acceptor conversion model. In this section we demonstrate that we are not only able to account for the metastable effects observed on standard CIGS devices, but also on specially prepared bifacial CIGS solar cells. In the latter devices, it was possible to examine the $I-V$ characteristics using either front-side illumination or back-side illumination. While we measured $I-V$

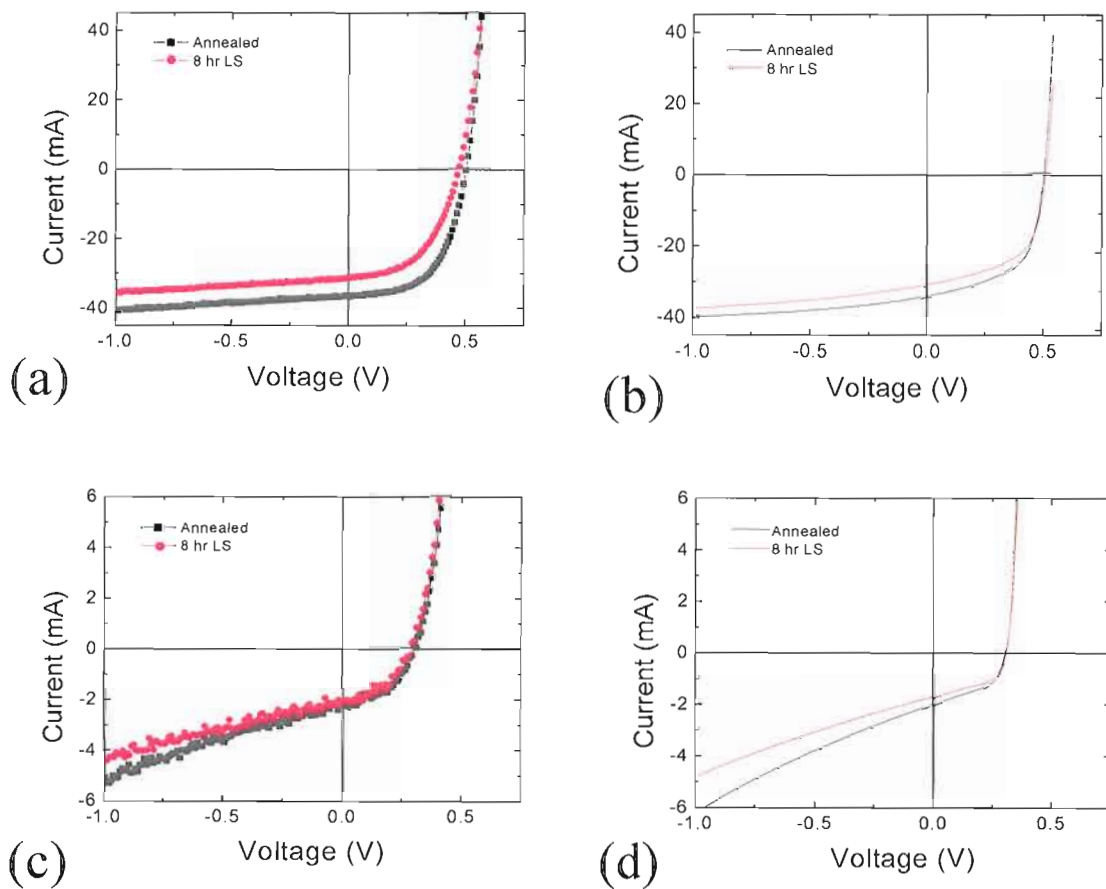


Figure 5.13. SCAPS modeling demonstrating the reverse bias I - V curve behavior of bifacial CIGS #33873.22 device (a) Experimental front-side I - V after 8 hr light-soaking at 980 nm at 250 K (b) SCAPS simulation for front side (c) Experimental back-side I - V after 8-hr light-soaking at 980 nm at 250 K (d) SCAPS simulation for back side.

characteristics using illumination from both sides of the device, all our light-soaking was carried out through the front side because there was almost 20 times attenuation through the 40 nm thick Mo back contact.

Fig. 5.13(a) and (c) show experimental I - V curves taken after a series of light-soaking treatments under 780 nm light for both front-side and back-side illumination. These data were measured under the same 50 mW/cm^2 , near-infrared illumination with a

small additional amount of 254 nm UV light, as described in section 3.3.2. As shown in Fig. 5.13(b) and (d), the donor-acceptor conversion model showed good agreement with light-soaking data for both front and back-side I - V curves on our bifacial sample using the same baseline modeling parameter set. We were again able to fit the decrease in I_{SC} and the lack of change in V_{OC} using the compensated donor-acceptor conversion model. Furthermore, we were able to match the reverse-bias I - V curves for the annealed and light-soaked states. Note that there is large gradient in current collection under the reverse bias voltage for the back-side I - V curves.

Because photo-generated charge carriers can be collected when they are created within one diffusion length from the edge of the depletion region of the device, reverse bias voltage increases carrier collection for the back side I - V curve as shown in Fig 5.13(c). Since the number of photons absorbed decays exponentially from the illuminated side of the device, the effect of the increased depletion width effect is negligible for front-side illumination because the depletion width ($\sim 1 \mu\text{m}$) is already large compared to the absorption length of the light ($\sim 0.16 \mu\text{m}$ for 780 nm light and $\sim 0.38 \mu\text{m}$ for 980 nm light) [25]. On the other hand, there are very few carriers to be collected outside the depletion width for back-side illumination. Since most carriers are generated near the back surface at zero bias, a substantial increase in carrier collection should be observed under reverse bias. Because we can match both front and back-side I - V data of the bifacial CIGS solar cells even in the reverse bias, we used the compensated donor-acceptor conversion model to predict a device performance based on the variation in the key electronic properties in the last section of this chapter.

5.3.2 Temperature and intensity dependence of I - V curves

We further investigated the temperature dependence of I - V curves of the bifacial CIGS solar cells to learn more about the source of metastability. Fig. 5.14 shows the temperature dependence of the V_{OC} under both front- and back-side illumination for several different light intensities. It is generally accepted that V_{OC} is equal to the splitting of the quasi-Fermi levels that occurs under open circuit conditions [35], that is,

$$qV_{oc} = (E_{Fn} - E_{Fp}) = (E_c - E_v) + kT \ln(np/N_c N_v) \quad (5.5)$$

$$V_{oc} = \Phi_b/q + kT/q \cdot \ln(p/N_c N_v) \ln(n) \approx \Phi_b/q - kT/q \cdot \ln(J'/J_L) \quad (5.6)$$

where E_{Fn} is the electron quasi-Fermi energy, E_{Fp} is the hole quasi-Fermi energy, Φ_b is the barrier height, J_L is the photocurrent which is proportional to light intensity, J' is used to make an argument in the logarithm dimensionless and electron density n is assumed to be proportional to J_L . If the dominant recombination pathway is governed by Shockley-Read-Hall type defect in the bulk CIGS layer, Φ_b is equal to Eg/q in the limit of $T \rightarrow 0$.

The bulk nature of the observed metastabilities in CIGS rather than interface effects is thus supported by the temperature dependence of the V_{OC} . We found that indeed $V_{OC} \rightarrow Eg/q$ as $T \rightarrow 0$ for the front-side illumination independent of light intensities, which indicates that the dominant recombination in the device takes place in the bulk of the absorber layer rather than at the interfaces.

Saturation of the front-side V_{OC} near 0.8 V was observed below 200 K. For CdTe solar cells, V_{OC} saturation used to be attributed to pinning of the quasi-Fermi level at the interface or bandtail recombination [26]. Since the electron quasi-Fermi level E_{Fn} cannot

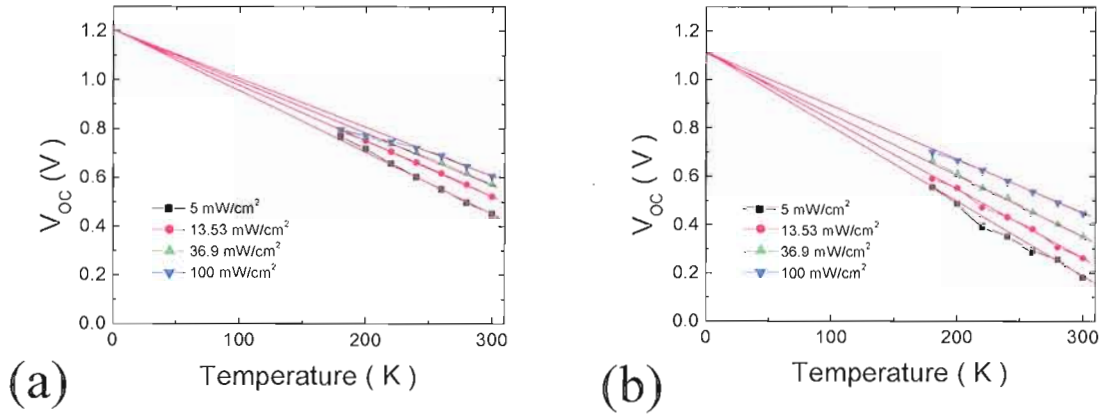


Figure 5.14. Temperature-dependence of V_{OC} for bifacial CIGS #33873.22 device at 980nm. (a) Front-side illumination showed $V_{OC} \rightarrow E_g/q$ as $T \rightarrow 0$. (b) Back-side barrier heights were shifted down by 0.1 V.

increase any further beyond the conduction band of the CdS layer at the interface, such pinning of quasi-Fermi level splitting in the low temperature could be argued qualitatively. Also, a high number of charged defects at the CdS/CIGS interface has been proposed to limit V_{OC} in the wide bandgap chalcopyrite solar cells [27]. However, we were not able to simulate the experimentally observed $V_{OC}(T)$ limitation below 200 K even with large number of interface states and a negative conduction band offset (CBO) in our modeling. One of the compelling ideas for the $V_{OC}(T)$ limitation is that V_{OC} may not exceed the built-in potential V_{BI} at the semiconductor junction. If the hole quasi-Fermi level E_{Fp} cannot move any closer to E_V in order to maintain certain level of hole free carrier density p as temperature goes down and E_{Fn} is pinned at the conduction band of the CdS layer at the interface, the maximum allowable V_{OC} is further limited by V_{BI} [28]. In fact, a typical value of V_{BI} can be estimated from the simple relation between depletion width w ($\sim 1 \mu\text{m}$) and free carrier density p ($\sim 10^{15} \text{ cm}^{-3}$),

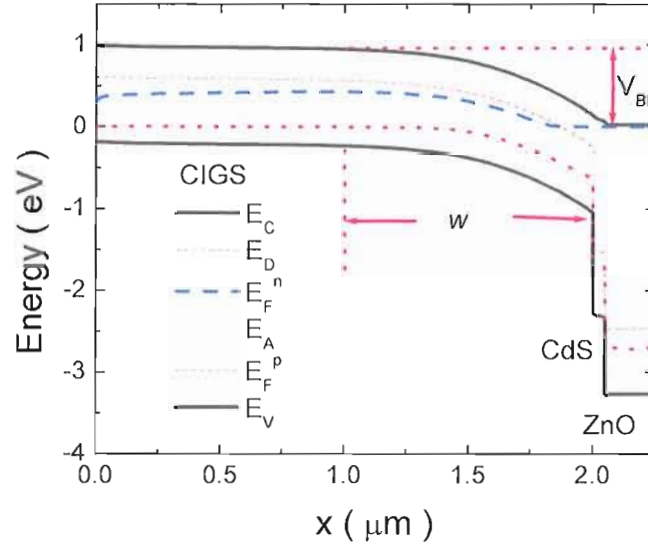


Fig. 5.15. Energy band diagram showing pinning of electron quasi-Fermi level at CIGS/CdS interface at 300 K. $V_{OC}(T)$ does not saturate in the SCAPS modeling.

$$V_{BI} = \frac{qpw^2}{2\epsilon} \approx 0.8V \quad (5.7)$$

For back-side illumination, the barrier height was found to be 0.1 eV lower than E_g , slightly lower than the 1.2 eV bandgap value. There are several possible explanations for the decrease. Electrons generated by back side illumination have to diffuse back to be collected by the field gradient in the depletion region. Since absorption length of 980 nm light is relatively short ($\sim 0.38 \mu\text{m}$), there exists additional electron carrier diffusion current toward the depletion region. The principle of detailed balance requires that there should be a hole drift current to cancel part of this diffusion current under open circuit conditions and so reduce the barrier potential across the device. Also, blocking the second junction at the Mo back contact can give rise to the reduction in the barrier height.

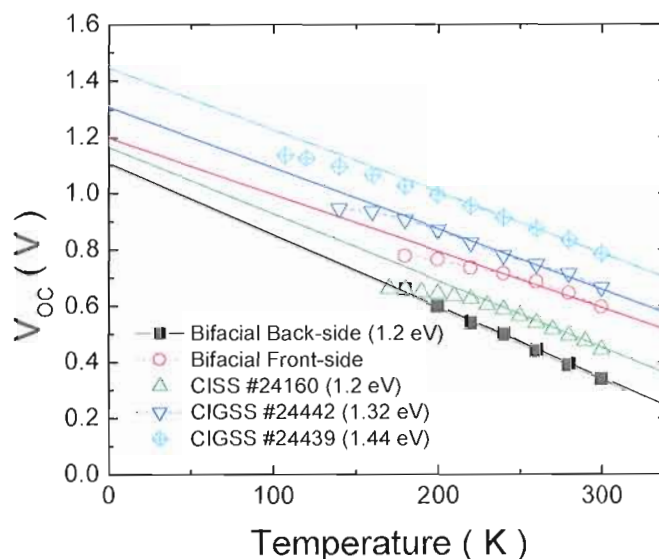


Fig. 5.16. Temperature dependence of V_{OC} for bifacial CIGS, CISS and CIGSS devices. Temperature dependences of V_{OC} start to saturate at temperature below 200 K. Linear extrapolations of V_{OC} at temperature above 240 K lead to $\Phi_b \approx E_g/q$ at 0 K for CIGS solar cells.

In a working solar cell, unless the back contact is perfectly ohmic, the metal work function will result in a second junction barrier at the back contact. When the device is illuminated from the back side, this junction could create a small electric field near the back contact, reducing the potential across the device.

The temperature dependences of V_{OC} for several wide-bandgap chalcopyrite solar cells measured under 1 sun intensity are summarized in Fig 5.16. Most devices showed a pronounced roll-over feature at a low temperature region regardless of bandgap. Linear fits based on relatively linear regions in temperatures between 240 K and 300 K gave well-behaved intercepts of Φ_b at 0 K which matched the bandgap energies for these devices. Different levels of saturation of the V_{OC} were observed for different devices. A

pinning of the electron quasi-Fermi level either by a high degree of charged defects at the CdS/CIGS interface or by the positive CBO (cliff-like) at the CdS/CIGS interface may be responsible for the V_{OC} saturation observed at low temperature.

5.3.3 I - V curve roll-over at low temperatures

Fig. 5.17 shows a set of white light-illuminated I - V curves at different temperatures for CISS #24160 before and after light-soaking at RT using white light. White light-soaking for 12 hours at RT improves current collection above the V_{OC} . Temperature dependence of V_{OC} shows a clear indication of saturation at low temperatures, although there is a hint of recovery after the light treatment. V_{OC} at a low temperature region were observed to increase by about several tens of meV after a light-soaking treatment. The variation in the barrier height Φ_b used to be ascribed to explain this roll-over for the CdTe solar cells [31]. Reversed polarity of the back contact diode can limit the hole current flow especially at low temperatures. We were able to simulate such roll-over effects in I - V curves in the SCAPS modeling simply by using the back contact barrier height Φ_b of 0.24 eV. Barrier height at 0 K for both curves turned out to be equal to the band gap of CISS in Fig.5.18, which indicates that major recombination occurs through the bulk CISS layer, not at the interface.

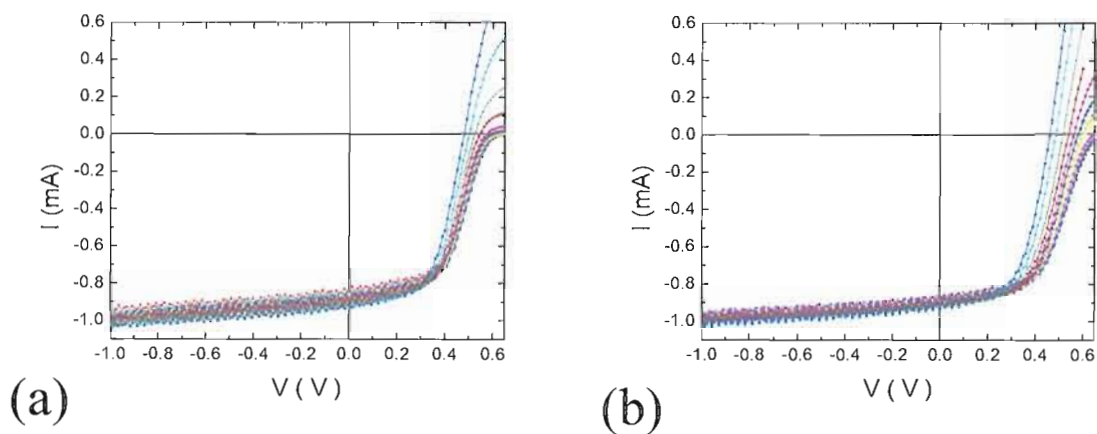


Figure 5.17. Temperature dependence of white IV for CISS #24160 (a) before light-soaking (b) after light-soaking for 12 hours at RT

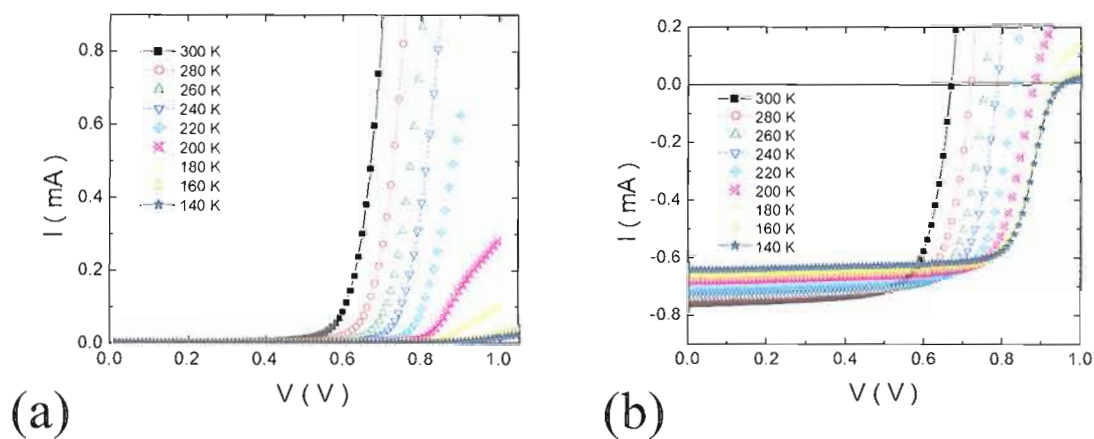


Fig. 5.18. Temperature dependence of $I-V$ curves for CIGSS #24442. (a) Dark $I-V$ curves (b) White light $I-V$ curves

5.4 Mobility limitation on the CIGS device performance

We were able to determine the majority hole carrier mobility μ_h around 3-22 cm^2/Vs in the CIGS layer through high frequency AS measurements. While the traditional characterization method requires Hall and coplanar resistivity measurements on the specially prepared insulating substrate, our high frequency AS measurement technique can be applied upon the working solar cell configuration. As light-soaking treatments reduce μ_h below the critical value of 3 cm^2/Vs , we found a significant drop in the device performance. Since μ_h seems to serve a good metric for device performance during the metastable degradation process even for the high performance CIGS solar cells, we hope to explore whether there is a critical mobility limit on device performance.

As pointed out by Schiff et. al. for a-Si:H solar cells, a-Si:H is likely a low mobility solar cell in which drift mobility ranging around 10^{-2} cm^2/Vs is by far lower than a critical mobility of about 1 cm^2/Vs for a good carrier transport [32]. Bandtail trapping is likely the root cause in reducing the effective mobility of the carriers in a-Si:H, since the mobile carriers get trapped and become immobile in the bandtail states [33]. Therefore, CIGS is also on the brink of efficiency limitation even with relatively higher mobility if significant levels of recombination centers exist in the bulk CIGS [34].

Considering that electron mobility is typically larger for most solar cells, the hole carrier mobility μ_h is likely limiting the device performance in CIGS as shown in Fig. 5.19. As μ_h drops below the critical value of 3 cm^2/Vs in the modeling, a significant

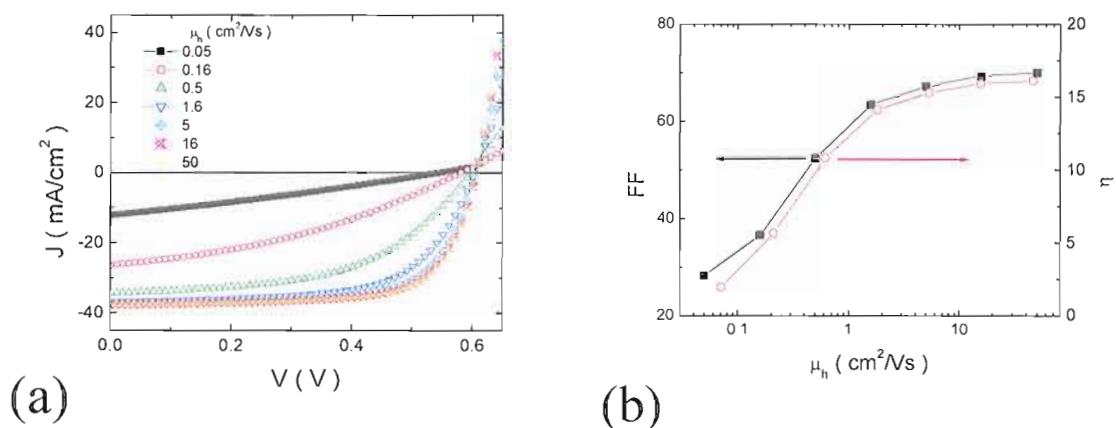


Fig. 5.19. Effect of hole mobility on CIGS device performance obtained from SCAPS modeling as μ_h varies from 0.05 to 50 cm²/Vs (a) Significant J - V curve changes occurs if μ_h drops below the critical value of 3 cm²/Vs (b) FF (filled symbols) and efficiency η (open symbols) dependences on μ_h .

decrease in the device performance is apparent in the J - V curves. Note that V_{OC} does not stay constant while μ_h decreases below the critical mobility limit; contrary to the initial assumption that only the recombination process determines V_{OC} at the interface. Overall, μ_h seems to play an important role in determining η as μ_h drops below the critical value whereas η becomes saturated even with larger value of μ_h .

Notes

- [1] S. Siebentritt and U. Rau, *Wide-Gap Chalcopyrites* (Springer, 2006).
- [2] J. T. Heath, J. D. Cohen, W. N. Shafarman, D. X. Liao, and A. A. Rockett. *Appl. Phys. Lett.* **80**, 4540 (2002).
- [3] T. Nakada, Ma. Hongo, and E. Hayashi, *Thin Solid Films* **431-432**, 242 (2000).
- [4] T. Nakada and M. Mizutani. *Jpn. J. Appl. Phys.* **41**, L165 (2002).
- [5] X. Liu, J. R. Sites, *Proc. AIP Conf.* **444** (1996).
- [6] G. B. Turner, R. J. Schwartz, J. L. Gray, in *Proc. 20th IEEE Photovolt. Spec. Conf.*, 1457 (1988).
- [7] S. Wei and A. Zunger, *Appl. Phys. Lett.* **78**, 3846 (1995).
- [8] A. Niemegeers, M. Burgelman and A. De Vos., *Appl. Phys. Lett.* **67**, 843 (1995).
- [9] D. Schmid, M. Ruckh, F. Grunwald and H.W. Schock, *J. Appl. Phys.* **73**, 2902 (1993).
- [10] J. Lee, J. T. Heath, W. N. Shafarman, and J. D. Cohen, in *Conference Record of IEEE 4th World Conference on Photovoltaic Energy Conversion*, **1**, 360 (2006).
- [11] J. Lee, D. B. Needleman, W. N. Shafarman, and J. D. Cohen, in *Materials Research Society Proc.* **1012**, Y.12.02 (2007).
- [12] U. Rau, in *Materials Research Society Proc.* **668**, H9.1.1 (2001).
- [13] M. Igalson and H. W. Schock, *J. Appl. Phys.* **80**, 5765 (1996).
- [14] J.T. Heath, J.D. Cohen, and W.N. Shafarman, *J. Appl. Phys.* **95**, 1000 (2004).
- [15] I. L. Repins, B. J. Stanbery, D. L. Young, S. S. Li, W. K. Metzger, C. L. Perkins, W. N. Shafarman, M. E. Beck, L. Chen, V. K. Kapur, D. Tarrant, M. D. Gonzalez, D. G.

Jensen, T. J. Anderson, X. Wang, L. L. Kerr, B. Keyes, S. Asher, A. Delahoy, B. Von Roedern Prog. Photovolt.: Res. and Appl. **14**,. 25 (2005).

[16] J. Lee, J. T. Heath, W. N. Shafarman, and J. D. Cohen, in Materials Research Society Proc. **865**, F12.4.1 (2005).

[17] J. Guillemoles, U.Rau, Adv. Mater **11**, 957 (1999).

[18] U. Rau, M. Schmitt, D. Hilburger, F. Engelhardt, O. Seifert, J. Parisi, W. Riedl, J. Rimmasch, and F. Karg, in *Proceedings of the 26th IEEE Photovolt. Spec. Conf.*, **371**, (1997).

[19] S. Lany and A. Zunger, J. Appl. Phys. **100**, 113725 (2006).

[20] S. Lany and A. Zunger, Phys. Rev. Lett. **100**, 016401 (2008).

[21] S. S. Hegedus and W. N. Shafarman, Prog. Photovolt: Res. Appl. **12**, 155 (2004).

[22] U. Rau, A. Jasenek, H. W. Schock, F. Engelhardt, T. Meyer, Thin Solid Films **361**, 298 (2000).

[23] J. Mattheis, P. J. Rostan, U. Rau, J. H. Werner, Sol. Energy Mater. Sol. Cells, **91**, 689 (2007).

[24] M. Burgelman, P. Nollet, and S. Degrave, Thin Solid Films **361**, 527 (2000).

[25] P. D. Paulson, R. W. Birkmire, and W. N. Shafarman, J. Appl. Phys. **94**, 879 (2003).

[26] K.L. Chopra, P.D. Paulson, and V. Dutta, Prog. Photovolt: Res. Appl. **12**, 69 (2004).

[27] M. Gloeckler, Thin Solid Films **480**, 241 (2005).

[28] J. H. Lyou, E. A. Schiff, S. Guha, and J. Yang, *Appl. Phys. Lett.* **78**, 1924 (2001).

[29] R.S. Crandall, J. Appl. Phys. **55**, 4418 (1984).

[30] R.S. Crandall, J. Appl. Phys. **54**, 7176 (1983).

- [31] T. McMahon, A. Fahrenbruch, in *Proc. 28th IEEE Photovolt. Spec. Conf.*, **549**, (2000).
- [32] E. A. Schiff, *Sol. Energy Mater. Sol. Cells* **78**, 567 (2003).
- [33] N. F. Mott, *J. Phys. C.* **13**, 5433 (1980).
- [34] J. Mattheis, J. H. Werner, and U Rau, *Phys. Rev. B* **77**, 085203 (2008).
- [35] R. A. Street, *Hydrogenated Amorphous Silicon* (Cambridge University Press, 1991).

CHAPTER VI

SUMMARY AND CONCLUSIONS

The research in this thesis aimed for directed toward gaining a detailed understanding of the metastability in the CIGS based solar cells. My experimental results were based on high frequency admittance spectra (AS) and J - V measurements on the high performance IEC CIGS solar cells. Numerical simulations based on SCAPS-1D illustrated the role of bulk defect states, free hole carrier density, and hole carrier mobility on the device performance while metastable changes were made in CIGS thin films.

Metastability studies on working device configurations have distinct advantages over the conventional research techniques on sub-bandgap defect states with many samples because: (1) metastability research does not require a repeatable series of samples and (2) it can be studied while many other device parameters are kept constant (e.g. chemical composition, grain-boundary, and buffer/interface layer) so that changes in the CIGS bulk absorber properties can be less ambiguously correlated to the electronic sub-bandgap defect states. Using metastable changes in CIGS to investigate the effects of the defect states on device performance, we found that metastability can be driven either by light-soaking or by applying forward dc voltage bias. The density of the electronic defect states located at 0.3 eV above the valence band and the density of the

majority (hole) carrier density were observed to increase in a 1:1 ratio regardless of methods used to create them. The metastable defect creation kinetics follows a sub-linear power law in time and intensity. This indicates that electronic properties in CIGS degrade due to the capture of electrons, as is consistent with the theoretical model $V_{Cu}-V_{Se}$ defect complex suggested by Lany and Zunger. However, a comparison of CV and DLCP profiles indicated that a considerably high density of deep defect states is localized near the barrier interface after light-soaking treatments.

From the AS and DLCP measurement results at varying temperatures and at different reverse biases, we were able to deduce the majority hole carrier mobility μ_h to vary over the range 3-22 cm^2/Vs . We were not able to find any correlation between μ_h and the cell efficiencies within this range. However, we did find that there was a significant drop in the device performance if the metastable degradation resulted in a μ_h smaller than 3.5 cm^2/Vs . A significant drop in device performance was likewise found when μ_h was chosen to be below the critical value of about 3 cm^2/Vs in the SCAPS modeling.

We found that there were two different activation energies in the thermal admittance spectra and that the activation energy of deep trap states decreased with the light-soaking treatments following the Meyer-Neldel rule. Further light-soaking treatments caused the activation energy of the deep trap states to eventually saturate at the activation energy of the shallow acceptor level. Both thermal activation energies seem to originate from the same defect states. Also note that different metastable states have the same emission rate at the iso-kinetic temperature around RT.

We were able to account for the metastable changes in J_{SC} with the changes in carrier collection length. Changes in J_{SC} after extended light-soaking treatments were well accounted for by the reduced photo-generated current collection ratio assuming minority diffusion length of 0.2 μm . As the majority hole carrier density increases with light-soaking, the depletion width decreases and so does the carrier collection. However, another kind of mechanism is required to explain metastable changes in FF . Since different rates of FF and J_{SC} changes were not be controlled by a single parameter, such as depletion width, we attribute this instead to the more fundamental parameter, μ_h . The overlap of J_{SC} vs. μ_h for both the degradation and annealing processes demonstrates such μ_h effects on device performance. Numerical modeling shows that device performance parameters, such as FF and η , significantly decrease if μ_h drops below a critical mobility value of 3 cm^2/Vs .

Temperature dependence of V_{OC} suggests that the dominant recombination center is in the bulk CIGS layer, not at the interface. It is of high interest that V_{OC} does not change at all with near-infrared light-soaking while other device parameters, such as J_{SC} and FF , degrade upon light-soaking treatments and anneal back in the dark at RT. Saturation of V_{OC} is observed below 200 K for all chalcopyrite solar cells, including wide bandgap CIGS devices with higher Ga fractions.

We considered a number of microscopic models to obtain a detailed understanding of the electronic properties during the metastability in CIGS. For example, we attempted to understand the lack of any change in V_{OC} during metastable changes using the compensated donor-acceptor conversion model. Adding a donor defect at 0.8

eV above the valence band as an additional recombination center possibly explains the lack of change in V_{OC} . Using this compensated donor-acceptor conversion model, we were able to account for the metastable effects observed not only on the standard CIGS devices but also on specially prepared bifacial CIGS solar cells. However, this assumption needs to be further tested experimentally for other high bandgap alloys produced by other types of compositional alloying.

REFERENCES

Chapter I

- [1] N. S. Lewis, and D. G. Nocera, *Science*, **103**, 15729 (2006).
- [2] N. S. Lewis, *Science*, **798**, 1137014 (2007).
- [3] G. W. Crabtree and N. S. Lewis, *Physics Today*, **60**, 37 (2007).
- [4] International Energy Agency, *World Energy Outlook 2007*, URL <http://www.worldenergyoutlook.org/2007.asp>.
- [5] G. M. Whitesides and G. W. Crabtree, *Science*, **315**, 796 (2007).
- [6] G. Cody, T. Tiedje, in *Proc. 25th IEEE Photovoltaic Specialist Conf.* (1996), pp. 1521-1524.
- [7] Solarbuzz, *Marketbuzz 2007*, URL <http://www.solarbuzz.com/Marketbuzz2008-intro.htm>.
- [8] K. Zweibel, J. Mason, V. Fthenakis, A Solar Grand Plan, *Sci. Am.* **298**, 64 (2008), URL <http://www.sciam.com/article.cfm?id=a-solar-grand-plan> (2007).
- [9] M. A. Green, K. Emery, D. L. King, Y. Hisikawa, W. Warta, *Prog. Photovolt.: Res. Appl.* **14**, 45 (2006).
- [10] M. C. Beard, K. P. Knutsen, P. Yu, J. M. Luther, Q. Song, W. K. Metzger, R. J. Ellingson, and A. J. Nozik, *Nano Lett.*, **7**, 2506 (2007).
- [11] R. N. Bhattacharya, M. A. Contreras, B. Egaas, R. N. Noufi, *Appl. Phys. Lett.* **89**, 253503 (2006).
- [12] K. Ramanathan, M. A. Contreras, C. L. Perkins, S. Asher, F. S. Hasoon, J. Keane, D. Young, M. Romero, W. Metzger, R. Noufi, J. Ward, and A. Duda, *Prog. Photovolt.: Res. Appl.* **11**, 225 (2003).
- [13] A. Luque and S. Hegedus, *Handbook of Photovoltaic Science and Engineering*, Hoboken (2003).

Chapter II

- [1] S. M. Sze, *Semiconductor Devices, Physics and Technology* (John Wiley & Sons, Inc., 2002).

- [2] P. Blood and J. W. Orton, *The Electrical Characterization of Semiconductors: Majority Carriers and Electron States* (Academic Press, London, 1992).
- [3] J. W. Orton and P. Blood, *The Electrical Characterization of Semiconductors: Measurement of Minority Carrier Properties* (Academic Press, London, 1990).
- [4] A. L. Fahrenbruch and R. H. Bube, *Fundamentals of Solar Cells* (Academic Press, 1983).
- [5] S. Siebentritt and U. Rau, *Wide-Gap Chalcopyrites* (Springer, 2006).
- [6] N. W. Ashcroft and N. D. Mermin, *Solid State Physics* (Saunders, 1976).
- [7] Richard Zallen, *The Physics of Amorphous Solids* (John Wiley & Sons, Inc., 1983).
- [8] A. D. Compaan, *J. Metals* **59**, Iss. 12, p. 31 (2007).
- [9] M. Gloeckler, J. R. Sites, and W. K. Metzger, *J. Appl. Phys.* **98**, 113704 (2005).
- [10] B.J. Stanberry, PhD dissertation (University of Florida, Gainesville, 2001).
- [11] J. T. Heath, J. D. Cohen, W. N. Shafarman, D. X. Liao, and A. A. Rockett, *Appl. Phys. Lett.* **80**, 4540 (2002).
- [12] S. Lany and A. Zunger, *J. Appl. Phys.* **100**, 113725 (2006).
- [13] H. W. Schock and R. Noufi, *Prog. Photovolt.: Res. Appl.*, **8**, 151 (2000).
- [14] W. N. Shafarman, R. Klenk, and B. E. McCandless, *J. Appl. Phys.* **79**, 7324 (1996).

Chapter III

- [1] P. Y. Yu, M. Cardona, *Fundamentals of Semiconductors* (Springer, 1996), 3rd ed.
- [2] J. D. Cohen, A. V. Gelatos, *Amorphous Silicon and Related Materials* (World Scientific, 1988), p. 475.
- [3] H. Ibach, H. Lüth, *Solid-State Physics* (Springer, 2003), 2nd ed.
- [4] N. Peyghambarian, S. W. Koch, and A. Mysyrowicz, *Introduction to Semiconductor Optics* (Prentice-Hall, 1993).
- [5] M. Burgelman, P. Nollet and S. Degrave, *Thin Solid Films* **361-362**, 527 (2000).

- [6] S. M. Sze, *Physics of Semiconductor Devices* (John Wiley & Sons, 1981), 2nd ed.
- [7] J. T. Heath, W. N. Shafarman, and J. D. Cohen, *J. Appl. Phys.* **95**, 1000 (2004).
- [8] J. Lee, J. T. Heath, W. N. Shafarman, and J. D. Cohen, in *Materials Research Society Proc.* **865**, F12.4.1 (2005).
- [9] A. Niemegeers, M. Burgelman, R. Herberholz, U. Rau, D. Hariskos, and H. W. Schock, *Prog. Photovolt.: Res. Appl.* **6**, 407 (1998).
- [10] R. Herberholz, M. Igalson, and H. W. Schock, *J. Appl. Phys.* **83**, 318 (1998).
- [11] J. Lee, D. B. Needleman, W. N. Shafarman, and J. D. Cohen, *Materials Research Society Proc.* **1012**, Y.12.02 (2007).
- [12] A. Klein and W. Jaegermann, *Appl. Phys. Lett.* **74**, 2283 (1999)
- [13] U. Rau, D. Braunger, R. Herberholz, H. W. Schock, J. -F. Guillemoles, L. Kronik and D. Cahen, *J. Appl. Phys.* **86**, 497 (1999).
- [14] J. Lee, J. D. Cohen and W. N. Shafarman, *Thin Solid Films* **480-481**, 336 (2005).
- [15] S. S. Hegedus, W. N. Shafarman, *Prog. Photovolt.: Res. Appl.* **12**, 155 (2004).
- [16] U. Rau, *Appl. Phys. Lett.* **74**, 111 (1999).
- [17] A. O. Pudov, J. R. Sites, M.A. Contreras, T. Nakada and H. W. Schock, *Thin Solid Films*, **480-481**, 273 (2005).
- [18] J. Lee, J. T. Heath, W. N. Shafarman, and J. D. Cohen, in *Conference Record of IEEE 4th World Conference on Photovoltaic Energy Conversion*, **1**, 360 (2006).

Chapter IV

- [1] K. Ramanathan, M. A. Contreras, C. L. Perkins, S. Asher, F. S. Hasoon, J. Keane, D. Young, M. Romero, W. Metzger, R. Noufi, J. Ward, and A. Duda, *Prog. Photovolt.: Res. Appl.* **11**, 225 (2003).
- [2] Shockley and Queisser, *J. Appl. Phys.* **32**, 510 (1961).
- [3] J. Lee, J. T. Heath, W. N. Shafarman, and J. D. Cohen, in *Materials Research Society Proc.* **865**, F12.4.1 (2005).

- [4] D. Redfield and R. H. Bube, *Photoinduced Defects in Semiconductors*, (Cambridge University Press, 1996).
- [5] J. Kneisel, K. Siemer, I. Luck, and D. Braunig, *J. Appl. Phys.* **88**, 5474 (2000).
- [6] M. Gloeckler, J. R. Sites, and W. K. Metzger, *J. Appl. Phys.* **98**, 113704 (2005).
- [7] M. Gloeckler and W. K. Metzger, *J. Appl. Phys.* **98**, 063701 (2005).
- [8] W. Meyer and H. Neldel, *Z. Tech. Phys.* **12**, 588 (1937).
- [9] R.S Crandall, in *Materials Research Society Proc.* **763**, B2.5.1 (2003).
- [10] M. Stutzmann, W. B. Jackson, and C. C. Tsai, *Phys. Rev. B* **32**, 23 (1985).
- [11] M. Stutzmann, W. B. Jackson, and C. C. Tsai, *Phys. Rev. B* **34**, 63 (1986).
- [12] A. Yelon, B. Movaghar, and H. M. Branz, *Phys. Rev. B* **46**, 12244 (1992).
- [13] R. Herberholz, M. Igalson, and H. W. Schock, *J. Appl. Phys.* **83**, 318 (1998).
- [14] U. Rau, D. Braunger, R. Herberholz, H. W. Schock, J.-F. Guillemoles, L. Kronik, and D. Cahen, *J. Appl. Phys.* **86**, 497 (1999).
- [15] M. Igalson and H. W. Schock, *J. Appl. Phys.* **80**, 5765 (1996).
- [16] S. Lany and A. Zunger, *Phys. Rev., B* **72**, 035215. (2005).
- [17] S. Lany and A. Zunger, *J. Appl. Phys.* **100**, 113725 (2006).
- [18] S. Lany and A. Zunger, *Phys. Rev. Lett.* **100**, 016401 (2008).
- [19] J. Lee, J. T. Heath, W. N. Shafarman, and J. D. Cohen, in *Conference Record of IEEE 4th World Conference on Photovoltaic Energy Conversion*, **1**, 360 (2006).
- [20] M. Gloeckler, PhD thesis (Colorado State University, Fort Collins, 2005).

Chapter V

- [1] S. Siebentritt and U. Rau, *Wide-Gap Chalcopyrites* (Springer, 2006).
- [2] J. T. Heath, J. D. Cohen, W. N. Shafarman, D. X. Liao, and A. A. Rockett. *Appl. Phys. Lett.* **80**, 4540 (2002).

- [3] T. Nakada, Ma. Hongo, and E. Hayashi, *Thin Solid Films* **431-432**, 242 (2000).
- [4] T. Nakada and M. Mizutani. *Jpn. J. Appl. Phys.* **41**, L165 (2002).
- [5] X. Liu, J. R. Sites, *Proc. AIP Conf.* **444** (1996).
- [6] G. B. Turner, R. J. Schwartz, J. L. Gray, in *Proc. 20th IEEE Photovolt. Spec. Conf.*, 1457 (1988).
- [7] S. Wei and A. Zunger, *Appl. Phys. Lett.* **78**, 3846 (1995).
- [8] A. Niemegeers, M. Burgelman and A. De Vos., *Appl. Phys. Lett.* **67**, 843 (1995).
- [9] D. Schmid, M. Ruckh, F. Grunwald and H.W. Schock, *J. Appl. Phys.* **73**, 2902 (1993).
- [10] J. Lee, J. T. Heath, W. N. Shafarman, and J. D. Cohen, in *Conference Record of IEEE 4th World Conference on Photovoltaic Energy Conversion*, **1**, 360 (2006).
- [11] J. Lee, D. B. Needleman, W. N. Shafarman, and J. D. Cohen, in *Materials Research Society Proc.* **1012**, Y.12.02 (2007).
- [12] U. Rau, in *Materials Research Society Proc.* **668**, H9.1.1 (2001).
- [13] M. Igalson and H. W. Schock, *J. Appl. Phys.* **80**, 5765 (1996).
- [14] J.T. Heath, J.D. Cohen, and W.N. Shafarman, *J. Appl. Phys.* **95**, 1000 (2004).
- [15] I. L. Repins, B. J. Stanbery, D. L. Young, S. S. Li, W. K. Metzger, C. L. Perkins, W. N. Shafarman, M. E. Beck, L. Chen, V. K. Kapur, D. Tarrant, M. D. Gonzalez, D. G. Jensen, T. J. Anderson, X. Wang, L. L. Kerr, B. Keyes, S. Asher, A. Delahoy, B. Von Roedern *Prog. Photovolt.: Res. and Appl.* **14**,. 25 (2005).
- [16] J. Lee, J. T. Heath, W. N. Shafarman, and J. D. Cohen, in *Materials Research Society Proc.* **865**, F12.4.1 (2005).
- [17] J. Guillemoles, U.Rau, *Adv. Mater* **11**, 957 (1999).
- [18] U. Rau, M. Schmitt, D. Hilburger, F. Engelhardt, O. Seifert, J. Parisi, W. Riedl, J. Rimmasch, and F. Karg, in *Proceedings of the 26th IEEE Photovolt. Spec. Conf.*, **371**, (1997).
- [19] S. Lany and A. Zunger, *J. Appl. Phys.* **100**, 113725 (2006).
- [20] S. Lany and A. Zunger, *Phys. Rev. Lett.* **100**, 016401 (2008).

- [21] S. S. Hegedus and W. N. Shafarman, *Prog. Photovolt: Res. Appl.* **12**, 155 (2004).
- [22] U. Rau, A. Jasenek, H. W. Schock, F. Engelhardt, T. Meyer, *Thin Solid Films* **361**, 298 (2000).
- [23] J. Mattheis, P. J. Rostan, U. Rau, J. H. Werner, *Sol. Energy Mater. Sol. Cells*, **91**, 689 (2007).
- [24] M. Burgelman, P. Nollet, and S. Degraeve, *Thin Solid Films* **361**, 527 (2000).
- [25] P. D. Paulson, R. W. Birkmire, and W. N. Shafarman, *J. Appl. Phys.* **94**, 879 (2003).
- [26] K.L. Chopra, P.D. Paulson, and V. Dutta, *Prog. Photovolt: Res. Appl.* **12**, 69 (2004).
- [27] M. Gloeckler, *Thin Solid Films* **480**, 241 (2005).
- [28] J. H. Lyou, E. A. Schiff, S. Guha, and J. Yang, *Appl. Phys. Lett.* **78**, 1924 (2001).
- [29] R.S. Crandall, *J. Appl. Phys.* **55**, 4418 (1984).
- [30] R.S. Crandall, *J. Appl. Phys.* **54**, 7176 (1983).
- [31] T. McMahon, A. Fahrenbruch, in *Proc. 28th IEEE Photovolt. Spec. Conf.*, **549**, (2000).
- [32] E. A. Schiff, *Sol. Energy Mater. Sol. Cells* **78**, 567 (2003).
- [33] N. F. Mott, *J. Phys. C*. **13**, 5433 (1980).
- [34] J. Mattheis, J. H. Werner, and U Rau, *Phys. Rev. B* **77**, 085203 (2008).
- [35] R. A. Street, *Hydrogenated Amorphous Silicon* (Cambridge University Press, 1991).